Optical pumping of a dense quantum gas at its limits

Continuous Sisyphus cooling and demagnetization cooling towards degeneracy

Von der Fakultät für Mathematik und Physik der Universität Stuttgart
zur Erlangung des akademischen Grades eines Doktors der
Naturwissenschaften (Dr. rer. nat.) genehmigte Abhandlung

vorgelegt von

Valentin V. Volchkov

aus Novosibirsk

Hauptberichter:	Prof. Dr. Tilman Pfau
Mitberichter:	Prof. Dr. Jörg Wrachtrup
Prüfungsvorsitzender:	Prof. Dr. Hans Peter Büchler
Tag der mündlichen Prüfung:	28. November 2013

5. Physikalisches Institut Universität Stuttgart

2013

Abstract

In this thesis, I study optical pumping as a powerful cooling tool for trapped ultra-cold atoms in a highly collisional regime.

First application of optical pumping is a continuous loading scheme used to transfer atoms from a guided beam into a hybrid trap. Further, I introduce a Sisyphus cooling scheme based on radio-frequency transitions and optical pumping, operating simultaneously to the accumulation of atoms in the trap. The combined scheme of continuous loading and Sisyphus cooling is demonstrated for a large range of initial conditions of the guided atoms. Thereby, I show that collisional thermalization occurs in a steady-state for almost arbitrary initial conditions, provided that the first dissipative step is able to prevent the atom from leaving the trap during its first passage. On the one hand, this scheme could be applied to a wide range of atomic or molecular beams. On the other hand, phase-space density of 4×10^{-4} is reached in a continuous operation mode with chromium atoms.

In the second part, I investigate demagnetization cooling based on dipolar relaxation collisions driving the thermalization of the internal (spin) and the external (motional) degrees of freedom. In the case of a gas, one has the advantage that the spin degree of freedom can be cooled very efficiently using optical pumping. It is shown, that demagnetization cooling of a gas is more efficient than evaporation cooling in terms of phase-space density gain versus loss of atoms. This allows reaching a temperature of $6\,\mu$K at a phase-space density of 0.03.

It is observed, that both, continuous Sisyphus cooling and demagnetization cooling are limited by a density dependent loss mechanism. I present circumstantial evidence for excited-state collisions as the dominant limiting process. Finally, I discuss possible extensions to the current experimental procedures, possibly allowing reaching quantum degeneracy by optical means only.

Contents

Zusammenfassung

Gegenstand der vorliegenden Arbeit sind Experimente mit ultra-kalten Quantengasen, dabei steht die Methode des optischen Pumpens im Vordergrund. Dieses Verfahren ist besonders effizient, um dipolare ultra-kalte Atome zu fangen und dann bei hohen Dichten zu kühlen.

Der erste Teil der Arbeit beschäftigt sich mit dem kontinuierlichen Laden einer optischen Dipolfalle aus einem Strahl von Chromatomen [Falkenau et al., 2011]. Hierbei bewegen sich schwachfeld-suchende Atome entlang einer Dipolfalle auf eine magnetische Barriere zu und werden dadurch abgebremst. Die kinetische Energie wird in potentielle Energie entsprechend der Höhe der Barriere umgewandelt und durch optisches Pumpen in unmittelbarer Nähe des Magnetfeld-Maximums dissipiert. Auf diese Art und Weise werden Atome im starkfeld-suchendem Zustand in einer Hybridfalle gesammelt. Das Fallenvolumen wird durch einen axialen magnetischen Einschluss und optischen Einschluss in radialer Richtung bestimmt. Mit diesem Verfahren können geladene Atome ins thermische Gleichgewicht gebracht werden, vorausgesetzt die kontinuierliche Quelle ist ein relativ kalter ($\approx 65\,\mu$K) und langsamer (1 m/s) Strahl mit einem hohen Fluss an Atomen ($> 10^9$ Atome/s) [Aghajani-Talesh et al., 2009, Aghajani-Talesh et al., 2010]. Das thermische Gleichgewicht wird über Stöße zwischen den gefangenen Atomen erreicht und stellt eine wichtige Voraussetzung für das Verdampfungskühlen dar [Falkenau et al., 2012]. Bei einem niedrigen Fluss oder einer zu hohen radialen Temperatur verbleibt die Dichte in der Falle (und die damit zusammenhängende Stoßrate) auf einem Wert, der für ein effizientes Verdampfungskühlen nicht ausreicht. Bei höheren Geschwindigkeiten reicht die magnetische Barriere nicht aus, um die Atome vollständig abzubremsen, so dass ein Teil der kinetischen Energie innerhalb der Falle umverteilt wird und zum ineffizienten Laden führt.

Um die übrig bleibende kinetische Energie weiter zu reduzieren, präsentieren wir in dieser Arbeit ein zusätzliches Kühlverfahren, bekannt als Sisyphuskühlung. Dieser Kühlmechanismus wurde ursprünglich von Pritchard vorgeschlagen [Pritchard, 1983] und basiert ebenfalls auf optischem Pumpen. In unserem Fall wird ein Hochfrequenzfeld eingestrahlt, welches ortsabhängig Atome in weniger stark gefangene magnetische Unterzustände transferiert. Gefangene Atome sehen ein steiles Potential während sie sich axial vom Boden der Falle wegbewegen, in der Nähe des Umkehrpunktes erfolgt die

Wechselwirkung mit dem Hochfrequenzfeld, so dass auf dem Rückweg zum Fallenboden die kinetische Energie nicht vollständig zurückgewonnen wird. Der Sisyphus-Zyklus wird in der Nähe des Fallenbodens abgeschlossen, wenn die Atome den optischen Pumpstrahl passieren und wieder in den ursprünglichen stark gefangenen Zustand gepumpt werden. Die Energie wird durch die spontane Emission eines Photons irreversibel abgeführt. Dieser Prozess kann zeitgleich zum kontinuierlichen Laden der Falle ablaufen und hat im Gleichgewichtszustand eine niedrigere Temperatur und eine höhere Phasenraumdichte zur Folge.

Im Rahmen dieser Arbeit wird eine Computersimulation des Ladens und der gleichzeitigen Sisyphuskühlung entwickelt. Diese Simulation beruht auf Methoden aus der Moleküldynamik, ein Verfahren bei dem Bewegung und Wechselwirkung von einzelnen Teilchen in kleinen Zeitschritten simuliert wird [Allen, 2004]. Ergebnisse der Simulation werden in Verbindung mit experimentellen Daten benutzt, um kontinuierliche Sisyphus-Zyklen nachzuweisen. Weiterhin untersuchen wir den Gleichgewichtszustand des Ladeprozesses bei verschiedenen Anfangsbedingungen des Atomstrahls. Wir zeigen, dass mit Hilfe der Sisyphuskühlung geladene Atome ins thermische Gleichgewicht kommen, selbst wenn der Fluss und die Phasenraumdichte des Atomstrahl um mehrere Größenordnungen reduziert werden [Volchkov et al., 2013]. Außerdem ist es nun möglich Atome trotz niedriger magnetischer Barriere oder geringer Tiefe der Dipolfalle effizient zu Laden. Die hier vorgestellte Technik eignet sich daher besonders, um Teilchen (Atome oder Moleküle) aus einem Strahl in eine Falle zu laden. Diese Technik setzt nur voraus, dass zustandsabhängige Potentiale mit externen Feldern erzeugt werden können und schnelles optisches Pumpen das Ändern des internen Zustands erlaubt. Aus diesem Grund ist die hier beschriebene Methode vor allem für Atome und Moleküle interessant, die nur in Form von langsamen, aber schwachen oder radial heißen Strahlen vorliegen [Rangwala et al., 2003, van Buuren et al., 2009, Tsuji et al., 2010]. Insbesondere bei Molekülen würde eine Methode zur Erzeugung von ultra-kalten Proben bis hin zu einem Bose-Einstein Kondensat den Weg für eine Reihe von spannenden Anwendungen ebnen. Dazu zählen der Quanten-Computer auf der Grundlage von polaren Molekülen in einem optischen Gitter [DeMille, 2002] oder Präzisionsmessungen zur Bestimmung der Änderung von Naturkonstanten [Chin et al., 2009]. Gleichzeitig stellt die kontinuierliche Sisyphuskühlung mit einer maximalen Phasenraumdichte von 4×10^{-4} einen weiteren Schritt in Richtung eines kontinuierlichen Atomlasers dar.

Im zweiten Teil dieser Arbeit wenden wir Entmagnetisierungskühlung auf ein dichtes Chrom-Gas an. Die Entmagnetisierungskühlung beruht auf der Spin-Bahn-Kopplung, die Spin- und Bewegungs-Freiheitsgrade in thermisches Gleichgewicht bringt [Enss and Hunklinger, 2005]. Im Falle eines Gases, besteht zusätzlich der Vorteil darin, dass der Spinfreiheitsgrad sehr effizient durch optisches Pumpen gekühlt werden kann. Das relativ hohe magnetische Moment von Chromatomen von $6\mu_\mathrm{B}$ (im Vergleich dazu haben beispielsweise Atome der Alkalimetalle nur $1\mu_\mathrm{B}$) erlaubt durch dipolare Relaxationsstöße eine schnelle Thermalisierung zwischen dem Spin- und dem Bewegungs-Freiheitsgrad. Als dipolare Relaxation bezeichnet man inelastische Stöße, bei denen der magnetische Unterzustand eines oder beider Stoßpartner verändert wird, während Bewegungsenergie in Zeemanenergie (oder umgekehrt) umgewandelt wird. Je nach Ausgangszustand der Stoßpartner kann dipolare Relaxation zum Heizen [Hensler et al., 2003] oder Kühlen [Hensler et al., 2005] führen. Sind die Stoßpartner im niedrigsten magnetischen Unterzustand, so müssen sie genügend relative Bewegungsenergie besitzen, um den energetisch höheren Unterzustand zu erreichen. Daher hängt die Rate der dipolare Relaxationsstöße von dem angelegten Magnetfeld ab.

Wir untersuchen experimentell die Thermalisierung der Spin- und Bewegungs-Freiheitsgrade von Chromatomen als Funktion des externen Magnetfeldes in einer tiefen Dipolfalle. Hierbei finden wir gute Übereinstimmungen mit theoretischen Vorhersagen. Die Entmagnetisierungskühlung eines Gases wurde in [Fattori et al., 2006] im Rahmen eines Machbarkeitsbeweises gezeigt. Dabei wurde die Temperatur des Gases von $19\,\mu$K auf etwa $11\,\mu$K innerhalb von 7 Sekunden reduziert. In der vorliegenden Arbeit hingegen wenden wir Entmagnetisierungskühlung auf Chromatome direkt nach dem Laden in die Dipolfalle an und erhöhen die Phasenraumdichte dabei um mehr als zwei Größenordnungen auf den Wert von 0,03. Die Temperatur sinkt dabei von $90\,\mu$K auf $6\,\mu$K. Es wird somit gezeigt, dass die Entmagnetisierungskühlung effizienter ist als das Verdampfungskühlen im Hinblick auf den Phaseraumdichte-Gewinn pro verlorenem Atom.

Es zeigt sich, dass sowohl kontinuierliche Sisyphuskühlung als auch Entmagnetisierungskühlung durch einen dichtebegrenzenden Mechanismus limitiert sind. Im Falle der Entmagnetisierungskühlung können wir Raten-Gleichungen zur Beschreibung der Verluste aufstellen. Diese Raten-Gleichungen basieren auf der Annahme, dass Licht-induzierte Stöße und daraus folgende Zweikörper-Verluste den dichtebegrenzenden Mechanismus ausmachen. Aufgrund der dichteabhängigen Relaxationsrate und den dichteabhängigen Licht-induzierten Stößen ergibt sich eine (ungewöhnlich starke) quadratische Skalierung des Verlustkoeffizienten mit der atomaren Dichte, genau so wie sie im Experiment beobachtet wird. Wir untersuchen weiterhin die Verlustraten als Funktion der Intensität des optischen Pumplichts und finden im Bereich von niedrigen Intensitäten einen Anstieg der Kühlrate sowie der Verlustrate, was ebenfalls die These der Licht-induzierte Stöße stützt. Beim Variieren der Verstimmung des optischen Pumplichts setzen Verluste erst ab einer bestimmten (positiven) Verstimmung ein. Wir erklären dieses Verhalten durch ein repulsives Molekülpotential zwischen einem Atom im Grundzustand und einem angeregten Atom. Je größer die Verstimmung des Pumplichts ist, desto kleiner ist der Abstand zwischen beiden Atomen, bei dem die Anregung stattfindet, und desto stärker werden die Atome von einander weg-beschleunigt [Gallagher and Pritchard, 1989]. Die Emission des Photons findet bei einem größeren interatomaren Abstand statt und das emittierte Photon ist energieärmer als das absorbierte. Erst ab einer bestimmten Verstimmung reicht die so in kinetische Energie umgewandelte Energiedifferenz aus, um die Dipolfalle zu verlassen. Wir überprüfen diesen Zusammenhang für verschiedene Tiefen der optischen Dipolfalle und bestätigen diesen Sachverhalt experimentell. Die oben genannten experimentellen Ergebnisse deuten alle auf Licht-induzierten Stöße hin.

Nichtsdestotrotz kann die Energie, die beim Streuen eines einzelnen Photons dissipiert wird, beim optischen Pumpen deutlich größer sein, als die bei bei einem Rückstoß übertragene Energie (wie es bei den meisten Laserkühlverfahren der Fall ist).

Dies erlaubt es mit nur wenigen Photonen einen starken Kühleffekt zu erzielen.

Zum Schluss diskutieren wir weitere Möglichkeiten die Phasenraumdichte im kontinuierlichen Betrieb des Lademechanismus weiter zu erhöhen, wie z.B. durch einen Dimple [Stamper-Kurn et al., 1998b]. Außerdem schlagen wir vor Licht-induzierte Stöße durch geeignete Wahl der Verstimmung des optischen Pumplichts zu unterdrücken [Burnett et al., 1996].

1 Introduction

Within the past two decades, the study of ultra-cold gases has become one of the most active fields in atomic physics. The attractiveness of this field stems to a great extent from its *interdisciplinarity*.

The realizations of Bose-Einstein condensation in dilute and weakly interacting gases [Anderson et al., 1995, Davis et al., 1995, Bradley et al., 1995] initiated the success story of ultra-cold atomic gases. It became clear that ultra-cold gases were not only a perfect candidate for the study the Bose-Einstein condensation itself (a phenomenon that still inspires the present-day research [Gaunt et al., 2013]), but also a multitude of long-standing many-body problems.

Ultra-cold (bosonic and fermionic) gases constitute versatile systems due to the unprecedented control of the most relevant experimental parameters such as dimensionality, geometry, or interaction strength. Far from giving a complete list, we mention here several remarkable examples.

Over decades the quantum phase transitions in liquid helium have been intensively studied and presented a challenging many-body problem for the theoretical description due to strong correlations. Using ultra-cold gases, the phenomena of superfluidity have been reproduced and studied in a pure form without the complications of strong interactions of liquid helium [Onofrio et al., 2000, Madison et al., 2000, Sidorenkov et al., 2013]. Few fermion systems have been prepared in order to study questions from nuclear physics [Serwane et al., 2011]. Fundamental questions regarding the transition from quantum to classical physics, referred to as decoherence have been subject of experimental investigation using ultra-cold atoms [Ratschbacher et al., 2013]. The study of quantum gases in periodic [Greiner et al., 2002] (or disordered [Billy et al., 2008]) optical potentials has become a particularly fruitful branch of the field, establishing a direct link to condensed matter physics. The universal thermodynamic properties of strongly interacting Fermi gases have been investigated [Bloch et al., 2008, Ku et al., 2012]. Non-equilibrium dynamics of strongly interacting systems give rise to analogues of hydrodynamics and cosmology [Hung et al., 2013].

The matter-wave analogue of a cw laser

The ability to extract atoms from a Bose-Einstein condensate (BEC) in the form of a single wave-function, a so-called **atom laser** [Mewes et al., 1997, Anderson and Kasevich, 1998, Hagley et al., 1999], inspired significant experimental efforts to produce a continuous BEC in analogy to the continuous wave (cw) optical laser. The realization of such a cw-atom laser would undoubtedly become a breakthrough for precision measurements and tests of fundamental quantum mechanics. However, so far, all experimental realizations of atom lasers were operated in a pulsed mode. The atoms were extracted until the BEC was depleted and a new had to be prepared. Even though it has been demonstrated that a BEC could be kept alive for arbitrary long times by merging it with a new BEC [Chikkatur et al., 2002], each time two condensates were merged their phase was randomized in the process. In another work [Robins et al., 2008], one BEC served as the source for a continuously out-coupled atom laser, while a second BEC was used to continuously replenish the source. The replenishment was realized using optical pumping and bosonic stimulation, therefore the phase of the source remained unaffected. Nevertheless, the operation of such a pumped atom laser was not truly continuous, since the pumping BEC was depleted after a short time.

All optical Bose-Einstein condensation

Reaching Bose-Einstein condensation by optical means only [Santos et al., 2001, Cirac and Lewenstein, 1996] is another long-standing goal in the field of ultra-cold atoms. Renewed interest in optical cooling methods of the quantum gases community originates from the possibility of using narrow line-width transitions for standard laser cooling techniques [Katori et al., 1999, McClelland and Hanssen, 2006] and recent progress in laser cooling of molecules [Shuman et al., 2010, Zeppenfeld et al., 2012]. The motivations are manifold. On the one hand, optical cooling may pave the way to degeneracy of ground-state molecules – a goal pursued by many groups. Precision measurements on molecules could advance the search for the electric dipole moment of the electron [Vutha et al., 2011], or probe the variation of fundamental constants [Chin et al., 2009]. Ultra-cold molecules with a strong dipole-dipole interaction could be used for quantum computing [DeMille, 2002]. On the other hand, new *lossless* laser cooling methods may be considered as an alternative to evaporative cooling allowing to boost the number of atoms of a degenerate gas.

This thesis

The experimental approach presented in this work is somewhat special compared to the standard ultra-cold atoms experiment. While in a standard experiment all manipulating (trapping and cooling) tasks are performed in a sequential mode, the apparatus used in this work is specifically designed and built such that almost all tasks run simultaneously! This is made possible by *spatially* (instead of temporally) separating the tasks, therefore it has certain similarity to a conveyor belt. Specifically, the heart of the experimental apparatus is an elongated configuration of four current-carrying bars, acting as a guide to laser-cooled chromium atoms. Thereby, we produce a slow and *continuous* beam of guided chromium atoms, that passes from one 'station' to the next, increasing its phase-space density at each station.

In the spirit of the above mentioned interdisciplinarity, the guided chromium beam apparatus allows us to work in different directions, addressing questions from different fields, as will be explained in the following.

The continuous operation mode constitutes a completely different approach to the efforts of reaching Bose-Einstein condensation in a cw-regime. Since the operation of the guided beam is intrinsically 'cw', we do not have to worry about how to replenish a pulsed BEC. Instead, the main question is: what is the next station to further increase the *steady-state* phase-space density at the end of the conveyor belt? And then: how many different stations do we need to obtain a truly continuous atom laser? Within this work we explore optical pumping as a powerful tool to increase the steady-state phase-space density by several orders of magnitudes. Consequently, it constitutes an important stage towards the cw-atom laser.

In the cold molecules community the operation of continuous beams is very common [Egorov et al., 2002]. Since the methods developed within this work are general, our experimental approach can be considered a model system for a variety of particle beams. Therefore, the presented techniques based on optical pumping could be applied to a large range of species, in particular molecules, presenting a possible route towards Bose-Einstein condensation.

Finally, apart from continuous operation, the investigation of optical pumping in dense samples allows us to push forward the frontier towards quantum degeneracy by all optical means. The main advantage over standard laser cooling is that the energy dissipated by a single photon in the case of optical pumping is not limited to recoil energy, but can be orders of magnitude larger. Typically, energy comparable to the thermal energy of the sample is extracted from the atoms, thereby drastically reducing the number of necessary photons and allowing working at extreme densities.

The present thesis is organized as follows. In chapter 2 we introduce recurring concepts of state-dependent potentials, optical pumping, and dark-states. The continuous loading mechanism exploited in this work is then presented as a combination of those concepts. Chapter 3 is dedicated to a comprehensive study of Sisyphus cooling in a continuously loaded trap. We identify the shortcomings of the conventional continuous loading scheme and demonstrate that simultaneous Sisyphus cooling makes the continuous loading mechanism even more robust and thus applicable to a wide range of particle beams. Additionally, we reach a steady-state phase-space density of 4×10^{-4}, which is a significant improvement.

In chapter 4, we switch from continuous to pulsed operation and investigate the possibility to optically pump atoms directly into a condensate. To this end we make use of demagnetization cooling. We discuss in detail the prerequisites for demagnetization cooling, in particular, strong dipole-dipole interactions and the existence of a dark state for the optical pumping. We find that temperature as low as a few recoil temperatures can be obtained using demagnetization cooling. We present evidence for light-assisted losses as the main limiting mechanism. Despite this obstacle, we reach a phase-space density of 0.03. Finally, in the last chapter we discuss various strategies that should allow overcoming the present limitations.

2 Continuous loading of a trap from an atomic beam

Continuous beams of particles not only constitute the basis of a wide range of fundamental research, but also play a major role in high-tech applications, most prominent of them being the traditional caesium beam frequency standard [Ramsey, 1983].

The flux and the phase-space density are the most important figures of merit of a particle beam. Since any measurement performed on a beam has a signal-to-noise ratio that directly depends on the flux and the PSD, techniques allowing to increase the PSD and the number of atoms in the region of interaction are highly desirable and can trigger significant progress. In this spirit, the development of laser cooling and the magneto-optical trap in which atoms from a fast and hot beam are stopped and cooled, increasing the PSD by many orders of magnitude, allowed for the implementation of an atomic fountain clock [Kasevich et al., 1989]. However, this approach can only be applied to a fraction of possible beams i.e. composed of atomic [Metcalf and van der Straten, 2002] or molecular species [Shuman et al., 2010, Barry et al., 2012] with suitable cycling transitions. Therefore, alternative approaches like buffer-gas cooling [Doyle et al., 1995, Egorov et al., 2002, Patterson et al., 2009], velocity filtering [Rangwala et al., 2003, van Buuren et al., 2009, Tsuji et al., 2010], Zeeman-deceleration [Vanhaecke et al., 2007, Narevicius et al., 2008] or Stark-deceleration [Bethlem et al., 1999, Enomoto and Momose, 2005, Tarbutt et al., 2004] have been developed to slow or stop a molecular beams. Yet, most of these methods do not change the PSD. In this context, the realization of an atomic diode [Price et al., 2008] that does not rely on laser cooling equally allows stopping and accumulating atoms from a slow, guided beam.

The implementation of the atomic diode in a continuously loaded atomic trap is the key concept to all experiments described in this work. However, the idea and the experimental realization of the conventional continuous loading are already well described in a series of publications [Aghajani-Talesh et al., 2009, Falkenau et al., 2011, Falkenau et al., 2012] and, in particular, in the works of Jahn Rührig [Rührig, 2011] and Markus Falkenau [Falkenau, 2011]. Therefore, the purpose of this chapter is to build a link between previous work and new results presented in this work.

First, we introduce techniques for preparing and manipulating of cold atoms, with emphasis on conservative and dissipative traps. We discuss optical pumping as means to manipulate the internal state of the atoms. Second, we briefly describe the experimental environment, central element of which is a rather unusual guided atomic beam. We then revise the specific implementation of the continuous loading of a conservative atomic trap from a guided beam and the dynamics of the loading process. Finally, we study and discuss the impact of additional experimental parameters that were not taken into account before.

2.1 Experimental techniques and continuous loading

This section summarizes several useful aspects from the vast field of atom-light interaction. We skip any historic remarks and exact derivations, since they can be found in many text-books on this subject. In particular, we refer to *Laser cooling and trapping* [Metcalf and van der Straten, 2002] and *Bose-Einstein Condensation in Dilute Gases* [Smith and Pethick, 2002] (and the references therein) which contain thorough descriptions of most experimental techniques.

2.1.1 Conservative traps for cold atoms

The most commonly used conservative traps for neutral atoms are potentials produced by static magnetic fields and light fields.

The coupling of the magnetic moment $\vec{\mu}$ of an atom to an external magnetic field $\vec{B}$ produces an energy shift (Zeeman-shift) given by

$$E_{\mathrm{Z}} = \vec{\mu} \cdot \vec{B} \tag{2.1}$$

Therefore, an inhomogeneous magnetic field configuration can be used to spatially confine atoms [Migdall et al., 1985]. A magnetic trap may be created by a single current carrying wire [Schmiedmayer, 1995] or a complex magnetic coil geometry [Bergeman et al., 1987]. The advantages of the magnetic traps are their depth (using superconducting coils trap depth of several K may be achieved [Harris et al., 2004]) and large trapping volume.

Conservative optical traps are based on the dynamic polarizability of neutral atoms and the associated optical dipole forces in a light field. The interaction energy is given by

$$E_{\mathrm{dip}} = -\frac{1}{2\epsilon_0 c}\Re(\alpha) I \tag{2.2}$$

where I is the intensity of the light field and α is the complex polarizability of the atom [Grimm et al., 2000]. In an intuitive picture, the electric field $\vec{E}$ induces an atomic dipole moment $p = \alpha E$ which then interacts with the field similar to the Zeeman-effect. The interaction energy can be positive or negative depending on whether the induced dipole moment is parallel or anti-parallel with respect to the electric field. Here again, an inhomogeneous intensity distribution (such as a focused laser beam, a standing wave, or a hollow beam) can be used to trap atoms. The conservative dipole force is accompanied by a dissipative force which comes from the imaginary part of the polarizability and will be dealt with in section 2.1.2. However, the dissipative force can be neglected in practice, when the difference between the driving frequency ω_{L} of the light field and the atomic transition frequency ω_0 is much larger than the transition width Γ. The optical dipole traps (ODT) can provide strong confinement on a micrometer scale but their depth is often limited by the available laser power to some mK. In addition, species without a magnetic moment (e.g. earth-alkaline atoms) can be trapped in an ODT.

State-dependent potentials

Let us now consider the internal structure of atoms in the context of magnetic and optical potentials.

The magnetic interaction energy depends on the orientation of the magnetic dipole moment with respect to the magnetic field. We can rewrite equation 2.1 as $U_{\mathrm{Z}}(\vec{r}) = g m_{\mathrm{S}} \mu_{\mathrm{B}} \left|B(\vec{r})\right|$, where m_{S} denotes the magnetic sub-state and g is the Landé-factor. We immediately see that depending on sign of $g m_{\mathrm{S}}$ the atoms can be either attracted or repelled by regions of high magnetic field. The control over the internal state thus gives the possibility to change the potential. This can be exploited for example as an implementation of the technique called evaporative cooling [Hess, 1986], in which the internal state m_{S} of a trapped atom is changed such that the atom becomes untrapped or even 'anti-trapped'. Selectively changing the state of high-energetic atoms and thereby removing them from the trap can lead to an efficient cooling of the remaining atoms. The continuous loading technique described in section 2.1.4 can be seen as the inverse process.

The internal structure of atoms can also lead to state-dependent optical potentials. When the detuning $\delta = \omega_{\mathrm{L}} - \omega_0$ is much larger than the fine-structure splitting of the atom, the optical dipole potential becomes independent of the internal states. This is an advantage when mixtures of magnetic sub-states (spin mixture) is being investigated [Stamper-Kurn et al., 1998a]. For a detuning on the order or smaller than the fine-structure splitting, polarisation of the light and the associated selection rules need to be taken into account. In particular, the transitions strengths between the specific sub-states in the ground state and the corresponding excited states define the magnitude of the optical potential. In addition, potentials arising from coupling to different excited states must be summed, and it is hence possible to completely cancel the potential for a given state by appropriately choosing the detuning and the light polarisation

[LeBlanc and Thywissen, 2007].

In any case, in order to efficiently trap atoms in a conservative potential a dissipative mechanism is needed to remove sufficient energy.

2.1.2 Dissipative traps

As already mentioned above, the imaginary part of the atomic polarizability is responsible for a dissipative force. This so-called radiation force results from redistribution of radiation by absorption and spontaneous emission of photons. One can combine several near-resonant beams in order to trap atoms in momentum space using radiation pressure [Chu et al., 1985] – a technique known as Doppler cooling. The redistribution of photons implies that the energy dissipated per scattered photon is on the order of the recoil energy. Therefore, a very large number of photons must be scattered to cool atoms from room temperature into the millikelvin regime. A particularly prominent example of dissipative traps is the magneto-optical trap (MOT) which combines Doppler cooling with spatial trapping by introducing a spatially varying radiation force with the help of a magnetic field gradient [Raab et al., 1987]. It is worth mentioning that the experimental realization of the MOT triggered a huge development in the field of atomic physics, opening the door to studies of ultra cold collisions, new precision measurements, and not at least the investigation of degenerate quantum gases.

The major limitation of the MOT is the continuous scattering of light and the associated heating and losses, one therefore needs a means to decouple atoms from the light when the cooling reaches the final temperature.

Dark-states

One generally refers to dark-states when an atom leaves the laser cooling by some irreversible (spontaneous) transition. The dark-state can be a different hyperfine state as it is the case for the dark-spot MOT [Ketterle et al., 1993] or a metastable electronic state in the case of chromium [Schmidt et al., 2003]. Another way to create a dark-state is tailoring the polarisation of the light field, such that a specific sub-state (or a superposition of multiple states) does not couple to the light. The stretched state in a $J \rightarrow J$ transition is then a trivial dark-state to circularly polarized light, and it will be used for optical pumping in the present work. A more sophisticated dark-state within the 'velocity selective coherent population trapping' consists of a superposition of two momentum states [Aspect et al., 1988]. Only the zero momentum-state remains dark over arbitrary long times, accumulation of atoms in this state then allows reaching temperatures far below the recoil limit [Lawall et al., 1995].

In all cases, it is the spontaneous decay of the excited that state populates the dark-state.

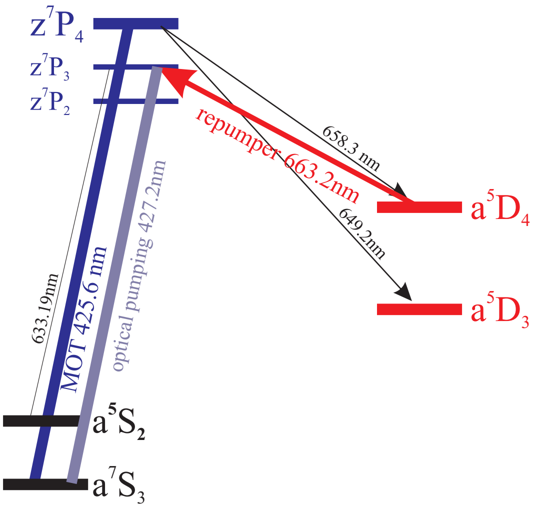

Figure 2.1: Electronic level structure of the used transitions is shown. Decay to metastable states is indicated by black arrows.

2.1.3 Production of the magnetically guided beam of chromium atoms

The source for the continuous loading of a conservative potential is a beam of magnetically guided chromium atoms. The experiment was set up by Alexander Greiner, technical details concerning the magnetic guide itself as well as lasers used for laser cooling and re-pumping can be found in his PhD-thesis [Greiner, 2008]. In this section we give a brief overview of the experimental set-up and emphasise some parameters that are particularly relevant for this thesis.

Chromium properties

In this work we use a bosonic isotope of chromium, specifically ^{52}Cr. The electronic configuration of chromium is [Ar]3d^{5}4s^1. The laser cooling transition of chromium $^7S_3 \rightarrow ^7P_4$ involves the outer electron from the s-shell and has a line-width of $\Gamma = 2\pi \times 5\,\mathrm{MHz}$, which is similar to the D1 and D2 lines of alkali-metals. The presence of the half-filled d-shell leads to intercombination transitions to metastable states $^5D_4$ and $^5D_3$, as shown in figure 2.1. The total number of 6 unpaired electrons in the ground state gives rise to a large magnetic moment of $6\mu_\mathrm{B}$. The ^{52}Cr isotope has no nuclear spin and therefore no hyperfine-structure.

Moving molasses MOT in a magnetic guide

Four current carrying copper wires inside of the experimental chamber (see figure 2.2) create a large two dimensional quadrupole field. The magnetic guide is therefore an extremely elongated magnetic trap. A moving molasses MOT (MMMOT) is operated in the vicinity of the magnetic guide and cools atoms into a frame of reference moving

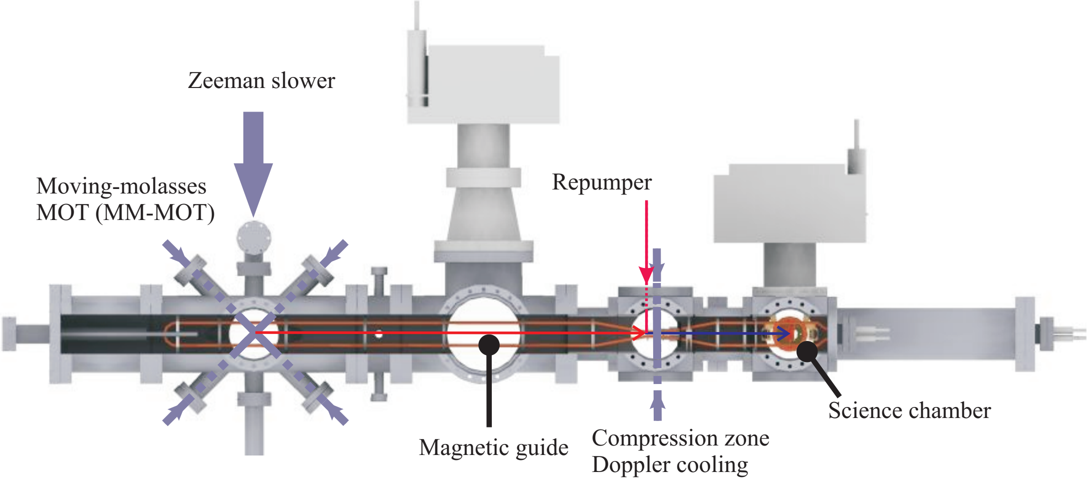

Figure 2.2: The insides of the vacuum chamber are shown. The transversely hot atomic beam of metastable chromium atoms is depicted as the horizontal red arrow between the guide bars. The atoms are transversely compressed in the tapered region (compression zone) and are transferred back to the ground state by the 're-pumper' laser. Further laser cooling is applied in the tapered region. The atoms are decompressed before reaching the science chamber.

along the guide [Greiner et al., 2007, Griesmaier et al., 2009][1]. This is accomplished by giving the cooling laser beams in the plane of the propagation different detunings. Since there is no restoring force along the magnetic guide the cold atoms leave the MMMOT in a low-field seeking state with $m_S > 0$ at a velocity defined by the difference in detuning. Figure 2.2 shows the magnetic guide bars inside of the vacuum chamber, the red arrow along the guide denotes the guided atoms which are dominantly in the metastable $^5D_4$ state. The atoms are pumped back to the ground state in the tapered region of the guide by a laser at 663.2 nm.

Transverse temperature control

The transverse spatial distribution of the guided atoms after the MMMOT resembles a thermal distribution with a temperature $T \approx 250\,\mu$K. We can further cool the atomic beam with a transverse cooling configuration in the compressed region of the magnetic guide. In this process all atoms are pumped into the $m_S = 3$ state. Finally, we obtain $T \geq 65\,\mu$K in the science chamber [Aghajani-Talesh et al., 2010], as illustrated in figure 2.2.

The relevant properties of the beam reaching the science chamber are summarized in table 2.1.

---

[1] Similar set-ups with magnetically guided atoms have also been described in [Olson et al., 2006, Cren et al., 2002].

2.1.4 One-way gate into a conservative trap

In the science chamber the atomic beam is overlapped with a focused laser beam, creating a deep optical dipole trap for chromium atoms. As discussed in the section 2.1.1, such a conservative trap requires a dissipative mechanism in order to retain passing atoms. Specifically, the directed kinetic energy of the atoms needs to be removed. The dissipation of the directed kinetic energy takes place in form of a single slowing step: the atoms climb up a potential hill, convert most of the kinetic energy into potential energy, which is then removed by changing the internal state of the atoms. For this purpose, a magnetic barrier potential is created by a pair of small coils at the centre of the ODT. The incoming low-field seeking atoms are decelerated by the increasing magnetic field until the top of the barrier is reached. In this process a significant fraction of the original directed kinetic energy is converted into magnetic potential energy. The potential energy is dissipated using optical pumping from $m_\mathrm{S} = 3$ to $m_\mathrm{S} = -3$. This scheme is illustrated in figure 2.3. One can see that the magnetic barrier becomes a trap for the atoms in the high-field seeking $m_\mathrm{S} = -3$ state. Note that this is only true in the axial and one radial direction (axial (z) and radial (x, y) directions always refer to the cylinder symmetry of the guide and the optical dipole trap), whereas along the axis of the magnetic field the magnetic field does not have a maximum[2]. The resulting trapping potential is therefore characterised by a magnetic confinement in axial direction and optical confinement in the radial direction.

An important feature of the dissipative mechanism is that the final magnetic sub-state $m_\mathrm{S} = -3$ does not couple to the circularly polarized optical pumping light. Therefore atoms continuously accumulate in this dark-state and are not disturbed by the light field. From this point of view this loading scheme can be seen as a one-way gate into a hybrid potential.

velocity	0.4 – 1	m/s
transverse temperature	65 – 250	μK
longitudinal temperature	100 – 180	μK
flux	10^5 – 10^8	Atoms/s
phase-space density	10^{-13} – 10^{-8}	

Table 2.1: Range of accessible parameters of the guided atomic beam. Note: the properties shown here are not independent, i.e. reducing the velocity by a factor of two also reduces the flux by two orders of magnitude.

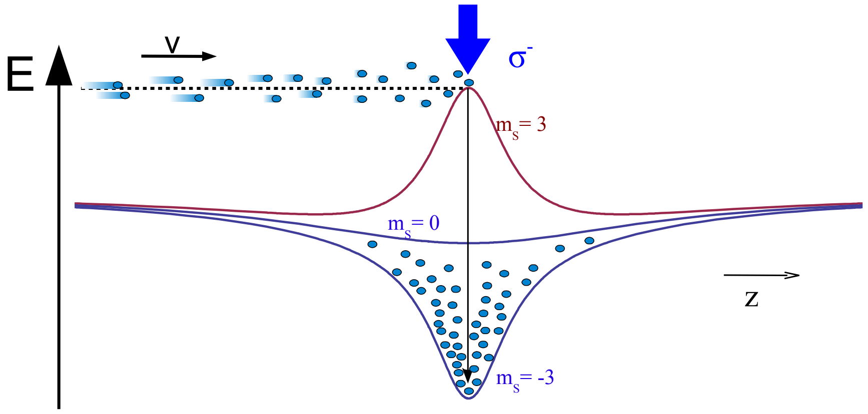

Figure 2.3: Continuous loading of a conservative hybrid potential. The guided atoms in the low-field seeking sub-state $m_S = 3$ are slowed down by the repulsive potential, created by a magnetic field barrier in the vicinity of an optical dipole trap. Close to their classical turning point the atoms are pumped into the high-field seeking dark state $m_S = -3$ by optical pumping, denoted by σ^-. The continuous loading mechanism dissipates a significant part of the longitudinally directed kinetic energy of the atomic beam.

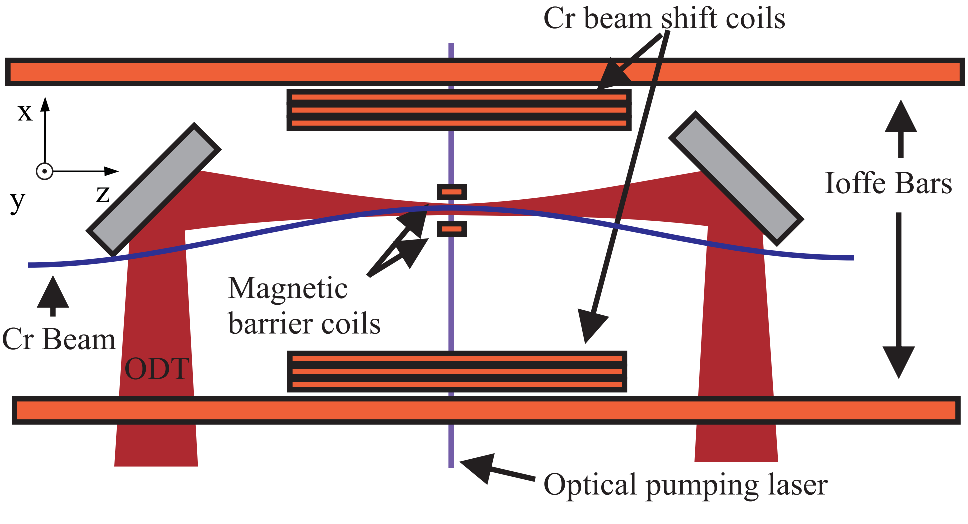

Figure 2.4: Illustration of the experimental implementation of the continuous loading mechanism. Ioffe bars create the guiding magnetic field zero, which is shifted by an additional magnetic field in x-direction. Thus, the atomic chromium beam can be overlapped with the ODT in the centre of the illustration. Magnetic barrier coils create a repulsive potential approximately in the focus of the ODT. Optical pumping beam perpendicularly intersects the ODT at the top of the repulsive potential.

Experimental parameters

The specific experimental realization of the loading scheme is presented in figure 2.4. The ODT was created by a focused laser beam from a fibre laser with a centre wavelength $\lambda = 1070\,\mathrm{nm}$, typically operated at a power $P_{\mathrm{ODT}} = 90\,\mathrm{W}$. The $1/e^2$ waist of the focus was $w_{\mathrm{ODT}} = 30\,\mu\mathrm{m}$, resulting in a trap depth $U_{\mathrm{ODT}} = k_{\mathrm{B}} \times 1.3\,\mathrm{mK}$. The Ioffe bars carried a current of 180 A and created a magnetic field gradient of 14 G/cm. In order to overlap the guided atomic beam with the ODT, we applied an additional magnetic field in x-direction shifting the zero-field of the magnetic guide by 3.5 mm, as shown in figure 2.4. The magnetic field barrier was produced by a pair of coils, each with a radius of 0.5 mm and consisting of a single winding. The barrier coils were separated by a distance of approximately 1 mm and created a magnetic field maximum along the z-direction. The magnetic field was calibrated using RF-spectroscopy, yielding $B(I) = I \times 10.82\,\mathrm{G/A}$. Unless otherwise stated, the coils were driven by a current $I = 1.15\,\mathrm{A}$, resulting in a combined magnetic field magnitude of $B = 12.1\,\mathrm{G}$. The light for optical pumping of the atoms was aligned through the barrier coils in x-direction as illustrated in the picture 2.4. The waist of the optical pumping light was $w_{\mathrm{OP}} = 140\,\mu\mathrm{m}$, the power was regulated using a PI-loop in the range of $P_{\mathrm{OP}} = 1\,\mathrm{nW} - 100\,\mu\mathrm{W}$.

Loading dynamics

The dynamics of the loading process were experimentally studied in [Falkenau et al., 2011]. We modelled the dynamics of the continuous loading into the hybrid potential using coupled rate equations for the number of atoms and their thermal energy [Falkenau et al., 2012]. The resulting model includes the continuous loading of atoms into the trap at a rate L as well as losses induced by elastic collisions with a temperature dependent collision coefficient γ_{evap}, and reads

$$\dot{N} = L - \gamma_{\mathrm{Bg}} N - \gamma_{\mathrm{evap}}(T_r, T_z) N^2 \tag{2.3}$$

$$\dot{E}_r = \bar{\epsilon}_{L,r} L - \gamma_{\mathrm{Bg}} \bar{\epsilon}_r N - \gamma_{\mathrm{evap}}(T_r, T_z) \cdot \Delta\bar{\epsilon}_r(T_r, T_z) N^2 \tag{2.4}$$

$$\dot{E}_z = \bar{\epsilon}_{L,z} L - \gamma_{\mathrm{Bg}} \bar{\epsilon}_z N - \gamma_{\mathrm{evap}}(T_r, T_z) \cdot \Delta\bar{\epsilon}_z(T_r, T_z) N^2 \tag{2.5}$$

where γ_{Bg} describes loss of atoms due to background pressure. E_r and E_z keep track of the radial and axial energies of the system. $\bar{\epsilon}_{L,r/z}$ represent the energy that is added to the system when an atom is loaded, whereas $\bar{\epsilon}_{r/z}$ is the average thermal energy per atoms which is removed in the event of a collision with particles from background gas. The right most term in the equations 2.4 and 2.5 describes the thermalization and evaporation in the system.

The numerical integration of the rate equations [Falkenau et al., 2012] showed that for realistic parameters the number of atoms saturates due to continuous evaporation,

---

[2] Maxwell's equations exclude a magnetic field maximum in all three dimensions in free space.

which is in qualitative agreement with the experimental data.

2.1.5 Experimental techniques

In order to characterise the trapped atoms we employed absorption imaging of the atomic cloud. For each measurement we released the atoms from the trap and took an absorption image after a given time of flight (TOF).

Imaging set-up

The experimental data presented in this work are obtained from imaging of the atoms. The atoms are probed by a weak (far below saturation intensity) resonant beam, therefore Lambert-Beers law can be used to reconstruct the atomic spatial distribution integrated along the propagation direction of the probe light. A detailed description of this and other useful imaging methods is given in [Ketterle et al., 1999].

In this section we put an emphasis on the optics of our imaging set-up. High-resolution imaging in the context of quantum gas experiments has gained considerable interest over the last few years. In-situ imaging of trapped atoms can give access to information that is lost during a time of flight expansion. For this reason, a high numerical aperture aspheric lens has been integrated inside of the vacuum chamber. The lens is placed 18 mm above the atoms, whereas its working distance is 11.5 mm. This introduces severe aberrations and creates an image inside of the vacuum chamber.

An additional objective was therefore designed correcting for the aberrations, specifically at the wavelength of the imaging ($\lambda = 425\,\mathrm{nm}$) using ZEMAX. Three lenses are needed to correct for the aberrations, adjust the magnification and the position of the objective at the desired location. The final design is given in table 2.2 and is depicted in figure 2.5. First, we analysed the aberration introduced by the aspheric lens: positive spherical aberration can be balanced by a bi-concave lens (introducing negative spherical aberrations). The astigmatism and coma can be reduced by an achromatic lens. In the beginning of the design the curvatures of the lenses and distances were varied to obtain the best imaging performance [Alt, 2002]. Then, one by one, the parameters

Lens	A18-15 HPX-S	LAO-150.0-50.0	LA1050-A	LDK-50.0-104.1-C
Manufacturer	Asphericon	CVI	Thorlabs	CVI
f_{eff} [mm]	15	150	100	-100
diameter [mm]	18	50	50	50
glass type	S-LAH64	N-SF10/N-BAK4	N-BK7	N-BK7

Table 2.2: The first lens is an aspheric lens inside of the vacuum chamber, the second lens is a cemented achromatic lens, the third lens is plano-convex singlet, and the forth lens is a bi-concave lens.

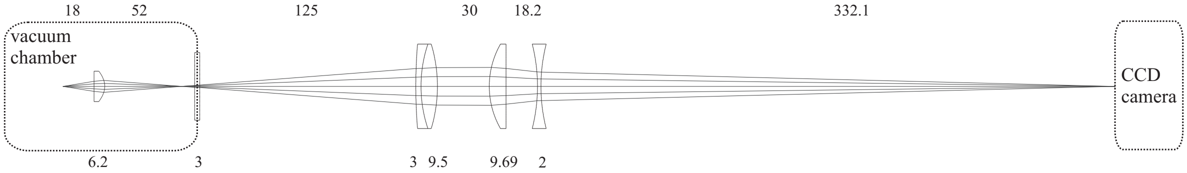

Figure 2.5: The imaging system consists of an aspheric lens inside of vacuum chamber (on the left) and a objective that corrects for the aberrations (see text). The numbers in the top row represent the spacings between the lenses in mm, while the numbers in the bottom row correspond to the glass thickness'. We assumed a window thickness of 3 mm.

were fixed to the closest commercially available lens. The designed configuration has a magnification of 6.4. We also expect near-diffraction limited performance in a field of view $< 50\,\mu$m around the optical axis. Note, that the performance and the magnification strongly depend on the precise positioning of the lenses relative to each other and also relative to the optical axis. We used a commercial cage-system[3] to mount the lenses, which simplifies the alignment of lenses with respect to each other. We set up a test configuration to determine the resolution of the imaging system consisting of an aspheric lens (with identical specifications as the one which is inside of the chamber) and the new objective. The resolution of the new objective was measured using a USAF 1951 test target, the new imaging system resolved 228 line pairs per inch corresponding to a resolution below $5\,\mu$m. The actual magnification of imaging with the new objective was determined using the optical pumping light and the fluorescence of the guided atoms. The measured magnification amounts to 6.6 which is in reasonable agreement with the computer simulation.

Oscillation frequencies

We measured the oscillation frequencies of the trapping potentials by exciting oscillations and recording position and size of the atomic cloud as a function of time. We applied a kick i.e. an abrupt change of the potential to excite the oscillations. As seen in figure 2.6, the radial size of the cloud (quadrupole mode) oscillates with twice the frequency of the position oscillation (dipole mode). We extracted the value ω of the frequencies using $x(t) = \cos(\omega \cdot t + \phi)\exp(-t/\tau) + x_0$ as a fit-function. Radial oscillation frequencies are defined by the confinement of the optical dipole trap only[4]. For axial oscillation frequencies $\omega_z = \sqrt{\omega_{z,\mathrm{ODT}}^2 + \omega_{z,\mathrm{MT}}^2}$ the contributions of the magnetic trap $\omega_{z,\mathrm{MT}}$ and the ODT $\omega_{z,\mathrm{ODT}}$ need to be measured independently. We used the magnetic potential in

---

[3] Thorlabs

[4] The magnetic anti-trapping in x-direction as well as the effect of the gravity and the magnetic trapping in y-direction can be safely neglected for the experimental parameters used in this work.

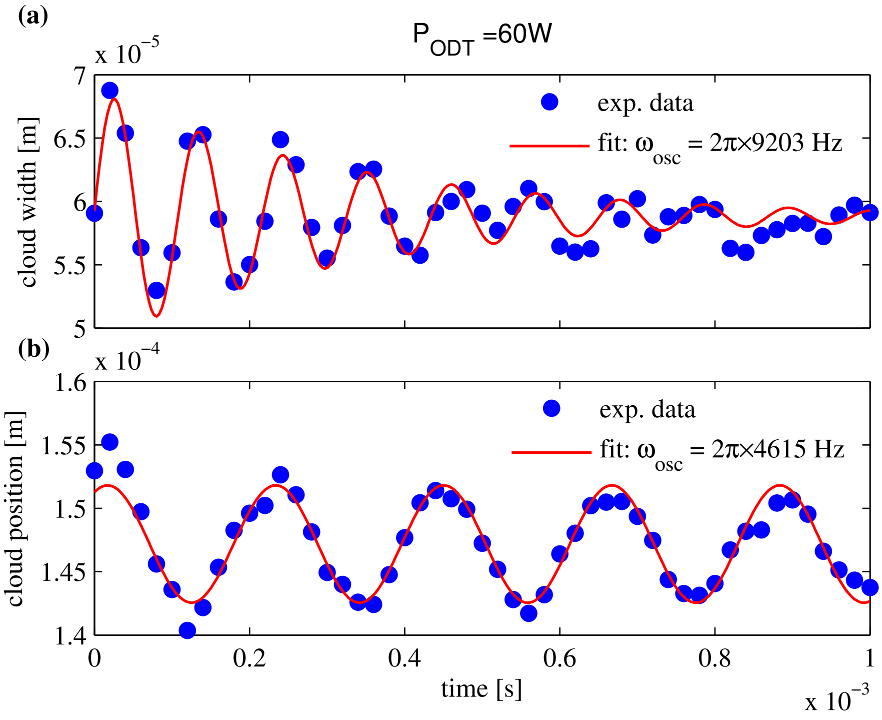

Figure 2.6: Trap oscillation in radial direction.

order to excite oscillations in axial direction. The axial oscillation frequency is dominated by the magnetic confinement in the case of the conventional loading, that is when the barrier coils current is $I = 1.15\,\mathrm{A}$, and was measured to be $\omega_z \approx \omega_{z,\mathrm{MT}} = 2\pi{\times}295\,\mathrm{Hz}$. For the measurements in chapter 4 the magnetic trap was switched off and the confinement was only given by the optical dipole trap. We obtained $\omega_z = \omega_{z,\mathrm{ODT}} = 2\pi \times 40\,\mathrm{Hz}$ at $P_{\mathrm{ODT}} = 90\,\mathrm{W}$.

Characterization of the atomic cloud

The amount of absorbed light is directly converted into the number of atoms in the imaged region. The temperature of the sample is obtained from the size of the atomic cloud. When the in-trap density distribution is not known, the expansion velocity is used to calculate the thermal energy. The expansion velocity is extracted from a series of pictures with increasing TOF. This method is described in detail in [Falkenau, 2011]. The advantage of this method is that it works without any assumption and can be applied to any initial geometry. However, one cannot deduce the temperature from a single picture, therefore for each measurement where temperature is an important quantity a large amount of data has to be acquired. In the case of a thermal sample trapped in a harmonic potential, the temperature can be calculated from a single picture, provided the oscillation frequencies of the potential are known [Ketterle et al., 1999].

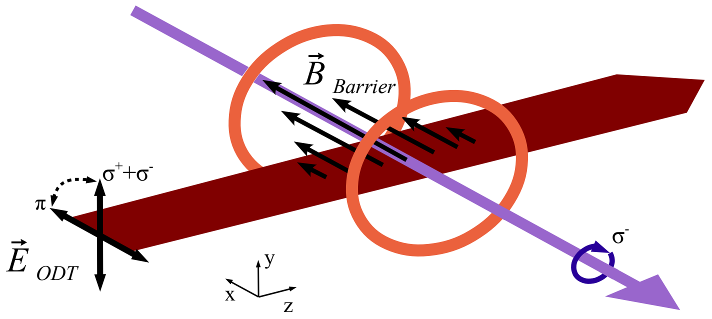

Figure 2.7: Polarisation of the ODT relative to the magnetic field of the barrier potential.

2.2 Improving loading with ODT-polarisation

In previous work, the modelling of the continuous loading process included only the depth of the optical dipole trap as a parameter for the calculation of the evaporation rate. The process of optical pumping and the corresponding time scales were not considered. However, it is clear that the amount of remaining longitudinal energy not only depends on the initial velocity spread (which determines the position of the classical turning point) but also on the duration of the optical pumping event. Here, we investigate experimentally the performance of the loading as a function of the effective detuning of the pumping light and the polarisation of the ODT. The detuning depends on the magnetic field of the barrier potential (Zeeman-shift) as well as on the intensity of the ODT (ac-Stark shift), as shown in figure 2.9.

2.2.1 Differential Zeeman shift

Due to a minor mismatch of the Landé factors between the ground state ($g = 2.0018$) and excited state ($g' = 1.917$) the detuning arising from the differential Zeeman-shift effectively depends on the magnetic sub-state. In our case, at $B_0 = 12\,\mathrm{G}$ the σ^- transition from $m_\mathrm{S} = +3$ is shifted by 36.5 MHz to the red, whereas from $m_\mathrm{S} = -2$ it is shifted by 29.3 MHz. This difference of 7.1 MHz is larger than the line-width of the transition and implies that both transitions cannot be in resonance with one narrow-line laser at the same time.

2.2.2 Differential ac-Stark shift

The ac-Stark shift of the ground state is equivalent to depth of the ODT. Since the electronic ground state is a spherically symmetrical $^7S_3$ state, in the first order approximation, the trap depth does not depend on the polarisation of the ODT nor on the magnetic sub-state of the atom. However, the coupling of the excited $^7P_3$ state to the ODT strongly depends on its polarisation. Therefore, the resulting differential

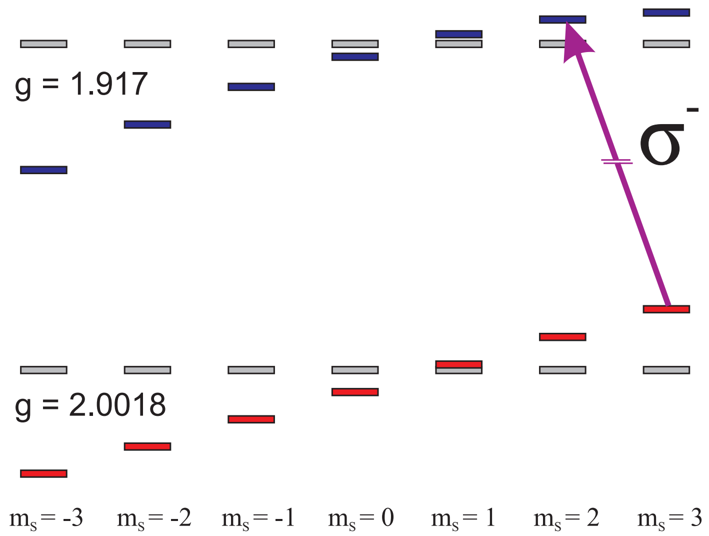

Figure 2.8: Zeeman sub-states of the ground and the excited state. The calculated shifts include Zeeman shift from a magnetic field $B_0 = 12\,\mathrm{G}$ and an ac-Stark shift from an ODT at $P = 90\,\mathrm{W}$ and polarized along the magnetic field.

ac-Stark shift which is being probed by the optical pumping light equally depends on the polarisation of the ODT and the magnetic sub-state, as shown in figure 2.9.

In the case of parallel polarisation (π-ODT) the total shift varies between -22 MHz and -61 MHz. This means that the optical pumping runs out of the resonance when atoms descend into lower sub-states, or starts off-resonantly. Either way, the optical pumping cannot be considered instantaneous, and while not in the lowest magnetic sub-state ($m_S = -3$) atoms can re-gain some of the directed kinetic energy from their propagation in the barrier potential. As we know from the analysis of the rate equations (see 2.1.4), the initial axial temperature contributes significantly to two-particles losses from binary collisions, limiting the maximal number of trapped atoms. For orthogonal polarisation ($\sigma^+ + \sigma^-$-ODT) the total shift varies weakly with the magnetic sub-state. The largest difference is only slightly larger than the atomic line-width.

From these calculations we expect the optical pumping to be faster and more efficient in the case of the orthogonal polarisation of the ODT, leading to a larger number of atoms and a lower temperature in the steady state.

2.2.3 Results

The polarisation of the ODT-laser is linear and can be rotated using a $\lambda/2$ retardation plate in the $x - y$ plane at the position of the atoms as shown in figure 2.7. We choose the magnetic field of the barrier potential $\vec{B}_{Barrier}$ as the quantization axis for the atoms. In this case, when the ODT-polarisation is parallel to $\vec{B}_{Barrier}$, the ODT couples to the π transitions of the atoms, whereas when the ODT-polarisation points in y-direction

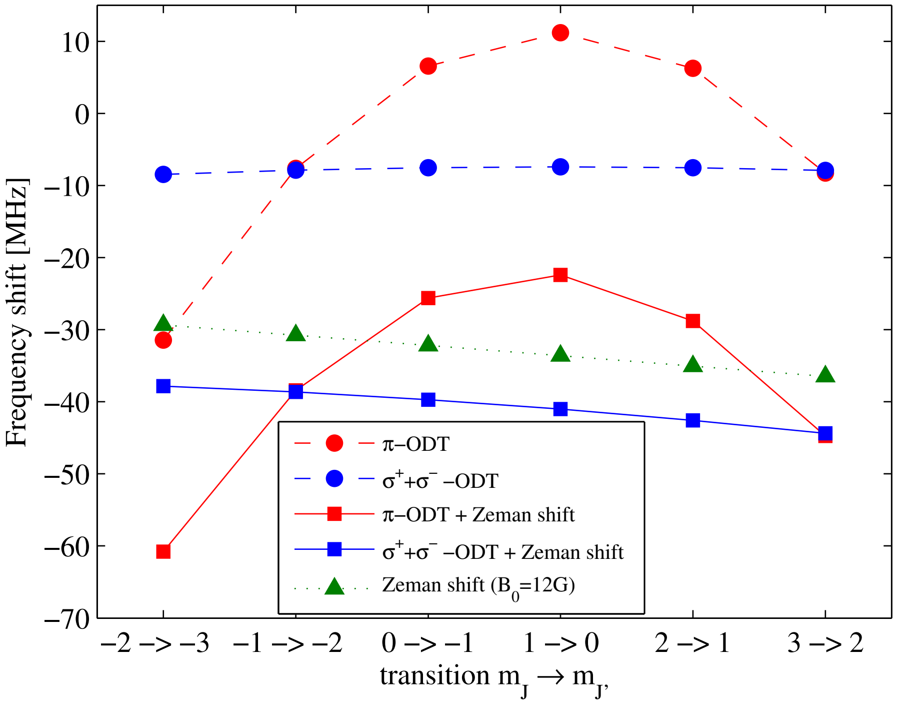

Figure 2.9: Calculated differential shifts of the optical pumping frequency for the σ^- transitions from different magnetic sub-states (denoted in the x-axis). As explained in the text, the Zeeman shift (triangles) varies because of a mismatch of the Landé factors. Circles denote the differential shift induced by the ODT for parallel and orthogonal polarisation with respect to the quantization axis. Squares represent the combined shift. Optical pumping is considered optimal when transitions from all magnetic sub-states are within the line-width of 5 MHz.

and is orthogonal to the magnetic field, it can be decomposed in circular components that couple to $\sigma^{\pm}$ transitions.

We measured the number of atoms and the temperature of the fully loaded trap as a function of the detuning of the optical pumping light for different polarisations of the ODT. In particular, we compare the parallel and orthogonal polarisation in figure 2.10. The shaded regions denote the calculated resonance conditions for parallel (π-ODT) and orthogonal (σ^++σ^--ODT) polarisations, also plotted in figure 2.9. The number of atoms peaks for both configurations at a detuning of -60 MHz. Changing the polarisation from parallel to orthogonal improves the number of atoms by 50%, while the temperature is slightly reduced. These results are in qualitative agreement with the consideration on the dynamics of optical pumping described above. Faster optical pumping into the dark-state in the case of orthogonal polarisation would lead to a reduced excess kinetic energy in longitudinal direction. As a consequence, the continuous evaporation at a lower temperature is more efficient, allowing for larger steady state number of atoms.

However, the measured curves are not symmetric around the calculated resonance.

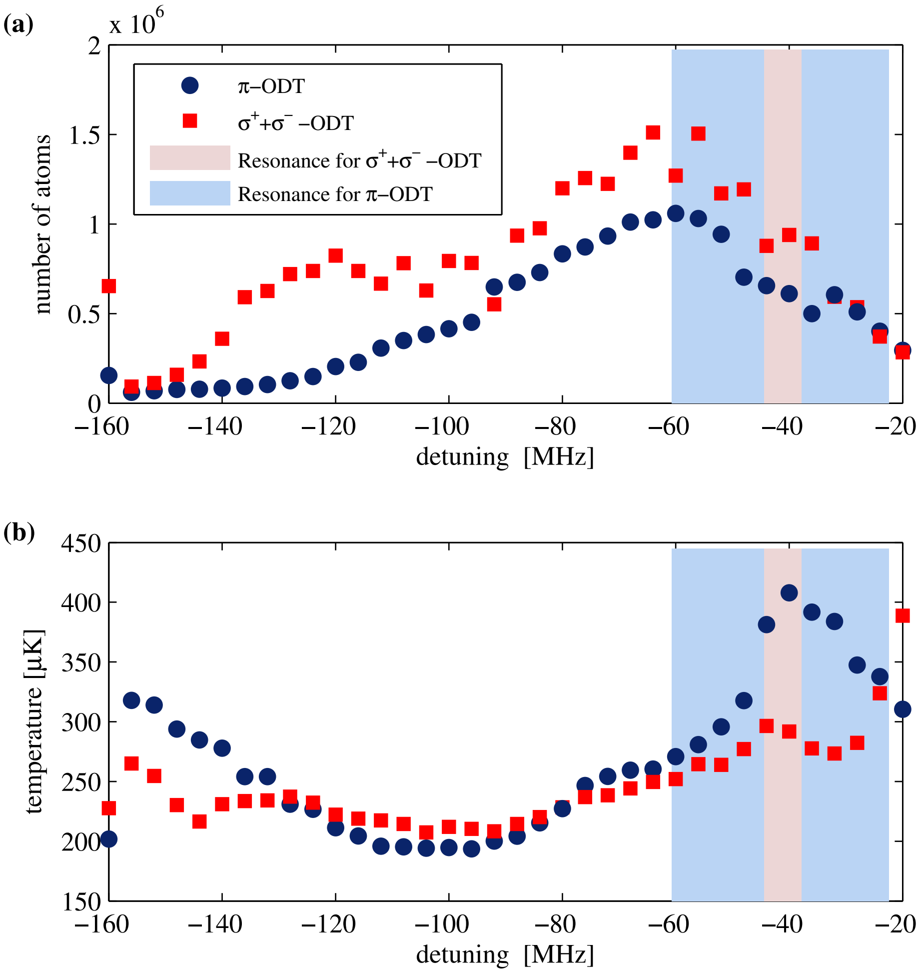

Figure 2.10: Steady state number of atoms (a) and temperature (b) are plotted versus the detuning of optical pumping (at constant intensity). Different ODT polarisations are denoted by circles (π) and squares ($\sigma^+ + \sigma^-$).

The shown data cannot be explained by a model for optical pumping relying on the detuning from resonance only. As we show in chapter 4, excited-states collisions and the associated heating and atom losses play a major role in optical cooling at high densities. Therefore, excited-state collisions may also be important during the loading process, since similar densities are achieved.

3 Sisyphus cooling in a continuously loaded trap

The continuous loading mechanism introduced in the previous chapter is in principle very general and can be applied to other kinds of beams. However, it strongly relies on a slow, high-flux, and transversely cold beam – conditions that are difficult to obtain for an arbitrary beam. Especially, when a single slowing step is not sufficient to dissipate all the kinetic energy, the loading mechanism breaks down.

As we have seen in section 2.2, strategies that reduce the remaining longitudinal kinetic energy, effectively improve the maximal number of atoms, the temperature, and thereby the phase-space density of the atoms in the trap. One could further improve the transfer of the atoms into the trapped dark-state by reducing the size of the optical pumping beam. However, the major source of excess longitudinal energy is the initial velocity spread of the atomic beam. For example, a beam with a mean velocity $v_0 = 1\,\mathrm{m/s}$ and a velocity spread $\delta v = 0.2\,\mathrm{m/s}$ has a temperature $T = 125\,\mu\mathrm{K}$ in the co-propagating frame of reference. Ideally, the barrier and optical pumping remove a fixed amount of kinetic energy (lets say $E = \frac{mv_0^2}{2}$), the remaining velocity spread is now given by

$$v' = \sqrt{v_0 \cdot \delta v + \delta v^2} \tag{3.1}$$

and corresponds to a temperature $T = 706\,\mu\mathrm{K}$.

We would like to force the atoms into repeating the slowing step as many times as it is necessary in order to dissipate the remaining energy, as it is shown in figure 3.1. We make use of the intermediate states that are only weakly trapped by the magnetic field of the barrier coils (emphasised in the zoomed region in figure 3.1). The additional slowing steps take place inside of the trap: the loaded atoms are slowed by moving axially away from the trap minimum, on their way the internal state is changed by applying a radio frequency field (RF). As a consequence the atoms do not re-gain the full kinetic energy they had at the bottom of the trap. Finally, when the atoms cross the optical pumping light they are pumped back into the ground state and the potential energy is dissipated by the photons. The iteration of these cooling steps inside of the trap is commonly known as Sisyphus cooling since it reminds the greek myth.

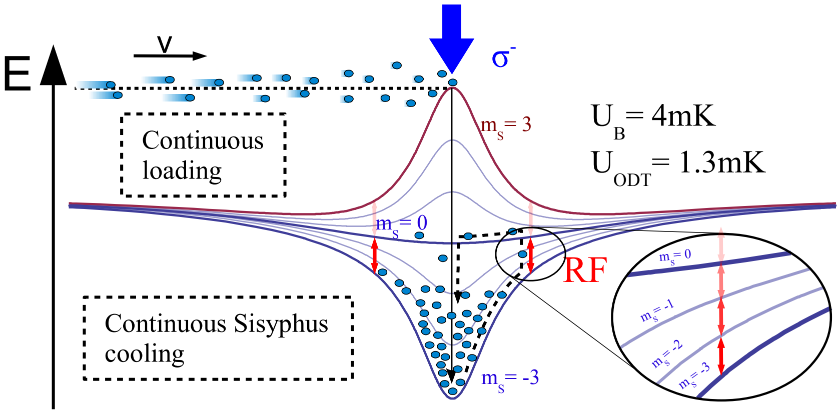

Figure 3.1: Continuous loading and simultaneous cooling mechanisms are depicted. The significant part of the longitudinally directed kinetic energy of the atomic beam is dissipated as described in figure 2.3. The remaining longitudinal energy is further reduced by RF-induced Sisyphus cooling inside the hybrid trap. Each time a trapped atom climbs up the magnetic potential to the regions of magnetic fields where it is resonant to the radio frequency (enlarged region), its gained potential energy is partly converted into Zeeman energy. The Zeeman energy is eventually dissipated when the atom returns to the centre of the potential by the optical pumping light.

Outline

In this chapter, we present a scheme combining continuous loading from a guided beam with simultaneous Sisyphus cooling [Volchkov et al., 2013]. First, we discuss various implementations of this cooling method known in the literature, followed by the description of the computer simulation developed to predict and analyse the cooling results. We present experimental data showing the effect of the Sisyphus cooling in addition to the continuous loading in different regimes. As a result, the constraints on the temperature and the flux of the beam necessary to enter collisional regime can be drastically relaxed. We can reduce the incident flux and the initial PSD by several orders of magnitude and still reach favourable conditions for subsequent evaporative cooling. Additionally, we show that technical constraints, in particular the height of the repulsive potential as well as the depth of the optical dipole traps can be reduced as well.

3.1 A brief history of Sisyphus cooling

The original idea of Sisyphus cooling involving state dependent potentials and optical pumping was proposed in [Pritchard, 1983]. Pritchard suggested the use of different hyper-fine states of sodium to realize state-dependent magnetic trap potential. The Sisyphus cycle consists in moving up a steep potential, a transfer into a less confined state close to the turning point, and optical pumping back to the original state at the bottom of the potential. For a purely magnetic trap the atoms have to be in the low-field seeking state. This scheme of Sisyphus cooling in a magnetic trap was further theoretically studied in [Janis et al., 2005]. In this work, different Zeeman states of the F=2 manifold of rubidium were used. The disadvantage of using the Zeeman states instead of hyper-fine states is that transitions to untrapped states become possible. Hence, the results of the latter work indicated that the mechanism is limited by the probability of losing atoms when the cooling rate is increased. In addition, the size and position of the optical pumping beam are crucial for the Sisyphus cooling in a magnetic trap. Ideally, the optical pumping should occur at the very bottom of the potential and nowhere else, since premature pumping would reduce the efficiency of the cooling cycle.

State dependent potentials can be also realized in an optical potential as shown in [Miller et al., 2002] using rubidium atoms. In order to obtain a useful difference between the potentials, the detuning of the optical dipole trap should be on the order of the fine-structure splitting. For this reason, the circularly polarized ODT was detuned only by a few nm to the red of the D1 line. As a consequence, atoms in the stretched $F = 2, m_F = 2$ state do not couple to the $5\mathrm{P}_{1/2}$ state and the potential is only given by the coupling to the relatively far detuned $5\mathrm{P}_{3/2}$ state. As opposed to this, atoms in $F = 2, m_F < 2$ states strongly couple to the nearby transition and experience a much deeper optical potential. The Sisyphus cycle begins by transferring atoms via a radio frequency field from the $m_\mathrm{F} = 2$ to the $m_\mathrm{F} = 1$ state. The position of this resonance is determined by the frequency of the RF field and should be as close to the bottom as possible, otherwise the cooling effect can turn into a heating effect. Optical pumping back to $m_F = 2$ occurs probabilistically by absorbing a photon from the ODT itself. The position where the optical pumping takes place cannot be controlled directly. The scattering time should be around the oscillation time.

Both approaches described above have an important drawback. The motion of atoms consists of three dimensional orbitals in the trap and the probability of finding an atom at the bottom of potential tends to zero. It means that only a very small fraction of atoms is involved in the cooling process. In order to increase this fraction one has to enlarge the region where the atoms interact either with the optical pumping light (for the magnetic trap) or the RF field (for the ODT), thereby compromising the efficiency of the cooling, and eventually limiting the lowest attainable temperature.

Temperatures around a few μK were reached by restricting the Sisyphus cooling in one dimension with the help of gravity. In gravitational Sisyphus cooling pioneered in [Newbury et al., 1995], the small difference in magnetic moments between the rubidium states $F = 2, m_F = 1$ and $F = 1, m_F = -1$ leads to a displacement of the associated magnetic potential minima. Coherent transfer between the two states is driven by a combined microwave and radio frequency two-photon process. Again, optical pumping is used to dissipate the potential energy. The optical counterpart is the so-called

GOST (gravito-optical surface trap)[Ovchinnikov et al., 1997], in which inelastic reflections from an evanescent light wave closely above a dielectric surface efficiently extract energy from the atomic motion. The caesium atoms in GOST are trapped by a blue-detuned hollow beam in direction parallel to the surface. Despite the low temperatures, the densities obtained in these experiments were not sufficient to enable subsequent evaporative cooling.

In a recent experiment [Zeppenfeld et al., 2012] Sisyphus cooling was applied to electrically trapped polar molecules. Here, the cooling so far was limited by the long life time of the excited state and therefore only a small number of Sisyphus cycles. This experiment demonstrates the general applicability of the Sisyphus cooling scheme.

In all of the works discussed above, the Sisyphus cooling was performed in a *pulsed operation*. In other words, a specific trap was first loaded with particles and then cooled for a certain cooling time. A prominent example of *continuously operated* Sisyphus cooling is the polarisation gradient sub-Doppler cooling encountered in magneto-optical traps [Dalibard and Cohen-Tannoudji, 1989]. The state-dependent sinusoidal potential arises from different couplings to the periodically changing polarisation of the light. Optical pumping between the sub-states forces the atoms to climb on average more potential hills up then down. The dissipated energy corresponds to the light shift difference for the respective sub-states. This cooling mechanism works efficiently only for a specific velocity class and is limited by the recoil energy.

3.2 Simulation of the loading and cooling

The model based on rate equations discussed in section 2.3 is in good agreement with the continuous loading mechanism and the evaporative cooling. The numerical simulation of this model helped us to understand the impact of the evaporation on our loading mechanism as well as the importance of the hybrid potential for the forced evaporative cooling. Unfortunately, the various parameters and aspects of the RF-induced Sisyphus cooling cannot be incorporated into the model by adding some terms to the rate equations.For this reason, we have developed a so-called molecular dynamics simulation that allows us to simulate individual atoms and their interaction with the RF-field, the optical pumping light, and with each other.

3.2.1 Molecular dynamics

Generally, molecular dynamics (MD) can be regarded as a bottom-up approach to the modelling of a system (whereas rate equations describing macroscopic quantities can be viewed as a top-down approach). Central ingredient of MD is the interaction between the simulated particles. Furthermore, the time evolution of the given system is discretized in small time steps over which the forces acting on the particles can be regarded as constant. The integration of the equations of motions is then straightforward. Vast literature can be found on MD as it is widely applied for simulation of fluid dynamics, transport, material properties, bio-molecules, etc. (see references in [Allen, 2004]). Following individual particle gives the possibility to include conditional statements, depending on individual properties of the particles. Here, we first focus on the implementation of the state-dependent (external) potentials and state-changing mechanisms without interactions (collisions) to obtain an idea about the motion of the particles. Subsequently, we add a loss mechanism simulating density and light dependent losses and finally extend the simulation with elastic collisions between the particles in order to bring the system into thermal equilibrium.

3.2.2 Ingredients of a simulation

The initial state of the system can be either a thermal cloud in the dark state or an empty trap. The thermal cloud is created by placing a defined number of particles into the trap according to a Gaussian position and momentum distribution for a given temperature. The simulation of each iteration step with a typical size of $\Delta t = 1\mu s$ consists of the following sequence:

1. Remove particles due to background loss
2. Add particles due to loading from the beam
3. Remove particles that escape radially (or axially)
4. Propagate equations of motion
5. Detect RF-resonance crossing and calculate RF-transitions
6. Calculate outcome of optical pumping
7. Light assisted collisions: remove particles
8. Perform thermalization: compute elastic collisions

Ensemble averages are calculated in variable (simulated) time intervals (typically every 10 ms), which we then compare to experimental data. In the following the different sub-routines of the simulation are described in detail.

3.2.3 Equations of motion

The simulated particles are described by their position $\vec{r} = (x, y, z)$ and velocity $\vec{v} = (v_x, v_y, v_z)$ vectors as well as their internal state, corresponding to the magnetic substate m_{S}. The potential landscape is given by separated radial and axial confinements.

The radial confinement is a harmonic potential with oscillation frequency ω_r that only depends on the power of the ODT. The axial potential arises from the magnetic field variation and is approximated by a harmonic potential with oscillation frequency ω_z for the atoms in the ground state with $m_\mathrm{S} = -3$ (as given in section 2.1.5). Atoms in other m_S states see a different potential curvature which results in a less trapping or even anti-trapping potential. We employ the 'velocity-verlet' method to propagate the equations of motion [Swope et al., 1982]:

$$\vec{r}_{new} = \vec{r} + \vec{v} \cdot \Delta t + \vec{a} \cdot \Delta t^2/2$$
$$\vec{a}_{new} = (-\omega_r^2 \cdot \vec{r}_{new})_{x,y} + (\tfrac{1}{3} m_\mathrm{S} \cdot \omega_z^2 \cdot \vec{r}_{new})_z$$
$$\vec{v}_{new} = \vec{v} + \vec{a} \cdot \Delta t/2 + \vec{a}_{new} \cdot \Delta t/2$$

Here, the expression $(\dots)_{x,y}$ denotes the x and y components of the acceleration $\vec{a}$, and $(\dots)_z$ denotes its z-component.

3.2.4 Multi-level Landau-Zener problem

In each time step of the MD simulation several conditions are verified. The detuning $\delta(t)$ to the RF resonance[1] is calculated based on the magnetic field at the new position of the atom and compared to the detuning $\delta(t - \Delta t)$ from the previous time step. When the sign of the detuning has changed, transition to a different internal state must be evaluated. In order to determine in which state the atom crossing the resonance will end up the multi-level Landau-Zener problem has to be solved.

Generally, analytic solutions for more then two levels are difficult to obtain, although some special cases haven been solved exactly [Shytov, 2004]. The lack of a hyperfine-structure in ^{52}Cr leads to a purely linear Zeeman-shift. In particular it means that the energy splittings between neighbouring sub-states are equal and that all sub-states are in resonance with the RF field at the same frequency. In fact, this case is known as the 'bow-tie'- configuration [Demkov and Ostrovsky, 2001]. As in the famous 2-level Landau-Zener model, the outcome of the transition can be described by the adiabaticity parameter Γ_LZ

$$\Gamma_\mathrm{LZ} = \frac{\Omega^2}{\frac{d}{dt}\delta} \tag{3.2}$$

The coupling strength Ω is given by the amplitude of the RF field (simulation parameter). The time derivative of the detuning $\frac{d}{dt}\delta$ depends on the velocity of the atom and the slope of the magnetic field at the position of the resonance. Strong coupling or slow change of detuning lead to an adiabatic transition. In the extreme case it means flipping an atom from the $m_\mathrm{S} = -3$ to the $m_\mathrm{S} = 3$ state. At low coupling strength, an atom may cross the resonance without changing its internal state. We calculated the transition

---

[1] The detuning depends on the z-coordinate because of the magnetic trapping potential.

probabilities, by numerically solving the time-dependent von-Neumann equation

$$\imath\hbar\frac{\partial\rho}{\partial t} = [H,\rho] \tag{3.3}$$

with ρ being the density matrix and H the Hamiltonian of the symmetric 7-level system

$$H = \begin{pmatrix} -3\delta & \Omega/2 & 0 & 0 & 0 & 0 & 0 \\ \Omega/2 & -2\delta & \Omega/2 & 0 & 0 & 0 & 0 \\ 0 & \Omega/2 & -\delta & \Omega/2 & 0 & 0 & 0 \\ 0 & 0 & \Omega/2 & 0 & \Omega/2 & 0 & 0 \\ 0 & 0 & 0 & \Omega/2 & \delta & \Omega/2 & 0 \\ 0 & 0 & 0 & 0 & \Omega/2 & 2\delta & \Omega/2 \\ 0 & 0 & 0 & 0 & 0 & \Omega/2 & 3\delta \end{pmatrix} \tag{3.4}$$

The time dependence was assumed to be linear[2] $\delta(t) \propto \frac{d}{dt}\delta \cdot t$ and the integration limits t_0 and t_f were chosen such that $|\delta(t_0)| = |\delta(t_f)| \gg \Omega$. Figure 3.2 shows exemplary the crossing of the resonance with $\Gamma_{\mathrm{LZ}} = 1$. Initially, only the $m_{\mathrm{S}} = -3$ state (red line) is populated, when the resonance is crossed at $t = 100$ all sub-states oscillate, the final populations correspond to the transition probabilities. Prior to performing the MD simulation, we created a look-up-table (LUT) for all magnetic sub-states in the range of $\Gamma_{\mathrm{LZ}} \in \{1/400, 100\}$ covering the strongly diabatic and adiabatic regimes, as shown for the $m_{\mathrm{S}} = -3$ state in figure 3.3.

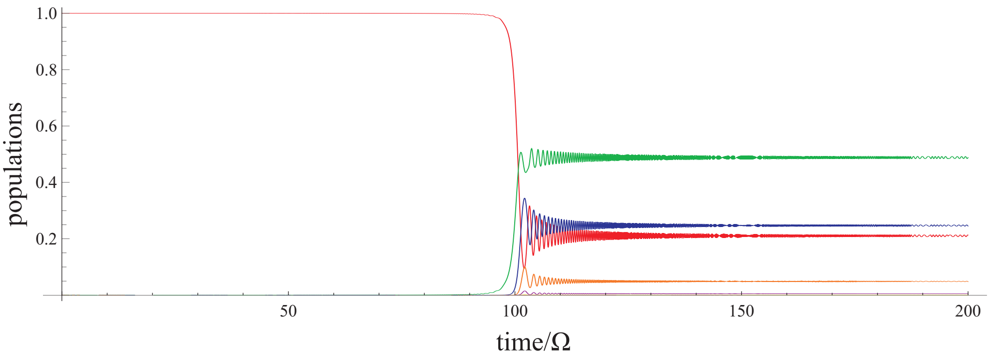

Figure 3.2: Landau-Zener transition with $\Gamma_{\mathrm{LZ}} = 1$, starting in the $m_{\mathrm{S}} = -3$ state (red line). Amplitudes of $m_{\mathrm{S}} = -2$, $m_{\mathrm{S}} = -1$, and $m_{\mathrm{S}} = 0$ states are displayed by green, blue, and orange lines, respectively. The time axis is given in units of $1/\Omega$.

In the MD simulation of the Sisyphus cooling process we use the Monte-Carlo method based on probabilities from the LUT to decide to which state an atom is transferred. First, we determine the value of the Landau-Zener parameter by computing the rate

---

[2] Hereby we neglect the fact that atoms are actually climbing up or rolling down the magnetic potential and are necessarily subjected to a force.

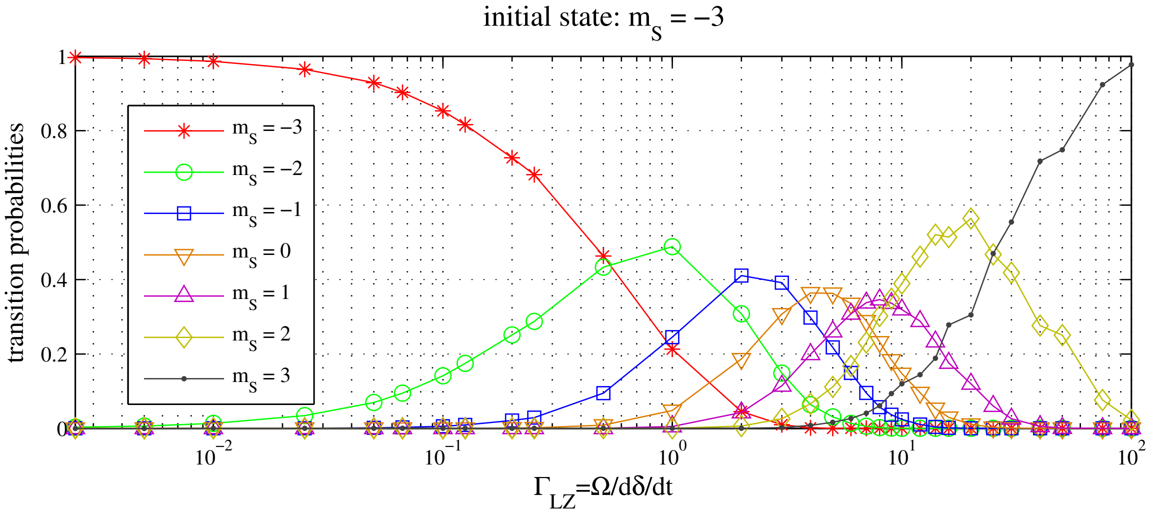

Figure 3.3: Graphical representation of the look-up-table for transition probabilities from the $m_\mathrm{S} = -3$ state. Linear interpolation between the calculated values is used in order to obtain the transition probabilities for arbitrary adiabaticity parameter Γ_LZ.

of change of the detuning: $\frac{d}{dt}\delta = (\delta(t) - \delta(t - \Delta t))/\Delta t$. Then, we use a randomly generated number[3] between 0 and 1 to assign the new state, as depicted in figure 3.4.

3.2.5 Optical pumping

Polarisation of the atomic sample via optical pumping can be implemented by setting the internal state of each atom that passes the $z = 0$ plane to $m_\mathrm{S} = -3$. The computation effort of this implementation is minimal and physically it corresponds to a very strongly focused optical pumping beam. In the actual experiment the optical pumping beam has a Gaussian intensity distribution along the axial direction of the trap with a waist of $w_0 = 140\,\mu$m. Therefore the propagation of atoms within the light field as illustrated in figure 3.5 has to be taken into account. We model the optical pumping by calculating in each time step the probability of being excited for each simulated atom. We calculate the individual scattering rate depending on the local intensity, the local detuning, the polarisation of the light, and the internal state of the simulated atom. The scattering rate multiplied by the time step size Δt gives the probability of being excited. The excitation takes place if this probability is larger than a random number between 0 and 1. Additionally, we use Clebsch-Gordon coefficients to determine in which state the atom is pumped.

Light assisted losses are modelled by counting the number of atoms inside a sphere with a certain radius around the excited atom. When more than one particle is found all atoms from that sphere (including the excited atom) are immediately removed from

---

[3] Uniformly distributed pseudorandom numbers.

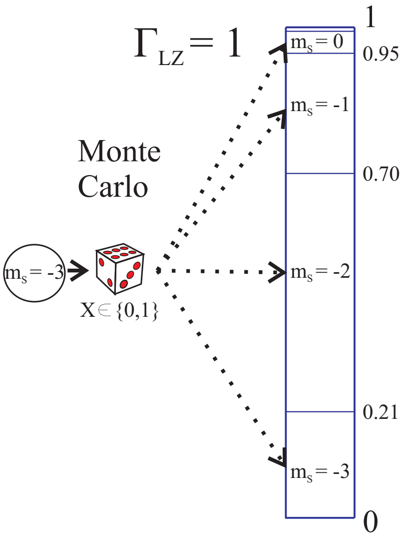

Figure 3.4: The outcome of a RF-transition is determined by a random number which is compared to bins of different sizes, corresponding to the probabilities for the given Γ_{LZ}. In this example the bins have the sizes according to the look-up-table values for $\Gamma_{\mathrm{LZ}} = 1$.

that trap. The size of the sphere is a free simulation parameter and defines the strength of this loss channel.

3.2.6 Adding and removing atoms

The total number of simulated particles is fixed during the course of a simulation. Resizing large arrays by adding or removing entries involves significant computational overhead which we avoid by handling arrays of fixed size. An empty trap is initialized by placing all particles in the low-field seeking state $m_{\mathrm{S}} = 3$ at the coordinates $(x, y, z) = (0, 0, 0.1)$m with zero velocity $(v_x, v_y, v_z) = (0, 0, 0)$m/s. These particles are considered outside of the trap (*lost*) and they do not contribute to the computation of the ensemble averages. Due to the harmonic potential in the axial direction the *lost* particles are accelerated away from the centre, however the axial position is reset to 0.1 m in each time step when it should exceed this value[4].

The flux is a simulation parameter that gives the rate at which particles are given a chance to be loaded into the trap. The loading of a particle starts by assigning one *lost* particle the radial position and the radial velocity according to the thermal distribution in a harmonic trap with given trapping frequency (ω_r – for the position) and a predefined radial temperature [5]. The axial position coordinate is set to $z_0 = -5 \times 10^{-4}$ m, while the axial velocity is set to $v_z = v_0 + \delta v \cdot \mathrm{randn}$, with δv being the velocity spread multiplied by a normally distributed random number. The average velocity can be set to a fixed

---

[4] This trick allows computing of the new position and velocity variables for all particles at once regardless whether they are lost or not, without running into very large entries. It turns out that in this way the computational time is strongly reduced compared to sorting trapped and lost particles first and then propagating only the trapped ones.

[5] This temperature is on the order of 400-500 μK and has been determined experimentally.

Figure 3.5: Initializing and optical pumping of a particle. The potential curves are off-set for the purpose of illustration. The particle is placed at the $z = -0.5\,\mathrm{mm}$ position. Average velocity v_0 can be set to a fixed value or calculated to match the potential height. Depending on the velocity spread δv and optical pumping settings (denoted by the broad violet arrow), the particle may be reflected or transmitted by the barrier potential without optical pumping (dashed arrows). The optical pumping is simulated based on the intensity and detuning of the optical pumping light, which determine the probability of an excitation. The particle is propagated in the potential according to the new internal state after an optical pumping event.

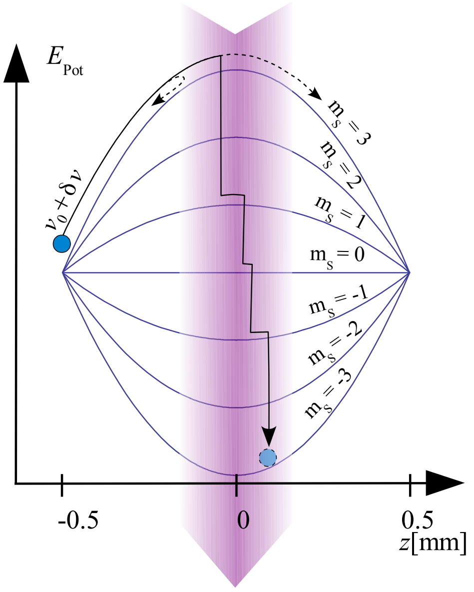

value or calculated using $v_0 = \omega_z \cdot z_0$, then it corresponds to the velocity necessary to reach the maximum of the potential barrier, as shown in figure 3.5. Once the particle is 'initialized‘, it propagates towards the centre of the trap and is treated like any other particle. The actual transfer into the trap takes place in the vicinity of the optical pumping beam as described in section 3.2.5. This implementation allows simulation of the loading at a lowered barrier potential. In general, the resulting loading rate does not only depend on the flux but also on the optical pumping parameters, the velocity and the barrier height.

Particles are removed from the trap in three cases. First, losses through collisions with the background gas are simulated by removing random trapped particles at times corresponding the loss rate. Second, particles can leave the hybrid trap in radial direction by reaching radial potential energy greater than the depth of the optical dipole trap. Most of the times, this event is preceded by an elastic collision. Furthermore, atoms can leave the hybrid trap in the axial direction following a RF transition into an untrapped magnetic sub-state. Third, simulation of light-assisted collisions also results in the loss of particles. In all cases, the loss is implemented by assigning the particles the initial coordinates $(x, y, z) = (0, 0, 0.1)$m, $(v_x, v_y, v_z) = (0, 0, 0)$m/s (see above) and the state $m_S = 3$.

3.2.7 Thermalization

Elastic collisions are included in the simulation in order to provide a mechanism for thermalization, which also keeps Sisyphus cooling in the game even when the average thermal energy of the particles is less than the energy required to reach the RF-resonance. We combine two simplifications to reduce the computational workload. In the experiment, the number of atoms typically loaded into the optical dipole trap varies between 10^5 and 2×10^6. Instead of simulating such a large number of particles, we use macro-particles as described by Bird [Bird, 1994]. Each macro-particle substitutes 100 to 1000 real particles. The collisional cross-section of a macro-particle is scaled by the square root of the number of real particles it represents. Thereby, the total collision rate stays unchanged compared to an equivalent system composed of real particles [Wu and Foot, 1996]. The second simplification consists in taking advantage of the momentum distribution of thermal particles in a harmonic potential, which does not depend on the position. We randomly pick pairs of particles that are subjected to 'non local‘ collisions. The number of pairs is based on the total scattering rate that is calculated from the number of particles and their average thermal energy. Each collision obeys the classical equations for conservation of energy and momentum. The given simplification are valid only for an ensemble close to thermal equilibrium and outside the hydrodynamic regime. One straight-forward possibility to avoid this limitation is to check the distances between all pairs of particles for collisions [Griesmaier, 2006]. However, this would lead to a quadratic scaling of computational time as a function of particle number.

3.3 Experimental implementation

The inhomogeneous magnetic field is the same field that is used for slowing of the atoms and can be approximated by a quadratic expression around its centre by:

$$B(z) = B_0 - \frac{m\omega_z^2}{2 \times 6\mu_\mathrm{B}} z^2. \tag{3.5}$$

The oscillation frequency in axial direction ω_z always refers to the confinement experienced by the $m_\mathrm{S} = -3$ state, its dependence on the current of the barrier coils and ODT power is given by

$$\omega_z(I_\mathrm{BC}, P_\mathrm{ODT}) = 2\pi\sqrt{273^2\frac{I_\mathrm{BC}}{\mathrm{A}} + 4.22^2\frac{P_\mathrm{ODT}}{\mathrm{W}}}\mathrm{Hz} \tag{3.6}$$

The magnetic field maximum is given by $B_0(I_\mathrm{BC}) = I_\mathrm{BC} \times 10.82\,\mathrm{G/A}$. In the case of radial oscillation frequencies, for ODT power $P_\mathrm{ODT} > 10\,\mathrm{W}$ the measured frequencies are best fitted by a the expression (see section 2.1.5 for more details)

$$\omega_r(P_\mathrm{ODT}) = 2\pi \times 606\sqrt{\frac{P_\mathrm{ODT}}{\mathrm{W}}}\mathrm{Hz} \tag{3.7}$$

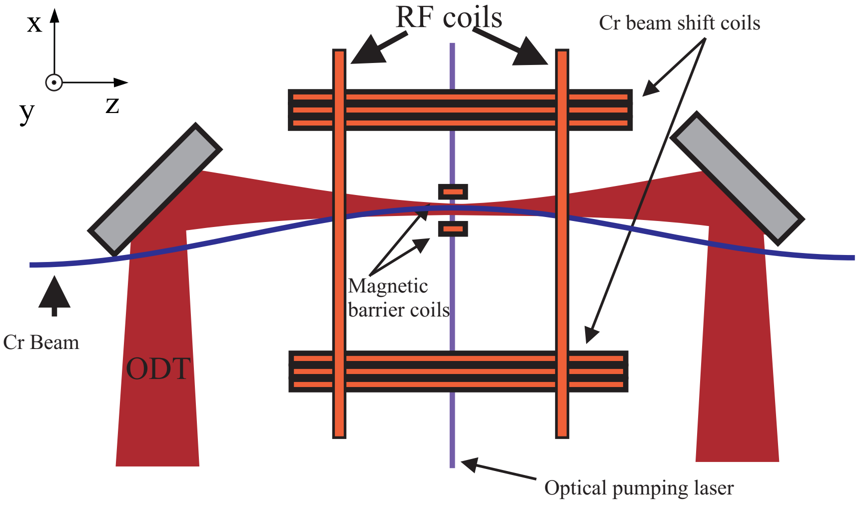

Figure 3.6: The quantization axis is given by the field of the magnetic barrier coils and points in x-direction. Single winding sqaure coils are located around the hybrid trap(between the magnetic barrier coils). The illustrated pair produces a magnetic field in z-direction. A second pair of similar coils produces a magnetic field in y-direction. The Sisyphus cooling is insensitive to which coil is used.

We applied a RF field via an antenna consisting of a single winding square coil with the edge length of 4 cm, approximately 1 cm away from the atoms. The coil was driven by a $P_{\max} = 250\,\mathrm{mW}$ frequency generator[6] without any impedance matching and produced an oscillating magnetic field in the z-direction at the position of the atoms, perpendicular to the quantization axis defined by the field of the magnetic barrier. The coils shown in figure 3.6 were not designed to act as antennas, therefore the frequency response in the range 1–40 MHz is not flat. However, the cooling results are very robust against switching between the available coils in z or y-direction. Wherever the RF power is indicated, in the following, it always refers to the output power of the frequency generator.

3.4 Evidence for Sisyphus cooling

In this section we experimentally study the Sisyphus cooling in different regimes. We restrict the loading time to values below 50 ms. At this short time scales, the density of the sample is low and collisions between atoms can be neglected. Under such conditions we can directly study the influence of the external parameters such as RF power and frequency and compare the data to the simulation. We find that for accessible experimental parameters *diabatic* transitions dominate the RF-cooling.

Increased amount of scattered light from the centre of the continuously loaded trap is observed on fluorescence images and constitutes a signature for the simultaneous

---

[6] Keithley 3390

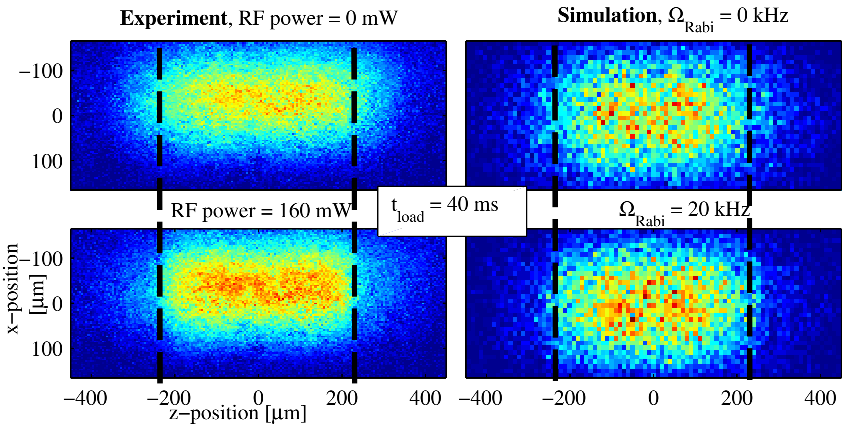

Figure 3.7: The emergence of the cut-off (dashed lines, guide to the eye) in the position distributions appears in the time-of-flight pictures taken after a loading time of 40 ms, when an RF field at 30 MHz is applied (lower row). The pictures in the left column are actual absorption pictures of atoms, while the right column pictures stem from a MD-simulation.

Sisyphus cooling. In steady state, the thermalization plays an important role, combined with RF-assisted Sisyphus cooling, the temperature is significantly reduced – far below the collisionless regime. Finally, we discuss how entering the hydrodynamic and density-limited regime reduces the efficiency of the cooling mechanism.

3.4.1 Collisionless regime

The RF-assisted Sisyphus cooling as shown in figure 3.1 is a single particle effect. As long as trapped atoms do not collide, each atom loaded into the trap performs its own cooling cycles. The axial kinetic energy is reduced in each Sisyphus cycle until the RF-region can no longer be reached, this leads to a cut-off in the momentum distribution. For the same reason we also expect a truncated position distribution.

Absorption images in figure 3.7 show the distributions of atoms after a TOF of 300 μs, integrated along the y-directions. Since the TOF does not exceed the oscillation period, what we see is the convolution of the position distribution with the momentum distribution. The loading time is set to $t_{\mathrm{load}} = 40$ ms. In the presence of the RF field at a frequency $f_{\mathrm{RF}} = 30$ MHz high energy atoms from the axial wings of the distributions are transferred below the resonance, that is towards the centre of the trap. This results in a box-shaped distribution. The vertical dashed lines indicate the position of the cut-off. Pictures on the right hand side originating from the computer simulation show the same signature.

Temporal evolution of the distribution is shown in figure 3.8. The profiles result from the integration of the absorption images as shown in figure 3.7 along the x-direction. The data were taken at increasing loading times from 10 ms (top) to 40 ms (bottom). Profiles

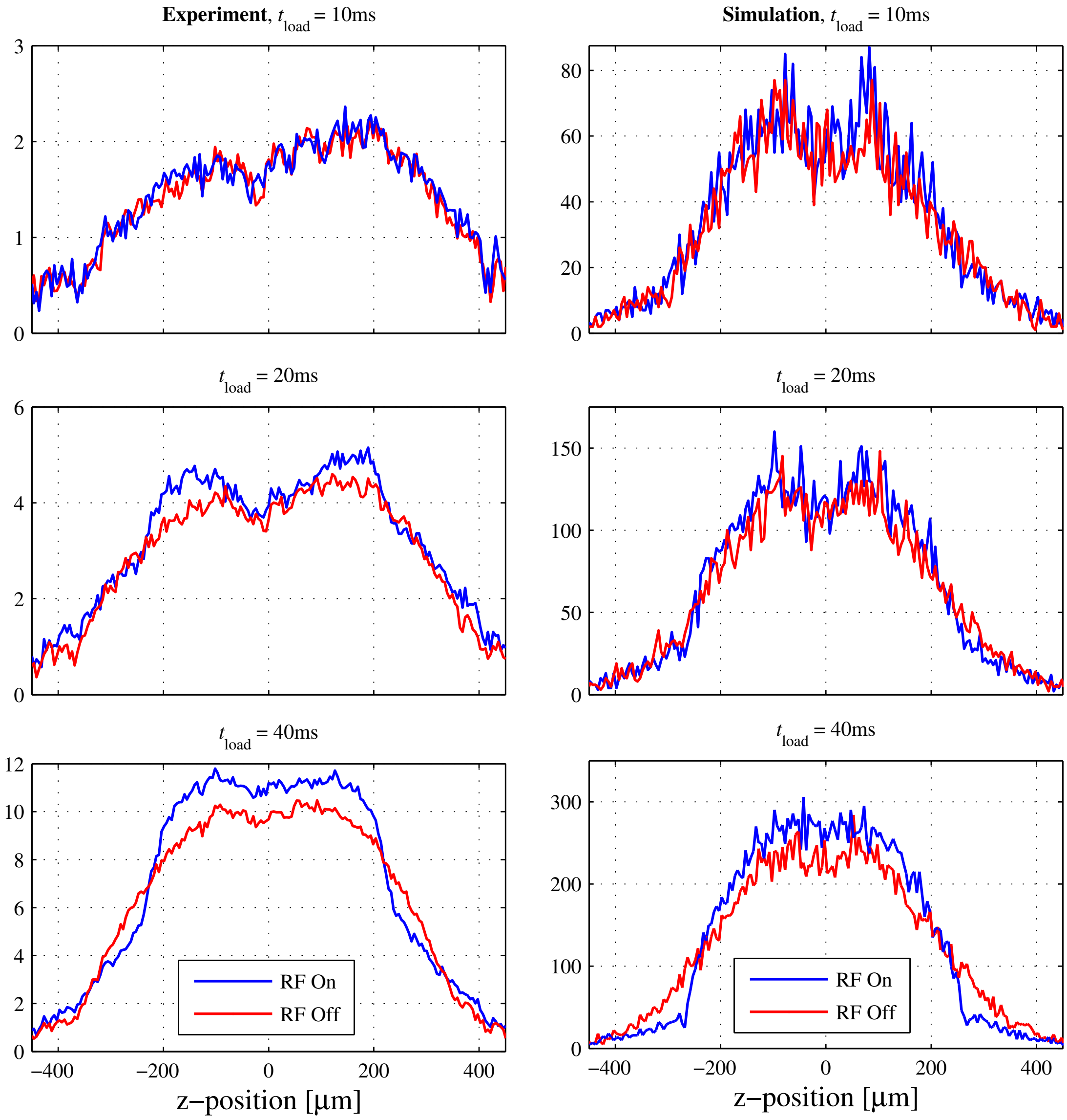

Figure 3.8: Profiles at different loading time show the evolution of the position and momentum distribution. The blue profiles originate from experiments (left column) or MD-simulation (right column) with a RF field oscillating at 30 MHz. No RF field was present in the case of red profiles. The high energetic wings of the red profiles are transferred into the centre after ≈40 ms of loading time. Note the changing y-axis scale, it takes the continuous increase of the number of atoms into account.

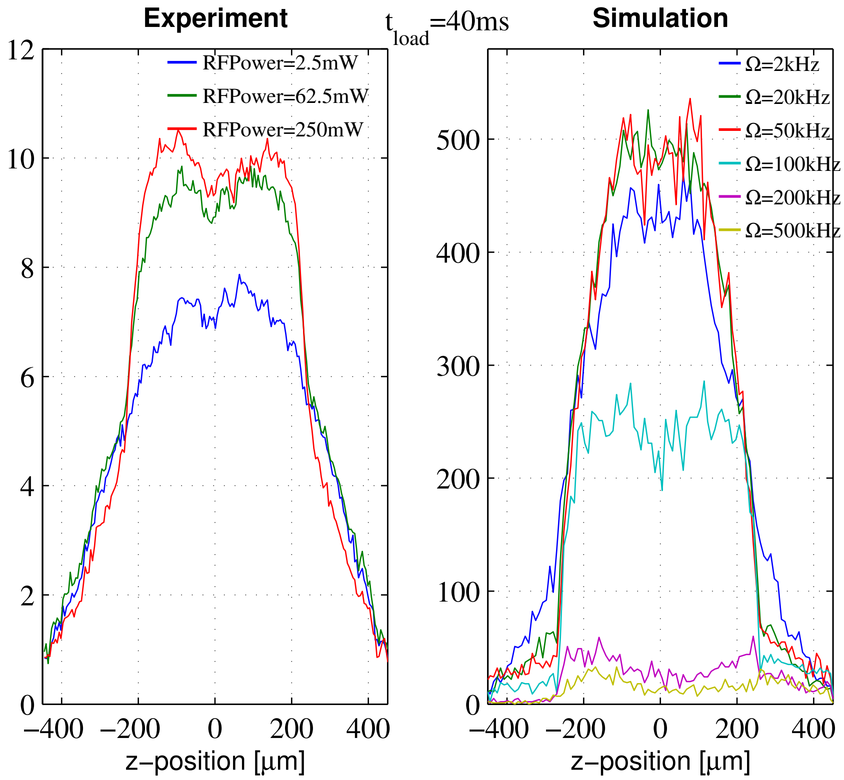

Figure 3.9: Experimental profiles are compared to MD-simulation at different Rabi frequencies. For the simulation, the change of the profile appears above a coupling strength of $\Omega = 5\,\mathrm{kHz}$. The drop of signal above the Rabi frequency $\Omega = 50\,\mathrm{MHz}$, can be explained by strong RF-transitions (see figure 3.10) before the actual optical pumping can dissipate the directed kinetic energy.

on the right hand side of figure 3.8 are the corresponding results of the simulations of the loading and simultaneous Sisyphus cooling. We observe the appearance of a cut-off in the distribution after a few tens of milliseconds, which is much longer than the oscillation time in axial direction of 3.4 ms. This suggests that most passages across the RF resonance result in no change of the magnetic sub-state. At given RF settings (frequency $f_{\mathrm{RF}} = 30\,\mathrm{MHz}$, power $\mathrm{P}_{\mathrm{out}} = 160\,\mathrm{mW}$) the total number of atoms during the collisionless time is not reduced by RF.

In figure 3.9 we present profiles taken at $t_{\mathrm{load}} = 40\,\mathrm{ms}$ for increasing RF power but constant frequency $f_{\mathrm{RF}} = 30\,\mathrm{MHz}$. From the comparison to the simulation we can estimate that the actual Rabi frequency Ω[7] is on the order of 20-50 kHz[8]. Additionally, the simulations give access to the number and strength of RF transitions occurring during

---

[7] Here and in the following we omit the 2π in front of all Rabi frequencies.

[8] This range is compatible with the expected oscillating magnetic field when taking the geometry of the antenna into account and assuming poor impedance matching.

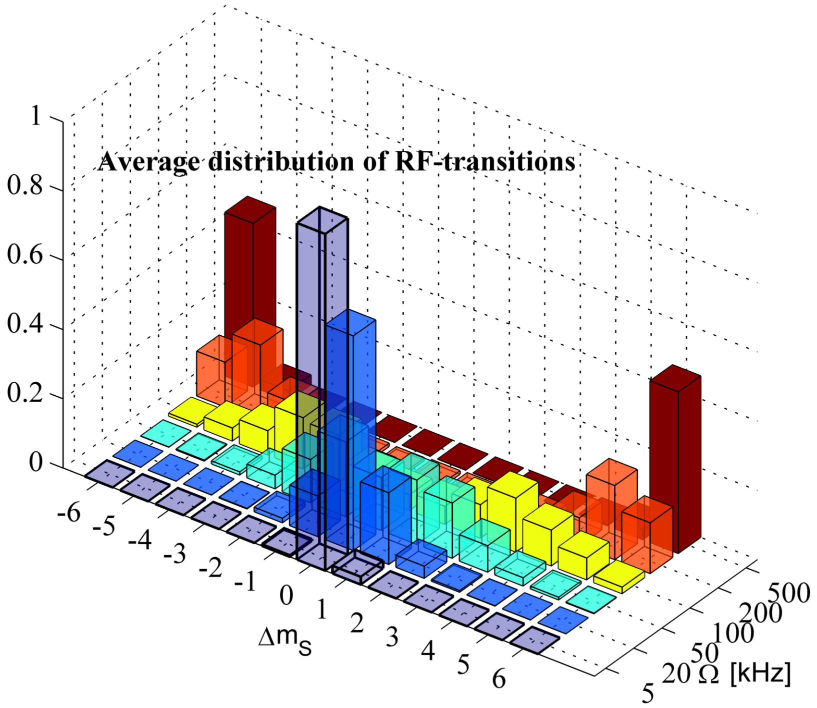

Figure 3.10: Passages across the RF-resonance are recorded and the change of the internal state is averaged over all passages within 10 ms. The histogram represents the statistics of the transition at different coupling strengths. We see that at $\Omega = 100\,\mathrm{kHz}$ the most frequent transitions are $\Delta m_S = \pm 3$, which means that a fraction of incoming atoms is transferred into the $m_S = 0$ state prior to optical pumping. As a consequence, those atoms retain sufficient directed kinetic energy to leave the trap in axial direction. This is also the reason for the drop of signal in figure 3.9.

the loading process. Figure 3.10 shows the normalized distribution of RF-transitions for different Rabi frequencies, averaged over 10 milliseconds. The majority of passages across the RF resonances at Rabi frequencies below 10 kHz does not lead to a transition to a different sub-state. In the cooling range between 10 kHz and 50 kHz, the projection of the spin changes by one or two quanta $m_S = \pm 1, 2$. In fact, it is the asymmetry toward the positive values that is responsible for the net cooling effect. At high RF power (not accessible in the experiment) corresponding to Rabi frequencies above 100 kHz, the loading mechanism is strongly disturbed by the large change of the sub-state, as one can also see from figure 3.9. Eventually the 'atomic diode'-idea breaks down because atoms are transferred adiabatically from $m_S = 3$ to $m_S = -3$ (for $\Omega \geq 500\,\mathrm{kHz}$) prior to being optically pumped and trapped.

From the presented data it becomes clear that a strong RF field cannot be used to remove axially hot atoms from the trap without disturbing the loading process. We therefore conclude that the cooling effect observed in the experiment is a consequence of multiple iterations of cycles consisting of RF transitions and subsequent optical pumping.

3.4.2 Steady state properties

In order to describe the steady state properties of the continuously loaded trap, it is convenient to relate the thermal energy $k_\mathrm{B}T$ of the sample to the depth of the optical dipole trap U_ODT by defining $\eta_\mathrm{ODT} = U_\mathrm{ODT}/k_\mathrm{B}T$, where k_B is the Boltzmann constant. η_ODT determines the speed and the efficiency of the evaporation during the loading [Falkenau et al., 2012]. Similarly, we introduce $\eta_\mathrm{RF} = U_\mathrm{RF}/k_\mathrm{B}T$ as the ratio of the thermal energy and the RF threshold energy U_RF for the dark state $m_\mathrm{S} = -3$. The energy splitting between the neighbouring magnetic sub-states is given by $\Delta E_\mathrm{RF} = g\mu_\mathrm{B}B(z) \approx 2\mu_\mathrm{B}B(z)$ and the frequency necessary to drive transitions is given by $f_\mathrm{RF} = \Delta E_\mathrm{RF}/h$. The magnetic potential energy of the $m_\mathrm{S} = -3$ atoms at the location of the RF resonance can be written as $U_\mathrm{RF} = 3h \times (f_\mathrm{RF0} - f_\mathrm{RF}) = 3h \times \Delta f_\mathrm{RF}$, where f_RF0 is the frequency at the centre of the trap. In units of temperature the frequency difference Δf_RF =1 MHz corresponds to $U_\mathrm{RF} = k_\mathrm{B} \times 144\,\mu\mathrm{K}$. In the following, we have $f_\mathrm{RF0} = 33.8\,\mathrm{MHz}$ [9] and $U_\mathrm{ODT} = k_\mathrm{B} \times 1.3\,\mathrm{mK}$ for a total ODT laser power $P_\mathrm{ODT} = 90\,\mathrm{W}$.

The steady state is reached when the number of atoms loaded into the trap is saturated and the radial and axial motional degrees of freedom are in equilibrium via collisional thermalization. The loading time necessary to reach the steady state varies as a function of flux between a few hundreds of milliseconds and twenty seconds.

In the steady state, several cooling processes run in parallel. *Direct* Sisyphus cooling as it is described for the collisionless regime continues to cool incoming, and axially hot atoms. In addition, elastic collisions mix the radial and axial degrees of freedom. On the one hand, this gives rise to radial evaporation since atoms can obtain sufficient energy to leave the ODT in radial direction. On the other hand, collisional production of axially hot atoms leads to additional *indirect* Sisyphus cooling contribution despite $\eta_\mathrm{RF} > 1$, as the high energy tail of the energy distribution is constantly refilled. This situation is comparable to (plain) evaporation in axial direction, however, in our case, atoms promoted to a state above the RF-threshold are not lost from the system. Furthermore, despite of the lower dimensionality of Sisyphus cooling, the speed of the indirect Sisyphus cooling can be comparable to radial evaporation when the RF-threshold is lower than the depth of the ODT.

We characterise the RF-induced cooling by performing loading experiments at different frequencies and powers. Figure 3.11 (a) shows the steady state temperature and the number of atoms in the loaded trap as a function of the applied radio frequency. Although one would expect that for frequencies smaller than 25 MHz ($\eta_\mathrm{RF} > \eta_\mathrm{ODT}$) evaporation in radial direction should strongly suppress Sisyphus cooling by removing hot atoms, one has to keep in mind that new atoms are being continuously added to the trap. As it is pointed out in [Falkenau et al., 2011] and as we have seen in the collision-

---

[9] This frequency results from a total magnetic field of 13 G, of which 12 G are produced by the barrier coils, while the remaining field can be attributed to an additional offset field.

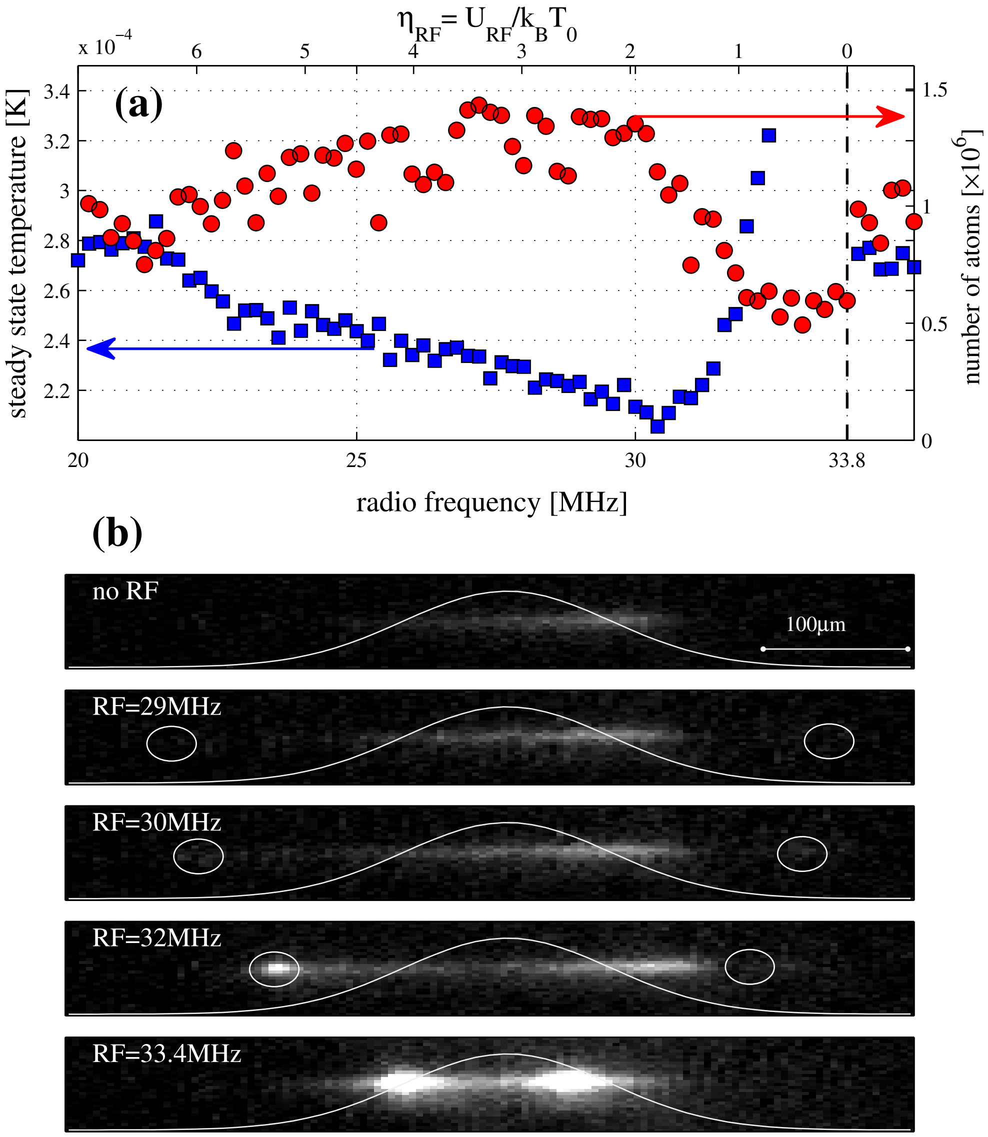

Figure 3.11: The temperature (squares, left axis) and the number of atoms (circles, right axis) of the sample in the steady state are plotted versus the applied radio frequency in (a). The RF threshold η_{RF} axis (top) is calculated with respect to initial temperature T_0 =280 μK. The vertical dashed line indicates the position of the trap bottom at the frequency of 33.8 MHz, above which the radio frequency field shows no effect. Pictures in (b) show the fluorescence of the atoms being loaded into and cooled in the hybrid trap in steady state. The optical pumping beam enters the depicted region from top and intersects the atomic trap in the centre. The position and the shape of the optical pumping beam are indicated by the Gaussian profile with a $1/e^2$ waist of 140 μm (white curve). When no RF is applied (top picture), the fluorescence corresponds to light scattered during the loading process only. The applied radio frequency manifests itself in increased fluorescence in the centre of the trap (see figure 3.12), as well as at the position where RF transitions are driven, highlighted by white circles.

less case above, those new atoms have much larger kinetic energy in axial than in radial direction before they thermalize and redistribute that energy in the cloud. Therefore the cooling effect already sets in at 22 MHz. The lowest temperature $T_{\text{min}} = 210\,\mu\text{K}$ is found around 30 MHz. We observe strong atom losses and an increase of temperature when the radio frequency approaches the trap centre. We can explain this behaviour by taking both the finite size of the optical pumping beam ($w_0 = 140\,\mu\text{m}$) and the axial spread of the atoms into account. The atomic position distribution at a temperature T has a $1/e^2$ width given by

$$R_z = \sqrt{\frac{4k_{\text{B}}T}{m_{\text{Cr}}\omega_z^2}} \tag{3.8}$$

The distance from the centre to the RF-resonance can be written as

$$R_{\text{RF}} = \sqrt{\frac{6h\Delta f_{\text{RF}}}{m_{\text{Cr}}\omega_z^2}} \tag{3.9}$$

For T_{min}, we obtain $R_z = 197\,\mu\text{m}$. The RF-resonance enters the atomic cloud at $\Delta f_{\text{RF}} = 2.8\,\text{MHz}$ when $R_z \approx R_{\text{RF}}$, which corresponds to $f_{\text{RF}} = 31\,\text{MHz}$. Figure 3.11 (b) shows a series of fluorescence pictures taken for increasing frequencies. The extent of the optical pumping beam is illustrated (to scale) by the white Gaussian profile. The onset of the losses and heating coincides with the frequency where the location of the RF-resonance (white circles) enters the spacial extent of the atomic sample and the pumping light beam.

We study the performance of the Sisyphus cooling in terms of gain in PSD as a function of the RF field power and present the results in figure 3.12. For each power setting we determine the phase-space density from an absorption picture. In addition to that we take a fluorescence picture giving access to the relative number of scattered photons. We consider only the light collected from the centre of the cloud as the fluorescence signal, as indicated by the region of summation in the inset of figure 3.12. The simultaneous increase of phase-space density with the fluorescence signal proves the occurrence of the Sisyphus cooling. We observe saturation of PSD at large RF powers. The dynamics of the cooling take place in the axial direction only, meaning that every time an atom interacts with the RF field it cannot avoid the optical pumping light on its oscillation back. For this reason, the fluorescence signal is directly linked to the probability of an atom to undergo a transition into another Zeeman sub-state. The strongest cooling effect is achieved when atoms are transferred into the $m_{\text{S}} = 0$ sub-state (see figure 3.1.) The saturation in the phase-space density and the fluorescence signal indicate that the Sisyphus cooling effect is balanced by transitions into the untrapped states and the loading mechanism itself gets disturbed.

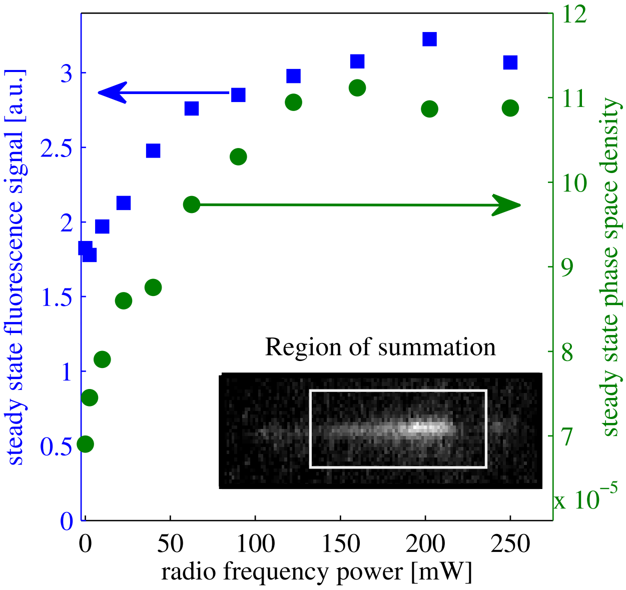

Figure 3.12: Saturation of the PSD and fluorescence for increasing RF power. The values of the fluorescence signal (squares, left y-axis) are obtained from a summation of the indicated region (see inset), while the phase-space density (circles, right y-axis) is extracted from separate absorption pictures of the atomic sample.

3.4.3 Density-limited regime

In the case of the continuous loading without additional Sisyphus cooling, the limiting factors on the one hand are elastic two-body collisions and the resulting evaporation of atoms during the loading [Falkenau et al., 2012], and, on the other hand, light-assisted losses coming from inelastic collisions with excited state atoms. Ultimately, the same is true for the Sisyphus-cooled loading mechanism. Nevertheless, RF-induced Sisyphus cooling leads to higher atom number, an increased density, and lower temperatures. To demonstrate and study this effect, we vary the steady state density by reducing the flux of the atomic beam. Figure 3.13 shows that without RF-induced cooling the steady state temperature of the fully loaded trap does not depend on the final density. Given the same atomic beam conditions and with optimized Sisyphus cooling, the temperature shows a linear dependence on the steady state density in the investigated regime. As a consequence, the PSD-gain of the RF-induced Sisyphus cooling is density dependent, which will be discussed in the next section.

There are at least three possible mechanisms for the density dependent temperature increase. First, the heating through reabsorption: as a matter of fact, the resonant optical density along the short axis of the cloud varies between 10 and 30. As a result, photons scattered in the optical pumping process are reabsorbed multiple times, leading to a heating depending on the density [Castin et al., 1998]. However, this cannot be the

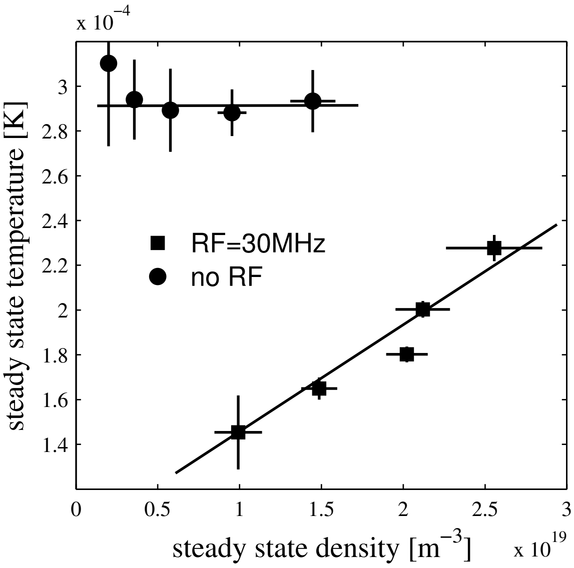

Figure 3.13: The flux of the atomic beam is varied, leading to different steady state densities of trapped atoms and corresponding temperatures. In the case of loading without RF (circles), the temperature is approximately constant. In the case of RF-assisted loading (squares) the temperature is significantly lower. However, it increases linearly with density (lines are guides to the eye). Error bars indicate the standard deviation of 5 independent measurements.

dominant reason, since scattered photons originating from the loading mechanism would also lead to significant heating, which is not observed in the experiment[10]. Second, excited state collisions in optical cooling of dense chromium samples have been observed and are discussed in more detail in chapter 4. One the one hand, we find that excited state collision are responsible for strong losses rather than heating. On the other hand, this loss (or heating) mechanism is not particular to the Sisyphus cooling and should equally increase with density due to the optical pumping in the loading process. Finally, as density increases, atoms being loaded into the trap are more and more likely to collide and redistribute their initially high axial kinetic energy in the sample *before* reaching the RF-resonance for the first time. This effect inhibits the *direct* Sisyphus cooling during the loading process (see section 3.4.2). In addition to that, collisional recapture reduces the cooling rate of the *indirect* Sisyphus cooling that relies on collisional production of high energy atoms for $k_{\mathrm{B}}T \ll U_{\mathrm{RF}}$. In the case where the collision rate exceeds the oscillation frequency, high energy atoms likely undergo further collisions during a single oscillation period and may fall below the RF-threshold again. For given experimental conditions, the collision rate rises to $\Gamma_{coll} \geq 1500\,\mathrm{s}^{-1} \approx \omega_z$, entering the so-called hydrodynamic regime in the axial direction.

---

[10] One can estimate from figure 3.12 that the amount of scattered light from loading and Sisyphus cooling are approximately the same.

3.5 Applications I: achieving collisional regime from hot and dilute atomic beam

According to the density-dependent steady state temperature discussed in the previous section, the PSD gain of the Sisyphus-cooling drops for increasing flux and resulting higher steady state density. Therefore, the achievable steady state PSD saturates regardless of the increasing flux in the density-limited regime. The potential of the presented continuous Sisyphus cooling therefore lies in the low-density regime, especially when the phase-space density of the atomic beam is so low that the continuous loading scheme consisting of a single Sisyphus step fails to reach collisional density.

In order to demonstrate the capacity of the Sisyphus cooling to enable evaporative cooling for unfavourable starting conditions, we performed a series of experiments with decreasing flux and phase-space density of the atomic beam. Hereby, we implement experimental conditions relevant for beams that cannot be cooled radially and suffer from strong reduction of flux when for example velocity filtering techniques are applied [Tsuji et al., 2010].

In figure 3.14, the continuous loading is depicted by the solid arrows from (a) to (b), connecting the various atomic beam conditions in (a) to the steady state phase-space density versus the number of atoms in the fully loaded trap (squares) in (b). The gain given by the (vertical) lines in (b) corresponds to the simultaneous continuous Sisyphus cooling (triangles). The gain in PSD reaches two orders of magnitude when the density limitations of the Sisyphus cooling as discussed above do not play a role. Here we would like to emphasise that even when the radial cooling of the atomic beam is not used [Aghajani-Talesh et al., 2010] and the flux is reduced by almost three orders of magnitude (lowest, left-most data point in figure 3.14 (a)) the total overall gain relative to the atomic beam amounts to over nine orders of magnitude. For this case, the steady state temperature of the RF-enhanced loading scheme being $T = 150\,\mu\mathrm{K}$ corresponds to $\eta_{\mathrm{RF}} \approx 3.6$ and implies a high elastic collision rate, so that only the hottest atoms participate in the RF-induced Sisyphus cooling. We have experimentally checked that the subsequent lowering of the ODT power led to efficient evaporative cooling of the fully loaded trap. The efficiency of the evaporative cooling is expressed by the parameter $\gamma_{\mathrm{eff}} = -\log(PSD_f/PSD_i)/\log(N_f/N_i)$, where the indices i and f denote the initial and final phase space density and number of atoms. In typical experiments $\gamma_{\mathrm{eff}} = 3 - 4$ can be achieved [Olson et al., 2013]. We measured $\gamma_{\mathrm{eff}} \geq 4$ at a PSD gain of more than one order of magnitude, and explain this efficiency by the large initial truncation parameter $\eta_{\mathrm{ODT}} > 9$ and the high rate of collisions. The ability to reach this regime from an almost arbitrary beam [11] constitutes a major result of this work.

---

[11] The only constraint for this scheme is that the longitudinal velocity of the beam has to match the height of the barrier. In the next section this constraint is further relaxed.

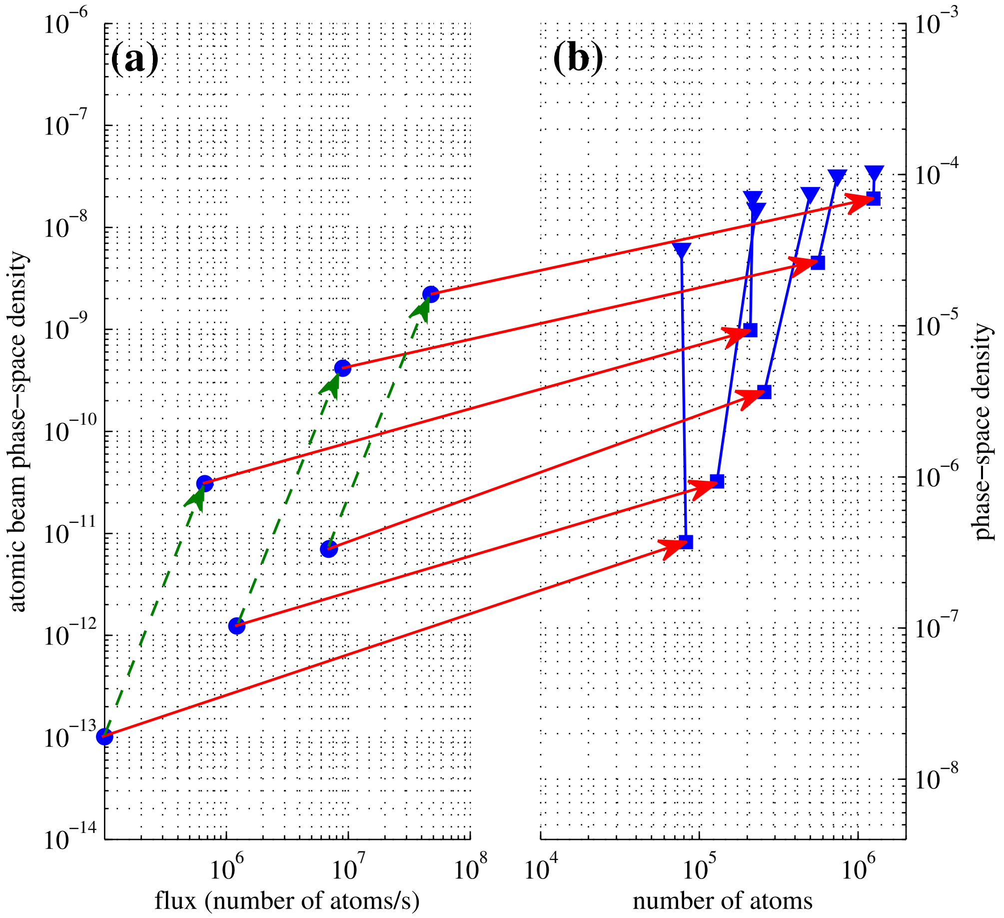

Figure 3.14: Continuous loading and cooling results (b) for different starting conditions (a) are summarized. The atomic beam in (a) is characterised by phase-space density and the flux. The data points denoted by circles correspond to different atomic beams arriving in the loading region. The flux of the atomic beam can be varied, as well as the radial temperature (see 2.1.5). The dashed arrows therefore indicate the phase-space density increase from continuous radial cooling of the atomic beam. The arrows from (a) to (b) represent the continuous loading process. The squares in (b) correspond to the phase-space density and the number of atoms in the continuously loaded trap in steady state without the RF field, whereas the triangles denote the steady state numbers with simultaneous RF-induced Sisyphus cooling.

3.6 Applications II: achieving collisional regime with a low barrier or weak ODT

In the original proposal [Aghajani-Talesh et al., 2009] and up to now the overall potential is chosen such that the incoming atoms in the low-field seeking $m_\mathrm{S} = 3$ Zeeman state have their turning points as close to the potential maximum as possible [Aghajani-Talesh et al., 2009, Falkenau et al., 2011]. This condition is vital in the limit where the initial kinetic energy E_Kin is much larger than the depth of the optical dipole trap U_ODT, since any excess energy can be redistributed in radial direction, leading to a fast removal (spilling) of atoms from the ODT. In particular, U_ODT needs to be taken into account by adding it to the initial kinetic energy in order to determine the necessary barrier height $U_\mathrm{B} = E_\mathrm{Kin} + U_\mathrm{ODT}$[12]. Furthermore, even when the potential height can be chosen according to the average initial velocity, the spread of the velocities translates into an initial axial temperature after the loading. For this reason, in order to retain the majority of the incoming atoms the depth of the ODT needs to be significantly larger than the total initial temperature. Evidently, these technical constraints strongly limit the applicability of the continuous loading scheme for other kinds of particle beams, since it is not possible to create neither arbitrarily high barrier potentials nor arbitrarily deep optical dipole traps.

In this section, on the one hand, we show that deviation from required barrier and ODT parameters drastically compromises the efficiency of the continuous loading. On the other hand, we demonstrate under such conditions that RF-induced Sisyphus cooling restores the efficiency of the loading process.

Low barrier potential

In the first set of experiments, we have reduced the magnetic barrier field by a factor of 2. We have measured the trap bottom to be at $f_\mathrm{RF0} = 16.5\,\mathrm{MHz}$. The loading dynamics are summarized and compared to regular loading (blue symbols) in figure 3.15. We first analyse the impact of the reduced barrier potential without additional Sisyphus cooling (red symbols). The most striking difference is observed in the steady state temperature: while axial (circles) and radial (asterisks) temperatures converge to $250\,\mu K$ in the case of regular loading, we observe no cross-dimensional thermalization in the modified barrier configuration. The lack of thermalization can be explained by two factors. First, the collision rate is strongly reduced due to the low density. Second, and more importantly, the probability of evaporation (loss of atoms) at such a high axial temperature is increased by a factor of 25 (see equation 3.14 in [Falkenau, 2011]). The steady state number of atoms is lowered by a factor of 3. Furthermore, when the

---

[12] In the limit, where the initial kinetic energy is less than one sixth of U_ODT, accumulation can take place by means of evaporation only [Roos et al., 2003].

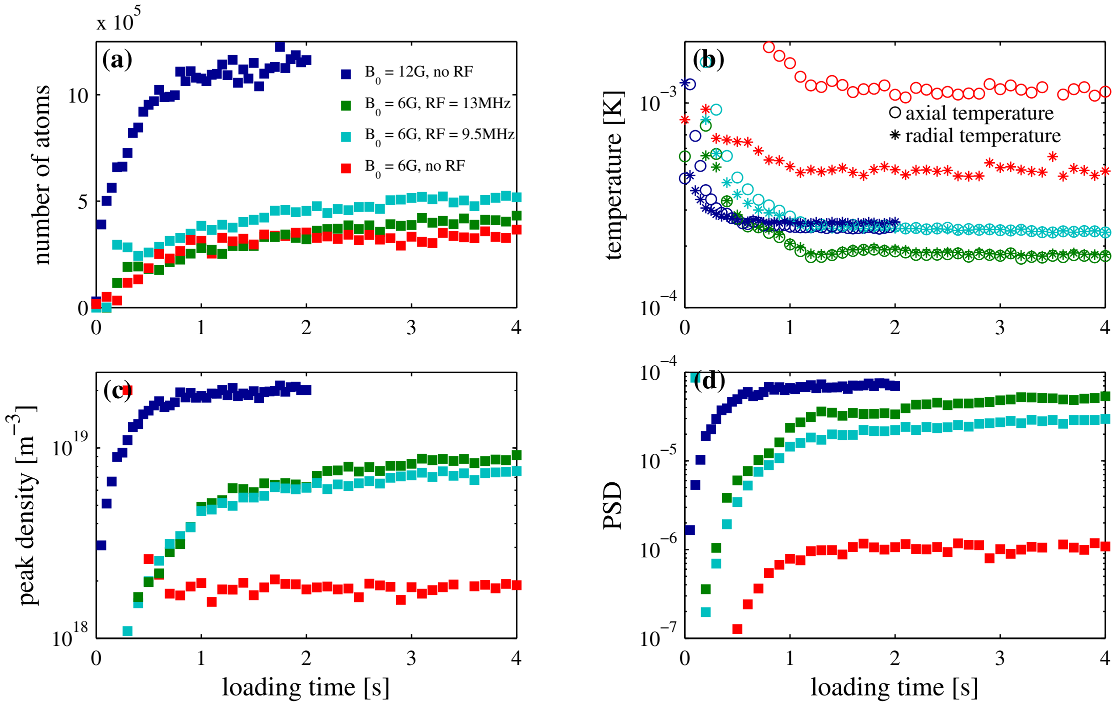

Figure 3.15: Dynamics of the continuous loading at a lowered barrier potential ($B_0 = 6\,G$) are compared to loading at regular barrier height ($B_0 = 12\,G$, blue symbols). For the low barrier data are shown without Sisyphus cooling (red), and with Sisyphus cooling at $f_{RF} = 9.5\,MHz$ (cyan) and $f_{RF} = 13\,MHz$ (green). In (b) radial (asterisks) and axial (circles) temperatures are presented separately. In absence of Sisyphus cooling, the continuous loading at $B_0 = 6\,G$ fails to reach high density necessary for thermalization of the axial and radial temperature, whereas when Sisyphus cooling is used a fast drop of axial temperature is observed.

continuous loading is interrupted, normally plain evaporation sets in. In the case of the lowered barrier configuration, plain evaporation is slow because of the low collision rate and inefficient because of the small η_{ODT}. We conclude therefore, that the lowering of the barrier potential basically turns the loading mechanism useless.

Let us now study the effect of RF-induced Sisyphus cooling on the loading performance. The general behaviour of the temperature as a function of the applied frequency is essentially the same as in figure 3.11. We present in figure 3.15 the loading curves for two different frequencies, at equal frequency generator output power of $P_{RF} = 50\,mW$. The data denoted by cyan symbols correspond to loading at $f_{RF} = 9.5\,MHz$, while green symbols represent data taken at $f_{RF} = 13\,MHz$. We observe that applying RF significantly reduces the steady state temperature, increases the density, and leads to a fast cross-dimensional thermalization. The temperature can be reduced below the regular loading scheme and reaches $T_{min} = 180\,\mu K$ at $f_{RF} = 13\,MHz$. The number of atoms is largest at $f_{RF} = 9.5\,MHz$. However, the improvement of the number of atoms provided by the Sisyphus cooling is rather moderate and amounts to a factor of 1.4 as shown in figure 3.15 (a). The number of atoms does not reach the level of the regular loading scheme. The time constant of the loading remains practically the same despite the additional Sisyphus cooling. This shows that Sisyphus cooling does not allow to capture atoms that have enough directed kinetic energy to leave the trap right away despite the dissipation by the optical pumping. As a consequence of a finite initial velocity spread, further reducing of the barrier potential will eventually result in no atoms being trapped with or without Sisyphus cooling.

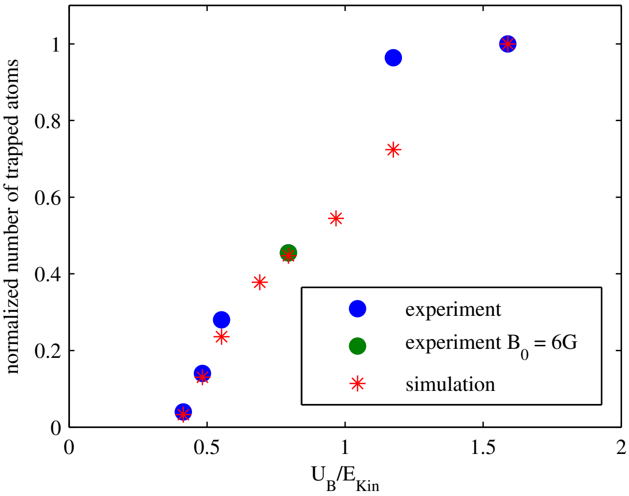

Figure 3.16: Steady state number of atoms (normalized to the results of regular loading) are shown as a function of magnetic barrier height over the initial kinetic energy of the guided atoms. Sisyphus cooling is used in all measurements. The data point depicted by the green circle corresponds to the the green curves in figure 3.15. Loading stops functioning for $\mathrm{U_B} \leq 1/2\mathrm{E_{Kin}}$. The results are well reproduced by the MD-simulation (red asterisks).

Nevertheless, when Sisyphus cooling is used to dissipate the excess energy left after the first slowing step, the purpose of the barrier is no longer to stop the atoms at the top of the potential, but to remove sufficient energy so that the atoms remain trapped in the combined potential for the high-field seeking state. Therefore, the condition for the magnetic barrier height $U_\mathrm{B} = E_{Kin} + U_\mathrm{ODT}$ (see above) changes to $U_\mathrm{B} \geq 1/2E_\mathrm{Kin}$. We demonstrate this effect by performing Sisyphus cooling assisted loading at various magnetic field barrier heights. Optical pumping detuning and intensity as well as Sisyphus cooling parameters are optimized for each barrier setting.

In figure 3.16 we show normalized steady state number of atoms plotted versus the magnetic barrier height $\mathrm{U_B}$ over the initial directed kinetic energy E_Kin. The rightmost data-point corresponds to regular loading conditions shown above in figure 3.15 (blue symbols) and serves as reference[13]. The green data-point corresponds to the green loading curves in figure 3.15. Sisyphus cooling permits the reducing of the magnetic barrier height at the expense of number of atoms, still maintaining high collision rate in the trap. The experimental results in figure 3.16 demonstrate that the magnetic potential height can be reduced to $U_{\mathrm{B}} \geq 1/2 E_{\mathrm{Kin}}$. This interpretation of the experimental data is confirmed by the results of MD-simulations with the same experimental parameters (asterisks).

Low optical dipole trap depth

In this section, we investigate the influence of the depth of the ODT on the loading process. Then, we discuss how the Sisyphus cooling at low ODT depth leads to a strong increase in phase space density. The reducing of the depth of the ODT has two major consequences for the loading process. First, the number of incoming atoms and their radial temperature is reduced. The reduction of the radial temperature originates from the compression and funnelling of the magnetically guided atoms by the ODT and is not related to the loading mechanism. Second, the evaporation threshold is reduced, which on its own would dramatically affect the efficiency of the continuous evaporation during the loading process.

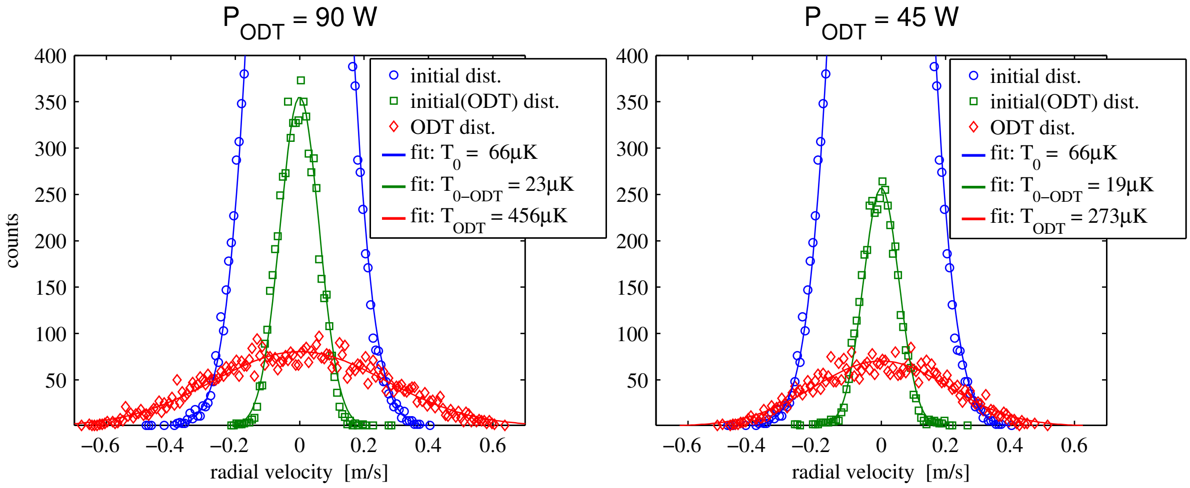

Figure 3.17: Simulation of the funnelling into the ODT. The compression of the guided atoms by the ODT is accompanied by heating. Initial velocity distribution of all atoms is denoted by the blue square. Only atoms that are found within the waist of the ODT laser beam are taken into account for the evaluation of the compression(red squares). The green squares denote the *initial* velocity distribution of atoms that make it into the ODT.

The efficiency of the transfer into the ODT has been studied in

---

[13] As explained above, the magnetic barrier is larger than the E_{Kin}, since the optical trap depth U_{ODT} has to be taken into account.

[Aghajani-Talesh et al., 2009]. We adapted the simulation parameters to the current experimental settings $T_{\text{Guide}} = 65\,\mu$K and $v_0 = 1\,$m/s. We performed simulations of trajectories of atoms being compressed by the optical dipole trap at $P_{\text{ODT}} = 90\,$W and $P_{\text{ODT}} = 45\,$W, the results are shown in figure 3.17. For $P_{\text{ODT}} = 90\,$W, we find that atoms which reach the longitudinal centre of the ODT within the waist of $w_0 = 30\,\mu$m, have a radial velocity distribution that resembles a thermal distribution at $456\,\mu$K. This value matches well the experimentally obtained radial kinetic energy of the sample after a short loading time ($t_{\text{load}} = 10\,$ms). From the simulation at $P_{\text{ODT}} = 45\,$W, we obtain a velocity distribution corresponding to a temperature $T_{45\,\text{W}} = 273\,\mu$K at the centre of the ODT. Now let us come back to the evaporation threshold mentioned above. The initial axial energy of the loaded atoms depends mainly on the spread of the longitudinal velocities of the atomic beam (see equation 3.1) and corresponds to a temperature of roughly $700\,\mu K$ which is above the radial trap $U_{\text{ODT}} = k_{\text{B}} \times 650\,\mu$K depth at $P_{\text{ODT}} = 45\,$W. Consequently, collisional redistribution of that energy leads to a frequent direct loss of atoms (spilling) and a very inefficient continuous evaporation (see section 2.1.4).

In figure 3.18, we compare the loading dynamics at different depths of the dipole trap. The initial radial temperature (asterisks) without RF shown in figure 3.18 (b) confirms the results obtained above in the simulation of compression by the ODT. We also observe that the initial axial temperature (circles) is basically the same for both ODT depth settings (without RF). The steady state number of atoms at lower ODT depth is strongly reduced, on the one hand because less atoms are funnelled into the ODT, on the other hand because of the inefficient evaporation. The efficiency of the evaporation is restored by adding Sisyphus cooling denoted by green data in figure 3.18. We varied the frequency of the RF field and found minimal temperature slightly below $100\,\mu K$ at $f_{\text{RF}} = 31.5\,$MHz. At low ODT depth, the heating and losses induced by the RF field as observed in section 3.4.2 set in at $f_{\text{RF}} = 32.5\,$MHz. The position of the RF-resonance R_{RF} (see equation 3.9) then reaches the wings of the atomic sample with a width of $R_z \approx 100\,\mu$m at $100\,\mu$K. This shows that the presence of the optical pumping light at the position of the RF-resonance does not necessarily disturb the cooling. We have checked that at lower ODT powers, as the steady state temperature decreases, the respective heating frequency is found closer to the trap centre. These findings indicate therefore that light-assisted collisions play an important role in limiting the Sisyphus cooling [Kuppens et al., 2000].

The evolution of the phase-space density during the loading process is shown in figure 3.18 (d). Despite the lower number of atoms, the PSD at low ODT depth exceeds the regular loading[14] when Sisyphus cooling is used. Steady state temperature of $50\,\mu$K

---

[14] As shown above, the PSD of regular loading with optimized Sisyphus cooling reaches values around 10^{-4}.

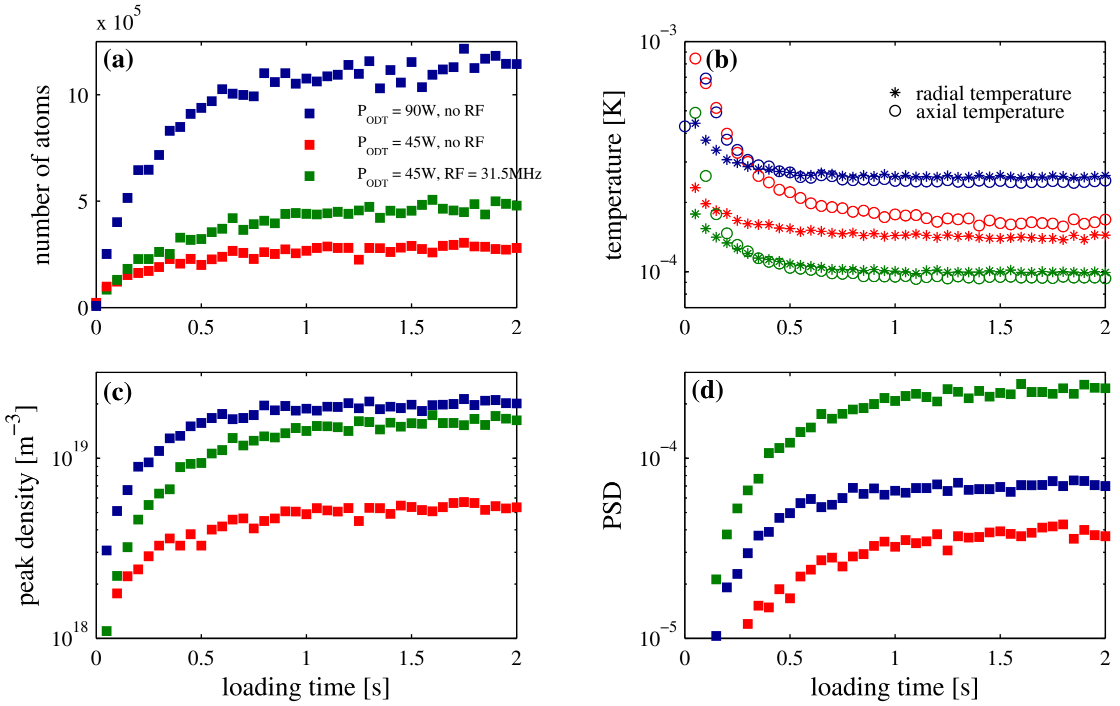

Figure 3.18: Dynamics of the continuous loading into a weak ODT ($P_{\mathrm{ODT}} = 45\,\mathrm{W}$) are compared to loading into a regular ODT (($P_{\mathrm{ODT}} = 90\,\mathrm{W}$), blue symbols). Moreover, we show data with (green) and without (red) Sisyphus cooling for the weak ODT. In (b) radial (asterisks) and axial (circles) temperatures are presented separately. The radial temperature at $t_{\mathrm{load}} \to 0$ in the reduced ODT power experiments is lower due to a weaker compression by the ODT. Combined with initially low radial temperature and efficient cooling of the axial temperature, Sisyphus cooling beats regular loading in terms of steady state PSD as shown in (d).

can be obtained by using an even weaker optical dipole trap combined with Sisyphus cooling. However, the PSD suffers from a very low atom number. In order to further explore this regime one could reduce the temperature of the guided beam, leading to a larger fraction of atoms funnelled into the ODT.

Summary

The results of the previous sections are summarized in figure 3.19. We perform continuous loading experiments at highest flux and lowest radial temperature of the magnetically guided atoms, the velocity of the atoms is $v_0 = 1\,\mathrm{m/s}$.

The continuous loading at a reduced height of the barrier potential ($B_0 = 6\,\mathrm{G}$) is denoted by the solid red arrow from (a) to (b) in figure 3.19. Compared to loading at optimized barrier height we observe a strong reduction of reached steady state number of atoms and phase-space density (squares). Under these conditions the Sisyphus cooling leads to a 50-fold improvement of the PSD and brings the sample into a strongly

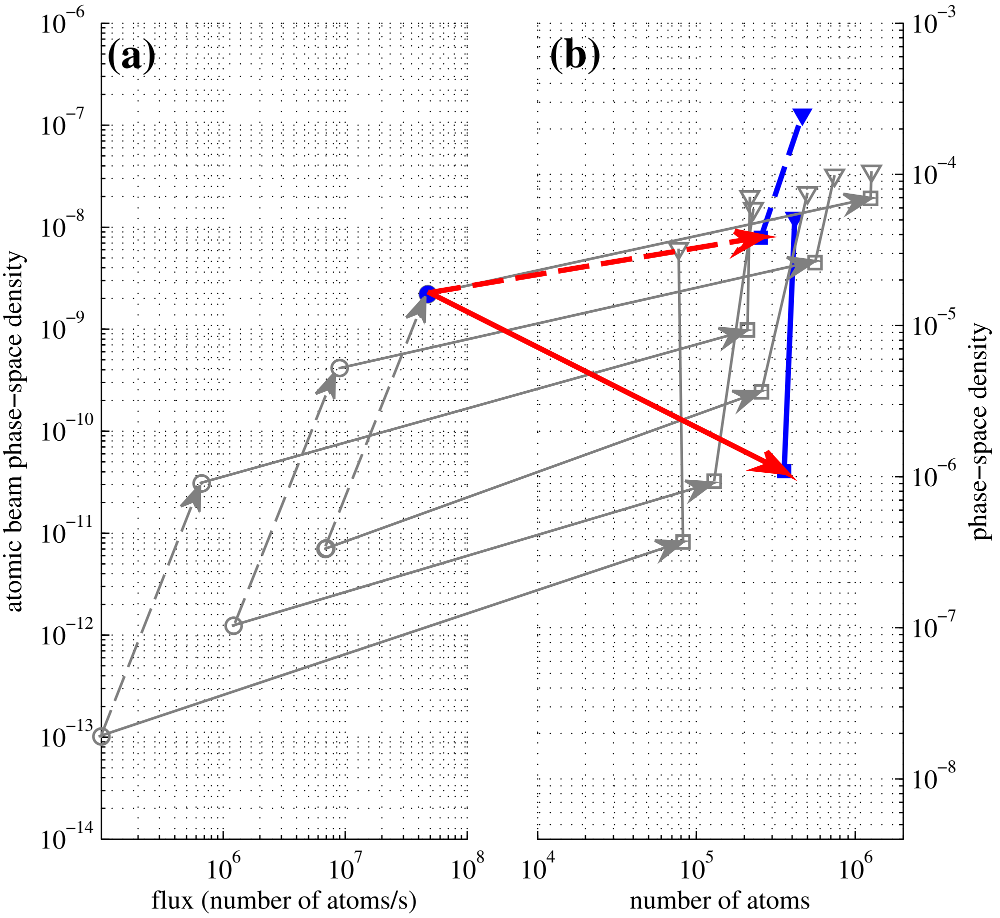

Figure 3.19: The performance of the loading scheme at compromised experimental parameters (solid arrow for $B_0 = 6\,\mathrm{G}$ and dashed arrow for $P_{\mathrm{ODT}} = 45\,\mathrm{W}$) is shown analogously to figure 3.14. The data from figure 3.14 is shown in gray for comparison.

collisional regime. The importance of this result lies at hand: the power dissipation of the magnetic field coils producing the barrier is the main limiting factor for the height of the barrier potential. We reduced the magnetic field by a factor 2, which in turn reduces the ohmic heating by a factor of 4.

Further, we have investigated the continuous loading into a weak optical dipole trap, depicted by dashed red arrow in figure 3.19. We have shown that, without additional Sisyphus cooling, the excess kinetic energy in axial direction of incoming atoms leads to an inefficient evaporation and slow cross-dimensional thermalization. The dashed blue line in figure 3.19 (b) denotes the gain produced by the Sisyphus cooling. The absolute phase-space density reaches the value of 2.5×10^{-4}, which surpasses the steady state PSD in a deep ODT with Sisyphus cooling (grey triangles).

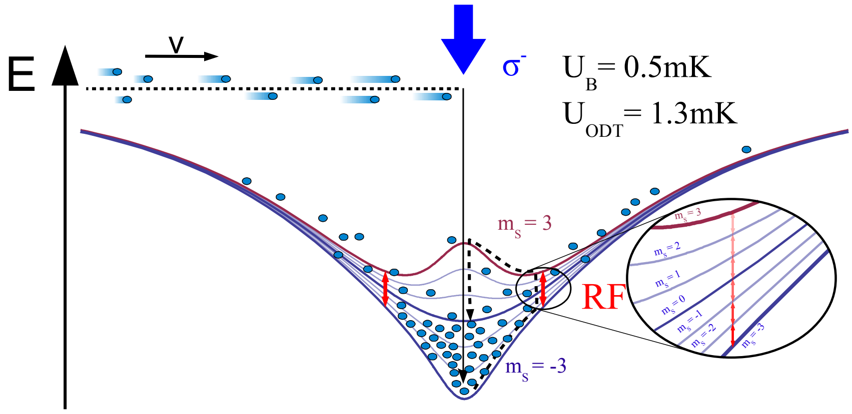

Figure 3.20: Alternative loading scheme for extra slow beams. Compared to scheme in figure 3.1, the velocity of the incoming atomic beam is reduced to v=0.4 m/s. At the same time, the barrier height is on the order of one half of the kinetic energy of the atomic beam. The depth of the ODT is kept constant. As indicated in the drawing, the atoms are first accelerated by the ODT before being slowed down by the repulsive barrier. Subsequently, optical pumping dissipates in total an energy corresponding to twice the barrier height. In this alternative scheme, the atom remains trapped radially *and axially* in the ODT and can repeat the optical pumping process when RF is applied.

3.7 Evaporationless regime

One of the limiting factor encountered in our analysis so far is the position of the RF-resonance relative to the sample and the optical pumping beam. At the same time, the steady state temperature is connected to the evaporation and Sisyphus cooling RF-threshold via η_{ODT} and $\eta_{\mathrm{RF}} = 3h \times \Delta f_{\mathrm{RF}}/k_{\mathrm{B}}T$ respectively. Therefore, the optimal frequency of the RF field corresponds to the minimal value of Δf_{RF} before the heating and losses set in.

The location of the RF-resonance can be pushed away from the centre of the trap by lowering the curvature of the magnetic field in axial direction, that is lowering the barrier potential. However, as we have seen in the discussion in section 3.6, the velocity of the guided beam sets the minimal barrier height.

In this section, we explore the regime where the initial directed kinetic energy is on the order of U_{ODT}. We reduced the velocity to $v = 0.4\,\mathrm{m/s}$, which is the lowest possible velocity in our setup. As a consequence, the flux dropped by more than two orders of magnitude and the radial cooling could not be used [Aghajani-Talesh et al., 2010]. This resulted in a slow but very dilute and radially hot atomic beam, as shown in figure 3.21 (a).

We lowered the magnetic field barrier to $B_0 = 1.5\,\mathrm{G}$ such that $U_{\mathrm{B}} \approx E_{\mathrm{Kin}}$. The trap bottom was found at $f_{\mathrm{RF0}} = 3.7\,\mathrm{MHz}$. With RF field at $f_{\mathrm{RF}} = 2.5\,\mathrm{MHz}$ we obtain $U_{\mathrm{RF}} = k_{\mathrm{B}} \times 173\,\mu\mathrm{K}$. Figure 3.20 illustrates this alternative scheme.

Similar to the discussion in the case of lowered barrier potential above, the loading mechanism in figure 3.20 still works by dissipating the potential energy via optical pumping in a Sisyphus step. The remaining kinetic energy can go up to $\mathrm{U_{ODT}}$ and has to be either removed by collisional thermalization and evaporation or by repeating the dissipative Sisyphus step when a RF field is applied. In contrast to figure 3.1, the atoms cannot be transferred into an axially untrapped state. The results of this loading scheme are presented in figure 3.21 (b). Similarly to figure 3.14, the steady state for RF-enhanced loading is denoted by the filled triangle, whereas loading without the RF field is denoted by the filled square. The steady state temperatures are $T_{\mathrm{RF}} = 50\,\mu\mathrm{K}$ and $T = 120\,\mu\mathrm{K}$ respectively. We obtain the highest steady state PSD of 4×10^{-4} with 10^5 atoms in the trap when RF-induced Sisyphus cooling is present. This PSD is significantly higher than in all previously described experiments in spite of the low initial PSD of the atomic beam!

We also observe that under such loading conditions the number of atoms is reduced by a factor of 2.5 when the RF field is applied. As outlined in section 2.1.4, the steady state number of atoms is governed by the loading rate, the background loss rate and the evaporation rate. Here, the loading rate as well as the background loss rate do not depend on the presence of the RF field. The rate of evaporation depends on the temperature and is strongly suppressed for $T_{\mathrm{RF}} = 50\,\mu\mathrm{K}$, corresponding to $\eta_{\mathrm{ODT}} \geq 26$. From these arguments we must assume that an additional loss process is involved when the continuous loading is accompanied by RF-induced Sisyphus cooling. The location of the RF-resonance is at $R_{\mathrm{RF}} = 375\,\mu\mathrm{m}$, which is outside of the optical pumping beam and also outside of the atomic sample ($R_z = 200\,\mu\mathrm{m}$ at $T = 50\,\mu\mathrm{K}$). Since the density does not exceed $10^{19}\,\mathrm{m}^{-3}$ we do not expect any losses associated with very high densities or light-assisted collisions. In case of multiple optical pumping events experienced by each atom the existence of metastable states may become important. The decay of the used $^7\mathrm{P}_3$ excited state has a branching ratio of $1 : 10^3$ to the metastable state $^5\mathrm{S}_2$ (see figure 2.1), which can be safely neglected in case of a small number of optical pumping processes. In the present loading scheme, however, the number of scattered photons per atom can become very large when large excess kinetic energy has to be dissipated by numerous Sisyphus steps. In order to investigate this assumption, additional repumping lasers are required.

3.8 Conclusion

In this chapter, we experimentally investigated the implementation of the continuous RF-induced Sisyphus cooling in various regimes and used computer simulation to provide insight into the observed effects on the level of single particles. We have shown that application of Sisyphus cooling significantly widens the range of initial beam conditions

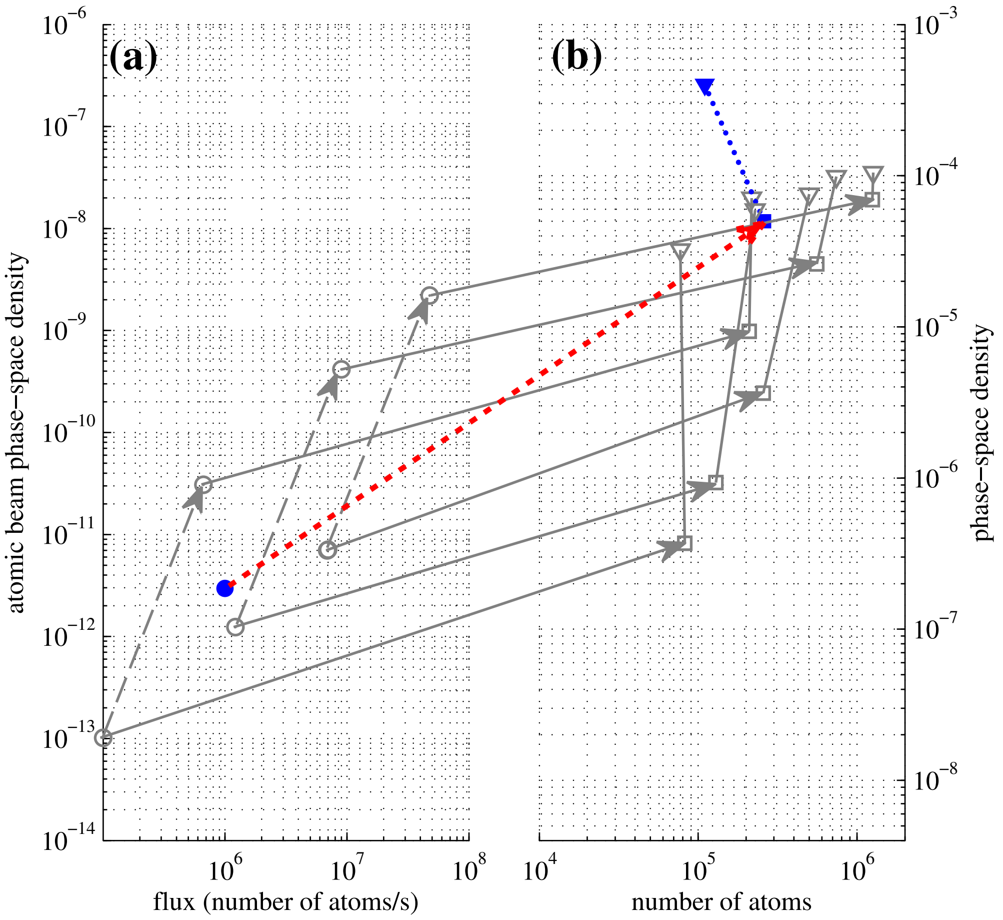

Figure 3.21: The performance of the alternative loading scheme is shown analogously to figure 3.14. The data from figure 3.14 is shown in gray for comparison. The data point with the highest PSD in (b) corresponds to an atomic sample with a steady state temperature of $T = 50\mu K$, at which evaporation is strongly suppressed.

that can be transferred via continuous loading into an optical dipole trap. In particular, atoms loaded with the assistance of Sisyphus cooling are efficiently brought into collisional regime, from which subsequent evaporative cooling can be used. We have demonstrated the generality of this approach by varying the transverse temperature and the flux of the initial beam, covering thereby more than five orders of magnitude in the initial PSD of the beam. Furthermore, the experimental constraints concerning the barrier height and the depth of the optical dipole trap can be relaxed when Sisyphus cooling is used to dissipate the excess in axial energy. Finally, we have also shown that with this techniques, the velocity can be reduced at the cost of flux and still a high PSD can be reached in the continuously loaded trap. In conclusion, the application of the Sisyphus cooling in continuous beam experiments facilitates the loading into a conservative trap by relaxing the requirements on the properties of the beam or by reducing the technical constraints. On the one hand, to our knowledge we have obtained the highest phase-space densities in *continuous* operation. On the other hand, this mechanism opens direct access to evaporative cooling for species that cannot be brought to high densities otherwise.

4 Efficient demagnetization cooling

In this chapter, we investigate demagnetization cooling of cold gases, a technique combining dipolar collisions and optical pumping [Kastler, 1950]. The cooling of the internal degree of freedom (spin) is realized by optical pumping, while dipolar relaxation provides the mechanism for re-thermalization of the internal and the external degrees of freedom. Starting from a polarized sample in the lowest magnetic sub-state (figure 4.1(a)), the kinetic energy of a pair of inelastically colliding atoms is reduced by ΔE for each particle that is promoted to the higher magnetic sub-state (figure 4.1(b)). The Zeeman-energy $\Delta E = g\mu_{\mathrm{B}}B$, where B is the applied magnetic field, corresponds to the energy splitting between neighbouring magnetic sub-states. Thus, the dynamics of the inelastic collisions are governed by the magnitude of the magnetic field, since only atoms with sufficient relative kinetic energies may undergo spin flips. Therefore, the energy splitting ΔE is typically on the order of the temperature of the sample. Optical pumping back to lowest sub-state cools the spin degree of freedom and dissipates the Zeeman energy (figure 4.1(c)). Furthermore, the optical pumping transition and the polarisation of the pumping light are chosen such that the atoms in the internal magnetic ground state do not couple to the light.

In a proof-of-principle experiment demagnetization cooling of a chromium gas has been demonstrated by our group [Fattori et al., 2006]. A moderate cooling effect has been observed in this experiment, however, the limiting effect remained unidentified. According to the theory [Hensler et al., 2005] temperature on the order of the recoil temperature (T_{R}) should be attainable. This raises the question whether quantum degeneracy can be reached using demagnetization cooling only.

In this chapter, we study demagnetization cooling of ^{52}Cr in a temperature range from $90\,\mu K$ to $6\,\mu K$. First main result it that a phase-space density of 0.03 was reached using demagnetization cooling – an important step towards quantum degeneracy by optical cooling only. Second finding of this study is that light-assisted losses present the dominant limiting mechanism in this regime [Volchkov et al., 2013]. We identify excited-state collisions as the source of the losses by their dependence on density of the sample, intensity and detuning of the optical pumping light.

In the following, we introduce a minimal set of equations used to calculate dipolar collision rates of chromium atoms, which are then compared to experimental results.

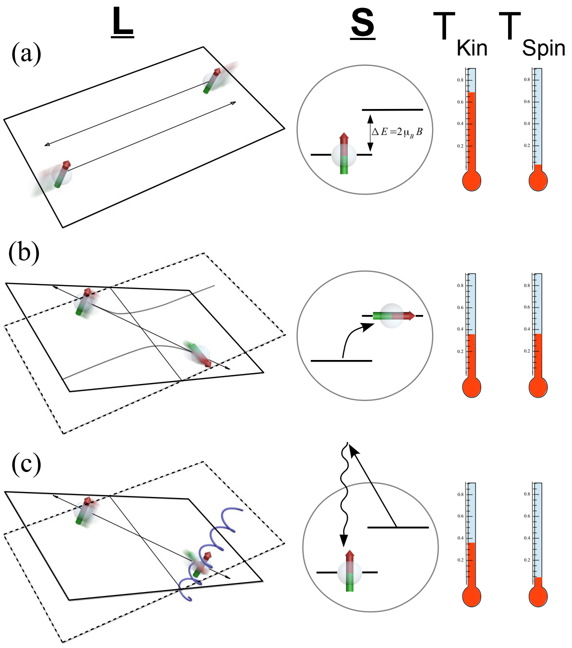

Figure 4.1: Illustration of the demagnetization cooling.Two atoms in spin-polarized state approach each other with finite angular momentum $\underline{\mathbf{L}}$ (a). During their (inelastic) collision the orbit is coupled to the spin $\underline{\mathbf{S}}$ via dipole-dipole interaction. The plane of the outgoing atoms in (b) is inclined with respect to the plane of the incoming atoms, which indicates the non-conservation of the orbital angular momentum. Kinetic energy is converted into Zeeman energy leading to thermalization of the motional and spin degrees of freedom, as shown in (b). Finally, optical pumping cools the spin degree of freedom and dissipates the energy by the scattered photon (c).

In addition, we present several experimental techniques that were used to gain better understanding of the specific properties of our system.

4.1 Theory of dipolar collisions

The original theoretical investigation of dipolar relaxations was motivated by the possibility of magnetic storage of hydrogen atoms [Kagan et al., 1981, Lagendijk et al., 1986]. In the case of magnetic trapping, atoms in the low-field seeking state may undergo exoergic collision, leading to heating and possibly losses. Thus, the knowledge of the dipolar relaxation cross-sections gives access to lifetimes of trapped samples. The calculation of dipolar relaxations was extended to helium [Shlyapnikov et al., 1994, Fedichev et al., 1996] using Born approximation. In [Hensler et al., 2003] the first Born approximation was specifically applied to dipolar relaxation of chromium atoms and found to be in reasonable agreement with experimental results. Similar theoretical work was done for polar molecules [Bohn et al., 2009]. The dipolar relaxation rates from [Hensler et al., 2003] were eventually used for theoretical description [Hensler et al., 2005] and experimental demonstration of demagnetization cooling [Fattori et al., 2006]. A more sophisticated model of dipolar relaxations [Pasquiou et al., 2010] showed that at higher magnetic fields the influence of short-ranged molecular potentials on the wave-functions leads to significantly different cross-sections. Furthermore, it allowed a precise determination of the scattering length a_6 of chromium.

In the present work, we will use the results obtained in [Hensler et al., 2003] to calculate the cross-section of dipolar relaxation, which are valid in the regime of low magnetic fields (below 1G).

4.1.1 Scattering cross sections

Starting from a pair of polarized atoms in the stretched state $m_{\mathrm{S}} = -3$, the anisotropic dipole-dipole interaction may flip the spin of either one or both colliding atoms by $\Delta m_{\mathrm{S}} = 1$. The long-range part of the interaction potential is given by [Hensler et al., 2003]

$$U_{dd} = \mu_0 (g\mu_{\mathrm{B}})^2 \frac{(\mathbf{S}_1 \cdot \mathbf{S}_2) - 3(\mathbf{S}_1 \cdot \vec{e}_r)(\mathbf{S}_2 \cdot \vec{e}_r)}{4\pi r^3} \tag{4.1}$$

where μ_0 is the magnetic permeability constant, g is the Landé-factor, $\mathbf{S}_{1,2}$ are the two spin matrices, and $\vec{e}_r = \vec{r}/r$ with $\vec{r}$ being the interatomic separation. As mentioned above, the total cross sections are estimated using first-order Born approximation by calculating the Fourier transform of the interaction $\tilde{U}_{dd}(\vec{k}_f - \vec{k}_i)$ for all possible initial and final wavevectors $\vec{k}_i$ and $\vec{k}_f$. $\left|\tilde{U}_{dd}(\vec{k}_f - \vec{k}_i)\right|^2$ is then averaged over all possible orientations of $\vec{k}_f$ and results in

$$\begin{aligned} \sigma_0 &= \frac{16\pi}{45} S^4 \left(\frac{\mu_0 (g\mu_{\mathrm{B}})^2 m}{4\pi\hbar}\right)^2 (1 + h(1)) & (4.2)\\ \sigma_1 &= \frac{8\pi}{15} S^3 \left(\frac{\mu_0 (g\mu_{\mathrm{B}})^2 m}{4\pi\hbar}\right)^2 (1 + h(k_f/k_i)) \frac{k_f}{k_i} & (4.3)\\ \sigma_2 &= \frac{8\pi}{15} S^2 \left(\frac{\mu_0 (g\mu_{\mathrm{B}})^2 m}{4\pi\hbar}\right)^2 (1 + h(k_f/k_i)) \frac{k_f}{k_i} & (4.4) \end{aligned}$$

Here the subscripts 0,1,2 refer to the number of spins that are flipped. Therefore σ_1 and σ_2 correspond to dipolar relaxation whereas σ_0 is the cross-section of the elastic dipole-dipole scattering. The function $h(x)$ is given by

$$h(x) = \pm \left(-\frac{1}{2} - \frac{3}{8} \frac{(1 - x^2)^2}{x(1 + x^2)} \log \left(\frac{(1 - x^2)^2}{(1 + x^2)^2} \right) \right) \tag{4.5}$$

where the sign ± depends on the symmetry of the particles, + corresponding to bosons and − to fermions. The factor k_f/k_i accounts for the different density of the final states and is given by $k_f/k_i = \sqrt{1 - \frac{mg\mu_{\mathrm{B}}B}{2\hbar^2 k_i^2}}$ for a single spin flip and $k_f/k_i = \sqrt{1 - \frac{mg\mu_{\mathrm{B}}B}{\hbar^2 k_i^2}}$ for a double spin flip transition at a magnetic offset field B. It is worth noting that σ_0 does not depend on the momentum of the colliding atoms. In particular, elastic dipole-dipole scattering does not vanish for identical fermions, demonstrating the contribution of higher partial waves. The practical implication of this is that polarized

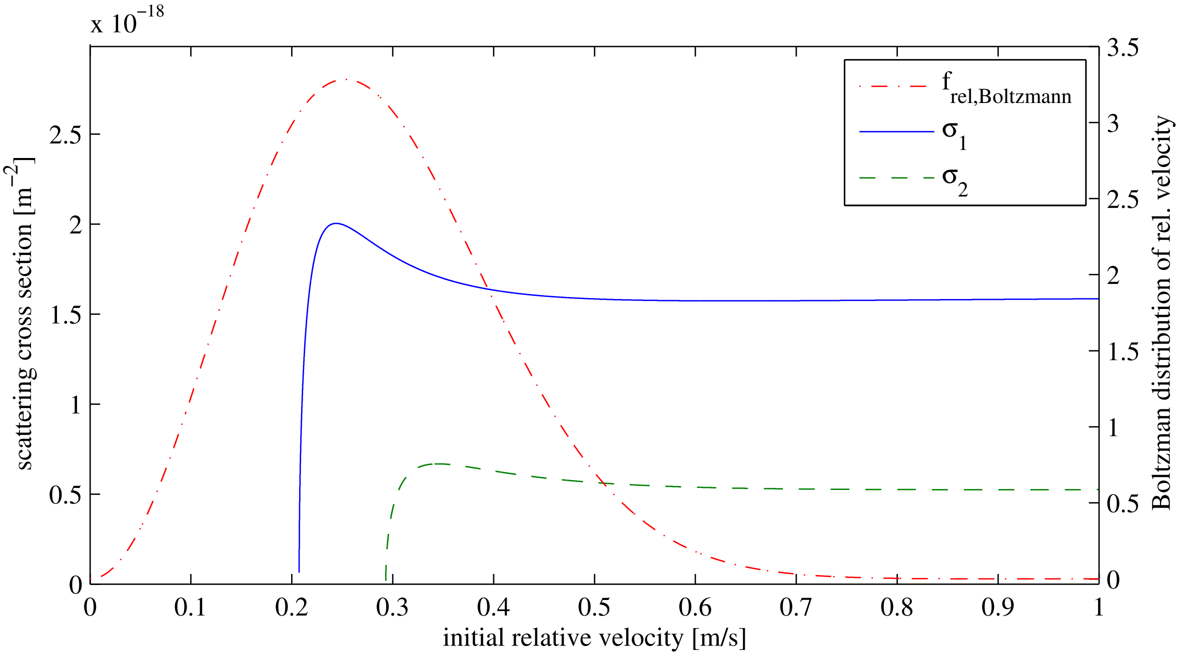

Figure 4.2: Scattering cross-sections are shown as a function of initial relative velocity at a magnetic field $B = 1\,\mathrm{G}$. Solid blue curve was calculated using equation 4.3, dashed green curve was calculated using equation 4.4. The red dashed-dotted curve shows the Boltzmann distribution of relative velocities at a temperature $T = 100\,\mu\mathrm{K}$.

samples of dipolar fermions can be directly cooled using evaporation cooling without any sympathetic coolant, as recently demonstrated in [Lu et al., 2012]. Energy conservation forbids spin flips when the relative kinetic energy is below the Zeeman splitting, therefore the cross section is zero below the corresponding velocity values, as illustrated in figure 4.2 for $B = 1\,\mathrm{G}$.

4.1.2 Dipolar relaxation rates

The total dipolar relaxation rate is given by $\Gamma_{\mathrm{dr}} = n(\sigma_1 + \sigma_2)v_{\mathrm{rel}}$, where v_{rel} is the initial relative velocity and n the density. For a thermal cloud, the Boltzmann distribution of relative velocities in a gas is used to obtain a thermal average of the relaxation rate

$$\Gamma_{\mathrm{dr,T}} = n \underbrace{\langle(\sigma_1 + \sigma_2)v_{\mathrm{rel}}\rangle_T}_{\beta_{\mathrm{dr}}} = n \int (\sigma_1 + \sigma_2)v \underbrace{\left(\sqrt{2/\pi}\left(\frac{m}{2k_{\mathrm{B}}T}\right)^{3/2} v^2 \exp\left(-\frac{mv^2}{4k_{\mathrm{B}}T}\right)\right)}_{\mathrm{f_{Boltzmann}}} dv \tag{4.6}$$

where we define β_{dr} as a density independent relaxation rate coefficient. The Boltzmann distribution for $T = 100\,\mu\mathrm{K}$ is shown exemplarily in figure 4.2. One can see that only a fraction of the velocity distribution contributes to the total rate of dipolar relaxation.

In the process of demagnetization cooling at a constant magnetic field the maximum of the velocity distribution moves to lower values, thereby further reducing the number of possible collision partners.

4.2 Detection of dipolar relaxation

It is important to be able to detect and control the dipolar relaxation in a simple experimental environment. Therefore, in the following section we will concentrate on the effect of depolarisation of the atomic sample without optical pumping. We will first focus on the thermalization of motional and internal degrees of freedom and the associated reduction of kinetic energy. In a second step, in order to have a more sensitive detection of dipolar relaxation we will take advantage of the strong heating effect when the spin energy of the sample is suddenly increased. Finally, we will use direct imaging of different magnetic sub-states after a spatial separation during a flight in a magnetic gradient field (known as Stern-Gerlach experiment).

4.2.1 Cooling as evidence for dipolar relaxations

A sample of chromium atoms polarized in the lowest magnetic sub-state will undergo a thermalization of kinetic and spin degrees of freedom via dipolar relaxation. The dynamics of such a thermalization were studied in [Fattori et al., 2006]. Here we are interested in the equilibrium temperature after a long time at different values of the Zeeman-splitting. According to [Hensler et al., 2005], the equilibrium temperature T_{eq} depends on the initial temperature T_0, the applied magnetic field B, and the total spin S (for $^{52}\mathrm{Cr}$ $S=3$) and can be calculated using

$$3k_{\mathrm{B}}T_0 = 3k_{\mathrm{B}}T_{\mathrm{eq}} + g\mu_{\mathrm{B}}B\frac{\sum_{i=0}^{2S} i \cdot \exp\left(-i\frac{g\mu_{\mathrm{B}}B}{k_{\mathrm{B}}T_{\mathrm{eq}}}\right)}{\sum_{i=0}^{2S} \exp\left(-i\frac{g\mu_{\mathrm{B}}B}{k_{\mathrm{B}}T_{\mathrm{eq}}}\right)} \tag{4.7}$$

Therefore, a reduction of the temperature should occur after a sufficiently long hold time.

Experimental sequence

We prepared the atomic sample by loading the hybrid trap as discussed in chapter 3. Throughout this chapter, unless otherwise stated, the optical dipole trap was operated at a power $P_{\mathrm{ODT}} = 90\,\mathrm{W}$. The loading resulted in a polarized cloud in a high magnetic field, in which demagnetization is negligible. Subsequently, the optical pumping was switched off and the magnetic field was ramped as illustrated in figure 4.3. During the decompression time (roughly 500 ms), a high homogeneous offset field was set while the

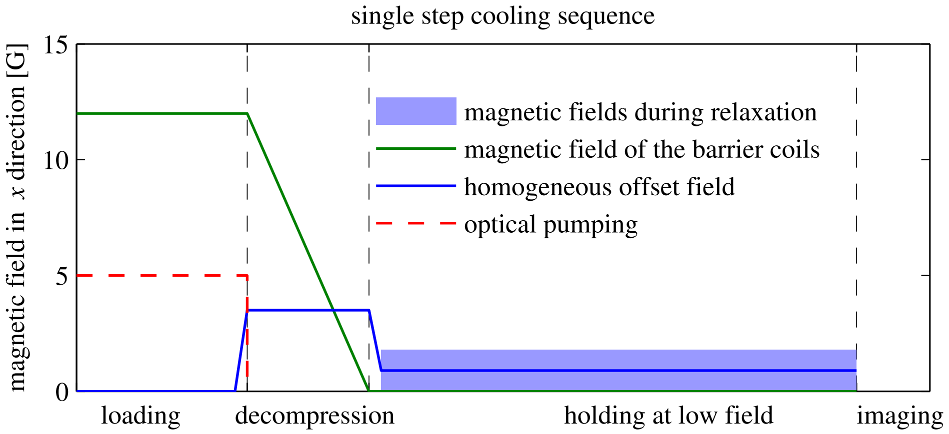

Figure 4.3: Experimental sequence illustrates different stages of a single measurement. Optical pumping denoted by the red dashed line was only used during the loading phase. After the decompression phase the atoms were held at a constant magnetic field. The shaded area indicates the range of investigated magnetic offset field settings.

current of the barrier coils was reduced. The atomic sample was decompressed in axial direction and adiabatically cooled to $T_0 \approx 100\,\mu$K, remaining polarized in the lowest sub-state. In the following step the offset magnetic field was set to a constant value $B_x = 0 - 1.8\,$G at which demagnetization and thermalization of kinetic and spin degrees of freedom took place. The hold time was typically several seconds in order to ensure the completion of all dynamics. At the end of each sequence, an absorption picture was taken, yielding the final temperature of the sample.

Results

The measured final temperature is plotted versus the applied magnetic offset field in figure 4.4. Additionally, we show the expected equilibrium temperature (red curve) according to equation 4.7 for the given offset field and assuming an initial temperature of $T_0 = 102\,\mu$K. We obtain a satisfactory agreement for a magnetic fields above 0.5 G. At magnetic fields close to zero the measured temperature is constant and does not follow the model. This deviation can be explained by the presence of weak uncompensated transversal fields, which results in a constant magnitude of the magnetic field when only one component is reduced to zero. The major shortcoming of this measurement is that the maximal cooling effect is on the order of magnitude of the shot-to-shot fluctuations. Furthermore, the maximal cooling effect is limited by the low heat capacity of the spin degree of freedom compared to the motional degree of freedom. A detailed comparison of a single step demagnetization cooling of a gas and a solid is given in the diploma thesis of Simone Götz [Götz, 2006].

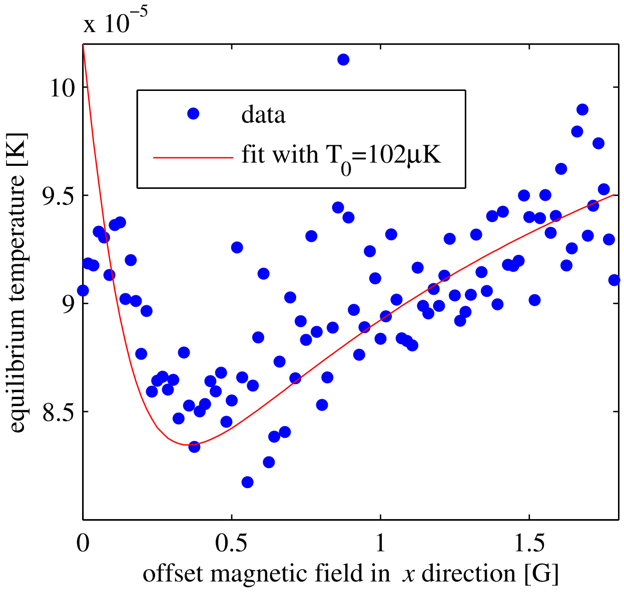

Figure 4.4: Final temperature at different magnetic offset fields is compared to the prediction of equation 4.7 (red curve). Deviation for zero magnetic field is most likely due to uncompensated transversal field components.

4.2.2 Heating as evidence for dipolar relaxations

What we want to probe is the degree of depolarisation at a given magnetic field, in an experiment as described above. The difficulty of the single step cooling is that the number of flipped atoms cannot be directly obtained from the change of the temperature due to the non-monotonic nature of equation 4.7, as shown in figure 4.4. In this following part we present a method that produces a signal that is directly related to the number of spin flips.

Experimental sequence

To this end, we take advantage of the exoergic dipolar relaxations in a depolarized sample at a high magnetic field. The experimental sequence shown in figure 4.5 is an extension of the previous cooling sequence. The demagnetization time at low offset fields is followed by a heating time at a high magnetic field. The temperature of the spin degree of freedom depends on the magnitude of the magnetic field. By suddenly ramping up the magnetic field we force atoms in higher spin sub-states to relax back to the lowest state, which can be seen as another thermalization process. As long as the Zeeman splitting is much larger than the temperature of the motional degree of freedom, the amount of heating is directly related to the number of atoms that were promoted to higher spin states during the preceding demagnetization phase.

Results

During the hold time at a high magnetic field the sample heats up depending on the number of previously occurred spin flips as we show in figure 4.6. Note that adiabatic

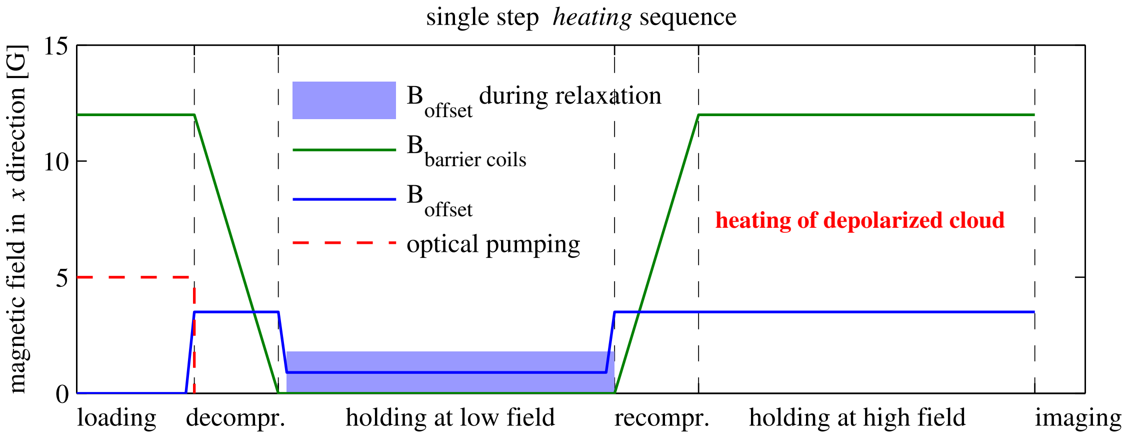

Figure 4.5: Experimental sequence of dipolar relaxation and cooling at low magnetic fields followed by heating at a high magnetic field. The hold duration at low and high field is 2 s. The resulting final temperatures as a function of magnetic field during the demagnetization phase are shown in figure 4.6.

Figure 4.6: Final temperature of the sample is plotted versus the magnetic offset field applied for demagnetization. The temperature increase is approximately proportional to the number of spin flips occurred when the low magnetic field was applied (see experimental sequence in figure 4.5). The red lines are guides to the eye.

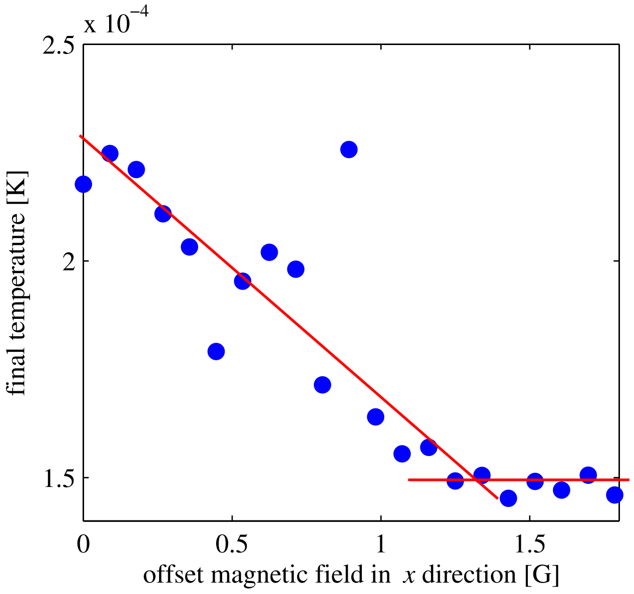

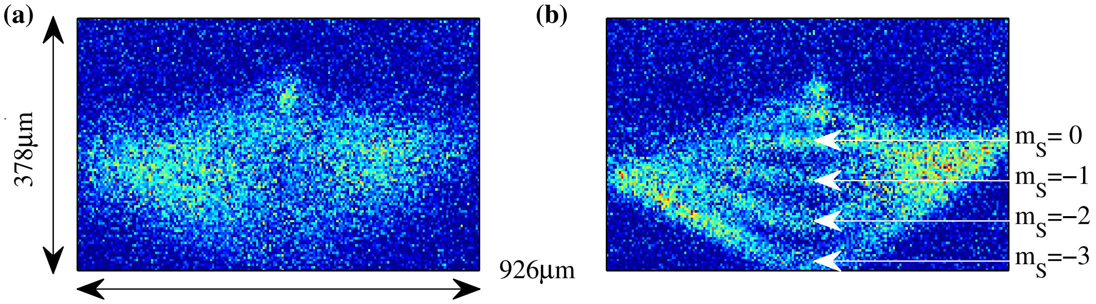

Figure 4.7: The absorption picture in (a) shows the result of a Stern-Gerlach experiment with a sample at temperature of $T \approx 20\,\mu$K. The atoms in the $m_{\mathrm{S}} = -3$ state experience the strongest acceleration to the bottom of the picture. However, the ballistic expansion smears out the separated components. In (b), delta-kick cooling was applied prior to the Stern-Gerlach sequence. As a consequence one can clearly distinguish between the magnetic components $m_{\mathrm{S}} = -3..0$. The distortion of the cloud, present in both pictures, originates from the inhomogeneous magnetic field gradient, created by the magnetic barrier coils.

heating during the 'recompression' leads to an overall higher temperature base line at $\approx 150\,\mu$K. An increase of the temperature by several tens of μK is clear evidence for dipolar relaxation at sufficiently low magnetic field. As expected, the heating effect increases for decreasing magnetic field. Above 1.5 G corresponding to $g\mu_{\mathrm{B}}B/k_{\mathrm{B}} \approx 2\mu_{\mathrm{B}}B/k_{\mathrm{B}} = 200\,\mu\mathrm{K} \approx 2 \times T_0$, we observe no heating[1]. This result suggests that the Zeeman splitting should not exceed the thermal energy of the cloud by more than a factor 2 in order to ensure efficient demagnetization.

4.2.3 Direct observation of population dynamics

In principle, the different magnetic sub-states can be spatially separated in a Stern-Gerlach type experiment and counted independently. To perform a Stern-Gerlach expansion a magnetic field gradient along the x direction is required. The atoms experience an acceleration depending on their magnetic sub-state and separate spatially during the time of flight. This technique was successfully used by many groups studying the dynamics of spinor Bose-Einstein condensates (e.g. [Schmaljohann et al., 2004]). Unfortunately, the adaptation of this method to our experiment poses some serious challenges. In order to spatially separate the m_{S} states during the time of flight the separation must be faster than the ballistic expansion of the cloud. In the case of a condensate the time-scale of the expansion correspond to temperatures on the order of 100 nK, therefore a weak magnetic field gradient is sufficient. In our case, we applied a magnetic field gradient on the order of 500 G/cm using the magnetic barrier coils in an anti-Helmholtz configuration. Due to the small dimension of the coils we obtained a very

---

[1] In the following we set $g \approx 2$.

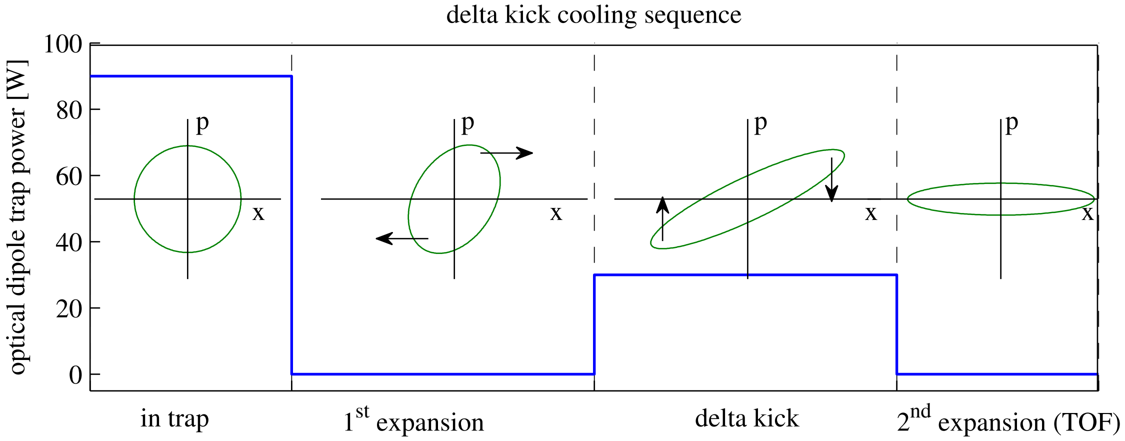

Figure 4.8: Delta-kick cooling is realized by allowing the atoms to expand for a short period of time ($\approx 30\,\mu$s) and then 'kicking' them with a short pulse of the ODT at a reduced power. The momentum p extracted from the atoms increases linearly (within the quadratic part of the ODT profile) with the distance x. The initial extent of the atomic cloud, the finite size of the ODT beam, as well as the band-width of the ODT laser set a limit to the lowest possible expansion velocity.

inhomogeneous gradient, leading to a strong distortion of the cloud, as shown in figure 4.7 (a). Furthermore, the different magnetic sub-states are smeared out because of the high temperature of the gas and the resulting fast ballistic expansion. As explained in the following, we use the so-called 'delta-kick cooling' [Ammann and Christensen, 1997] in order to reduce the smearing out, as can be seen in figure 4.7 (b). Still, the strong distortion of the cloud does not allow a quantitative analysis of the spin dynamics, we will therefore consider only the relative change of the populations.

Delta kick cooling

During the ballistic expansion of a thermal gas, the spatial distribution also reflects the momentum distribution of the atoms. Therefore, one can freeze the expansion by applying a position dependent kick that matches the momentum distribution [Ammann and Christensen, 1997]. Such a kick can be provided by a short pulse with a harmonic potential. In the ideal case, the expansion can be stopped completely. In the experiment, the initial size of the cloud and the finite range of the harmonic potential limit the efficiency of this cooling technique. The experimental sequence is illustrated in figure 4.8. The first expansion time of about $30\,\mu$s changes the phase-space distribution into something that resembles an ellipse with correlated momentum and position. The delta kick is applied by switching on of the optical dipole trap for a duration of another $30\,\mu$s. The optical dipole trap has a harmonic profile around its centre, therefore, the strength of the kick increases linearly with the radial distance from the centre of the trap

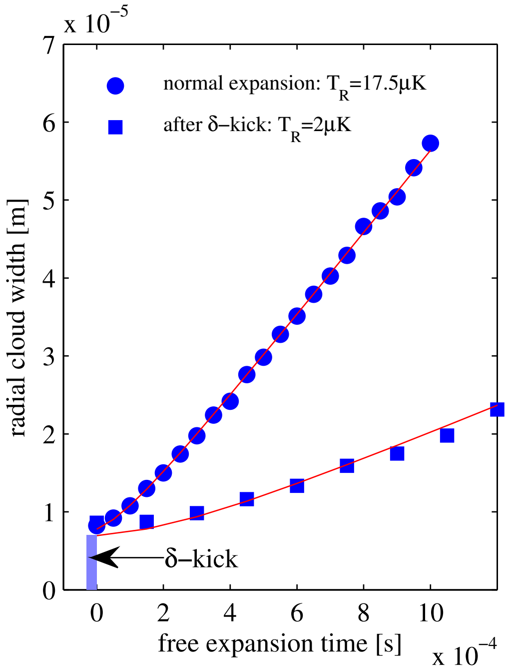

Figure 4.9: The cloud sizes as a function of expansion time are shown for normal expansion(circles) and expansion after a delta-kick (squares), denoted by the shaded area. The fit to the normal expansion reveals the (radial) temperature of the sample prior to the release from the trap. The delta-kicked samples appears as much colder.

and matches well the momentum distribution. After the delta kick the cloud expands at a significantly lower velocity and appears as a roughly 10 times colder sample, as shown in figure 4.9. The timings and the power of the optical dipole trap are adjusted experimentally and correspond to the lowest observed expansion velocity. Depending on the temperature of the sample the settings may need to be adapted. The first expansion time is a trade-off between long enough expansion in order to obtain a correlation between position and momentum, and sufficiently short expansion such that the cloud remains in the harmonic region of the dipole trap. We are also limited by the band-width of the ODT laser amplitude modulation, which is on the order of 10 kHz, so that the actual power does not strictly follow the set values shown in figure 4.8. Nevertheless, as demonstrated by the absorption images in figure 4.7, the reduction of the expansion velocity brings us into the regime where we can use the available magnetic field gradient to separate the magnetic sub-states.

Relaxation dynamics

In order to demonstrate the capability of investigating the dynamics of the spin states using Stern-Gerlach separation we prepared an atomic sample at a temperature $T_0 = 18\,\mu\mathrm{K}$ and with a peak density of $n_0 = 3.5 \times 10^{19}\,\mathrm{m}^{-3}$. The atoms were polarized using optical pumping light at a magnetic field of $B_{\mathrm{High}} = 0.36\,\mathrm{G}$ before the magnetic field was suddenly decreased to $B_{\mathrm{Low}} = 0.07\,\mathrm{G}$ and the optical pumping light switched off. The atoms were then held at the low field for a variable relaxation time and imaged after a delta-kick and a Stern-Gerlach separation. In figure 4.10 we show the evolution

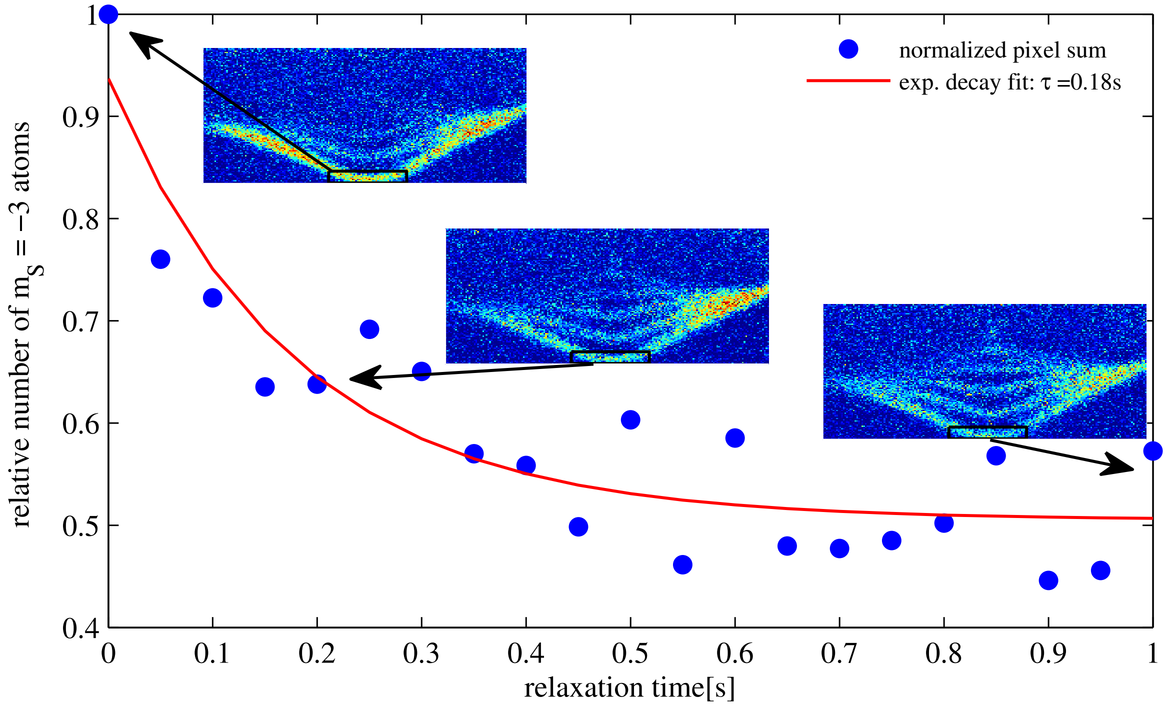

Figure 4.10: Depolarisation of the atomic sample at a low magnetic field is illustrated by the absorption pictures and the evolution of the atom numbers in the $m_S = -3$ state. A relative number of $m_S = -3$ atoms is obtained from the summation over the indicated region on the absorption pictures. We normalize the count to the number obtained at $t = 0\,\mathrm{s}$. Complementary curves are obtained for the other components, however, all with different time constants. The decay time-constant τ for the $m_S = -3$ state can be therefore regarded as global relaxation time. We have also verified that the sum over all sub-state remains constant during the whole time.

of a fraction of atoms in the lowest magnetic sub-state $m_\mathrm{S} = -3$ as a function of relaxation time. We counted the number of atoms in the black rectangle depicted on the in-set absorption pictures. The resulting numbers represent a fixed fraction of the total number of $m_\mathrm{S} = -3$ atoms. The depolarisation of the cloud is evident from the appearance of higher magnetic sub-states in the absorption pictures[2] (in-sets in figure 4.10) as well as from the decay of the $m_\mathrm{S} = -3$ state. The fact that the Zeeman splitting $2\mu_\mathrm{B}B/k_\mathrm{B} = 9.5\,\mu\mathrm{K}$ is almost 2 times smaller than the thermal energy implies that a large fraction of atoms may undergo dipolar relaxation collision. We fit an exponential curve to the data and obtain a characteristic decay time of $\tau = 0.18\,\mathrm{s}$. This time scale can be compare to the expected relaxation rate given by equation 4.6. For the specific experimental values we obtain $\beta_\mathrm{dr} = 3.0 \times 10^{-19}\,\mathrm{m^3s^{-1}}$ and $\Gamma \approx 10\,\mathrm{s}^{-1}$. This calculated value is in reasonable agreement with the experimental data. In other words, during the duration of the experiment atoms undergo several dipolar relaxations which is consistent with the observed depolarisation.

In this section we have shown that we can control the dipolar relaxation in a cold sample of chromium atoms. In the next section we will study the dipolar relaxation combined with continuous optical pumping, resulting in an efficient cooling technique.

4.3 Demagnetization cooling

In contrast to single step demagnetization cooling of solids, optical pumping of a demagnetized gas allows for fast polarisation of the spin and resumption of the demagnetization cooling. In fact, demagnetization via dipolar relaxation and optical pumping can take place simultaneously.

In the present section, we first discuss the technical issues involved in the implementation of optical pumping. The maintenance of a clean polarisation of the pumping light is of particular importance. In a second part we investigate the demagnetization cooling at different Zeeman splittings (i.e. magnetic offset fields), which will allow us to design an optimized cooling sequence consisting of several magnetic field jumps.

4.3.1 Optimizing optical pumping

The transition used for optical pumping ${}^7\mathrm{S}_3 \rightarrow {}^7\mathrm{P}_3$ is the same as the one used for the continuous loading of the hybrid trap (see chapter 2). Furthermore, all remarks concerning the importance of the dark-state given in the previous chapters hold here as well. In brief, we want the magnetic ground state $m_\mathrm{S} = -3$ to be the dark-state

---

[2] Admittedly, on the absorption picture taken at $t = 0\,\mathrm{s}$ components in states $m_\mathrm{S} > -3$ are present. This initial distribution is an effect of a projection by the strongly inhomogeneous gradient applied for the Stern-Gerlach separation and is not related to the dipolar relaxation.

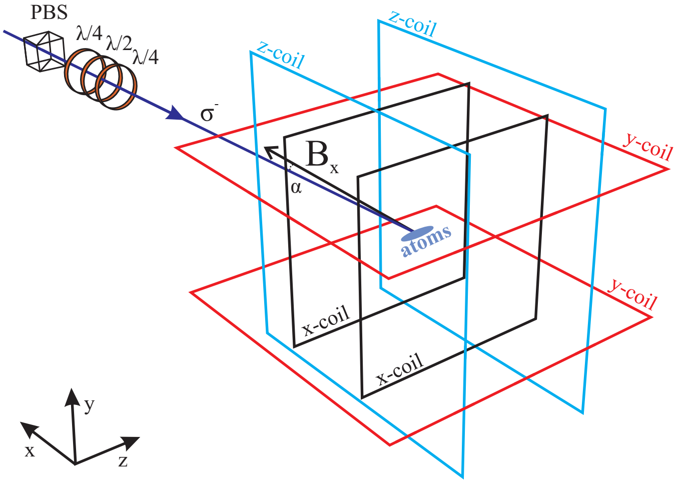

Figure 4.11: Experimental implementation of polarisation adjustment and magnetic field control for optical pumping. Optical pumping light passes a polarisation beam splitter cube (PBS) that transmits linearly polarized light with an extinction ratio better than 10.000 $>$ 1. Subsequently, a zeroth-order $\lambda/4$ retardation plate is used to create circular polarisation, combined with a series of $\lambda/4$-$\lambda/2$ plates used to compensate for any imperfections of the polarisation optics or possible birefringence of the vacuum chamber window. Three pairs of coils are used to generate the magnetic field offset field and to finely tune its orientation. The angle α illustrates the misalignment of the optical pumping beam and the magnetic field vector $\mathbf{B_x}$ generated by the x-coils.

with respect to the optical pumping light. Scattering of pumping photons is necessarily associated with a transfer of recoil to the atoms. Since we aim to reach temperatures on the order of the recoil temperature, scattering of light must be limited to 'useful' optical pumping only, that is scattering involving dissipation of the energy stored in the spin degree of freedom. Additionally, as we have already speculated in the context of the loading of the trap and will demonstrate below, light-assisted and density dependent losses play an important role in the optical pumping of very dense samples. Unlike in the process of continuous loading, now the magnetic field is created using large exterior coils. Therefore, on the scale of the trapped sample the field is homogeneous and its orientation is well defined.

Magnetic field alignment

The magnetic field axis needs to be oriented along the propagation direction of the optical pumping at all times in order to suppress π-transitions from the $m_S = -3$ state. The external coils used to generate the offset field are already mechanically aligned such that the field shows dominantly in the x-direction, as depicted in figure 4.11. We used the additional (z, y)-coils creating transverse fields in order to overlap the quan-

coil pairs	calibration in [G/A]	in [MHz/A]	background [G]
x	0.365	1.02	-0.033
y	0.266	0.744	0.288
z	0.233	0.653	-0.119

Table 4.1: Calibration of the magnetic field coils. Given values correspond to the magnetic field magnitude per ampere of applied current. Alternatively, the calibration is expressed as Larmor-frequency $2\mu_{\mathrm{B}}B/h$ per ampere.

tization axis provided by the offset field with the optical pumping light. To this end, first, we calibrated the magnetic field generated by all coils using RF-spectroscopy of atoms [Wenzel, 2012]. The calibration results summarized in table 4.1 also include the components of the background offset field. The background values correspond to a (quasi)-static magnetic field and can be compensated for by constant fields. These values are constant on the time-scale of a day, fluctuations of some percent have been observed over several days. Further, as a consequence of slight misalignment of the optical pumping beam with the axis of the x-coils, additional transverse fields that *depend on the magnitude* of the offset field are required. We determined the compensation fields for several values of the offset field using the atoms as a probe to the optical pumping light polarisation. We varied the currents generating the transverse components of the magnetic field on a grid in the neighbourhood of the background values. For each setting we shone optical pumping light at the atoms for 1 second and recorded afterwards the temperature of the sample. Examples of such temperature measurements are shown as insets in the figure 4.12. In the case of uncompensated transverse fields (in the outer regions of the temperature maps), the polarisation of the optical pumping can be decomposed such that an electric field component along the quantization axis appears, which drives π-transitions and heats up the sample. We use a two-dimensional Gaussian for fitting of the the data and extracting the position (i.e. currents) of the minimal heating (central region of the temperature map). Figure 4.12 shows the determined currents as a function of the offset field. Typically, we performed the compensation calibration once a day prior to any further measurements.

Optical pumping polarisation

In principle, a polarizing beam splitter and a $\lambda/4$ retardation plate are sufficient for creating of a circularly polarized light. In that case, the polarisation is limited by possible birefringence of the entry window (resulting from strain in the glass) or the imperfections of the polarisation optics. We used a combination of three retardation plates consisting of two $\lambda/4$ and one $\lambda/2$ as illustrated in figure 4.11 in order to further improve the quality of the circular polarisation. The additional degrees of freedom of the two supplementary

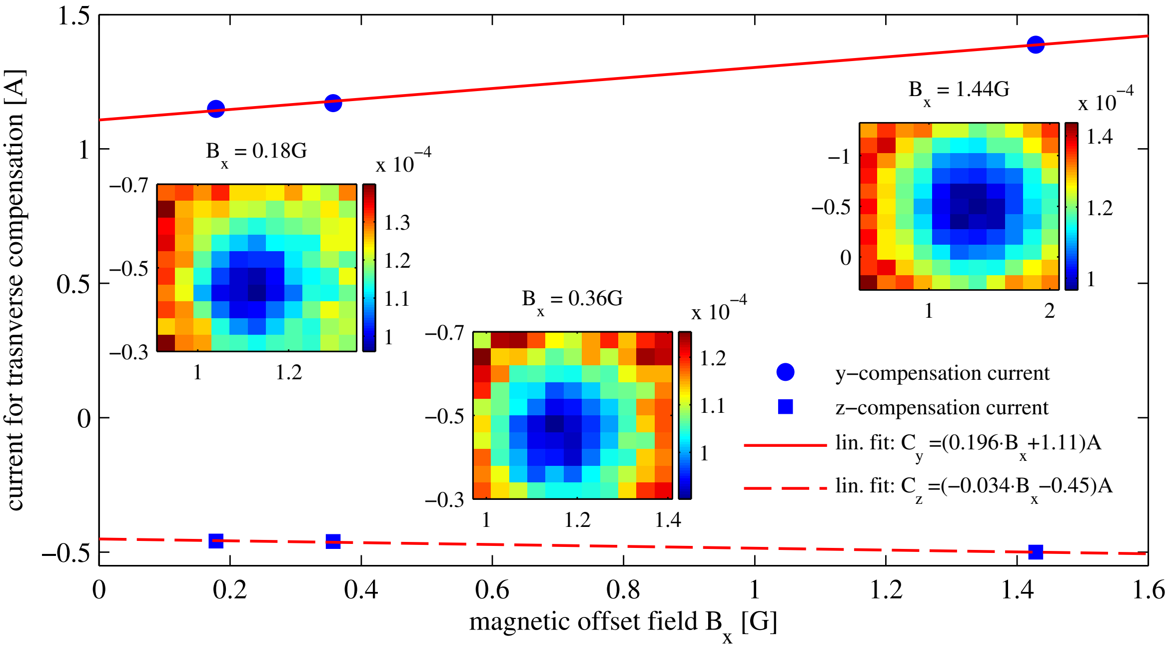

Figure 4.12: Example of transverse compensation calibration using atoms as a probe to the polarisation of optical pumping light. The insets show arrays of temperature at different compensation settings (x and y-axes corresponds to currents in z-coils and y-coils respectively). The minimum of a temperature map is determined using a 2D-Gaussian fit. Circles and squares denote the minima in the horizontal and vertical directions respectively. Currents for compensation at intermediate magnetic offset field values are calculated using linear fits denote by the solid and dashed lines.

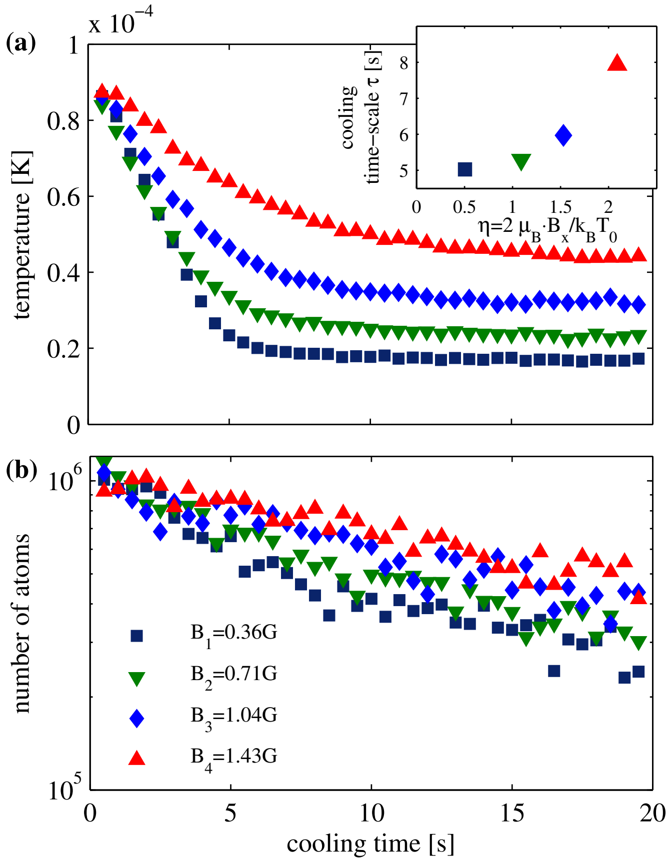

Figure 4.13: Single-step demagnetization cooling with continuous optical pumping at different magnetic offset fields. In (a) the time evolution of the temperature is denoted by different symbols for different magnetic offset fields, (b) shows the corresponding number of atoms. The cooling time-scale τ of each temperature curve, as defined in the text, is plotted versus the magnetic offset field in the inset.

retardation plates allow us to create arbitrary polarisations even when the retardation of each plate is not exactly $\lambda/4$ or $\lambda/2$. The specific optimal angles of the retardation plates are determined experimentally using the atoms as a probe (see above). We estimate the polarisation of the light to be better than $I_{\sigma^-}/I_{\sigma^+} \geq 4000$. Details concerning this technique can be found in the PhD thesis of Jahn Rührig [Rührig, 2014].

4.3.2 Multi-step demagnetization cooling

In the previous sections, we have demonstrated that we can induce dipolar relaxation in a dense sample of chromium atoms and control the relaxation rate using the magnitude of the magnetic field to vary the energy difference between neighbouring magnetic sub-states. We have also described how to turn the $m_S = -3$ state into a dark state regarding the optical pumping light by precisely controlling the orientation of the magnetic field, while using pumping light with circular polarisation only. Here, we present the performance of demagnetization cooling depending on the magnetic field.

The experiments were conducted similar to the single step dipolar relaxation sequence as described in section 4.2.1. This time, during the holding time at low field, the transverse fields were set according to the calibration and the optical pumping light was on. Figure 4.13 shows the evolution of the temperature and the number of atoms for different constant magnetic offset fields ranging from 0.36 G to 1.43 G. At time $t = 0\,\mathrm{s}$ the magnetic field was set to a specific value, and the optical pumping light was switched on. The resulting temperature curves are characterised by an initial cooling rate $\dot{T}_0$, and a final temperature T_{Fin} at which no further cooling is observed. Although in the thermodynamic sense the system has no state of equilibrium other than at $T = 0$, we can assume that for all practical purposes, when $\eta = 2\mu_{\mathrm{B}}B/k_{\mathrm{B}}T$ reaches values above 5 the cooling can be considered terminated. We define a time-scale for reaching the final temperature as $\tau = (T_0 - T_{\mathrm{Fin}})/\dot{T}_0$, where T_0 is the initial temperature. For experiments at a constant magnetic field the time τ can be used to quantify the efficiency of the cooling process. At very low magnetic offset fields the temperature curve starts with a flat slope, since the dissipated energy per dipolar relaxation collision is very small. Therefore the *initial* cooling rate $\dot{T}_0$ tends to zero. Together with a theoretically very low final temperature (neglecting losses and external heating), the resulting τ assumes large values. For intermediate magnetic field values such that the Zeeman energy splitting is lower but on the order of the initial temperature of the sample, we expect a minimum for τ since each dipolar relaxation event leads to a dissipation of a significant fraction of the kinetic energy. When the Zeeman splitting exceeds the initial temperature by more than a factor of two, the Boltzmann distribution begins to suppress dipolar relaxation as we have seen in section 4.2. This leads to a slow initial cooling and a large τ. The inset in figure 4.13 (a) shows the values of τ for the corresponding temperature curves. We determined the initial cooling rate from a linear fit of the first 4 seconds of the temperature curve, the final temperature was calculated by taking an average of the last 4 temperature data-points.

The evolution of the number of atoms during the hold time is shown in figure 4.13 (b). One can see that the final number of atoms does depend on the applied magnetic field. So far, the demagnetization cooling was considered as lossless. Here, we encounter losses which are associated with this cooling technique which were not discussed in earlier work [Fattori et al., 2006]. We will study the losses in more detail below. In general, it means that the number of atoms needs to be taken into account when efficiency of the demagnetization cooling is discussed.

Since the phase-space density (PSD) is the ultimate figure of merit, we optimized the cooling sequence by maximizing the gain in the phase-space density versus the loss of atoms, expressed by $\gamma_{\mathrm{eff}} = -\log(PSD_f/PSD_i)/\log(N_f/N_i)$ as already introduced in section 3.5. Specifically, we divided the hold time in intervals of several seconds. We determined experimentally the highest γ_{eff} as a function of the applied magnetic field

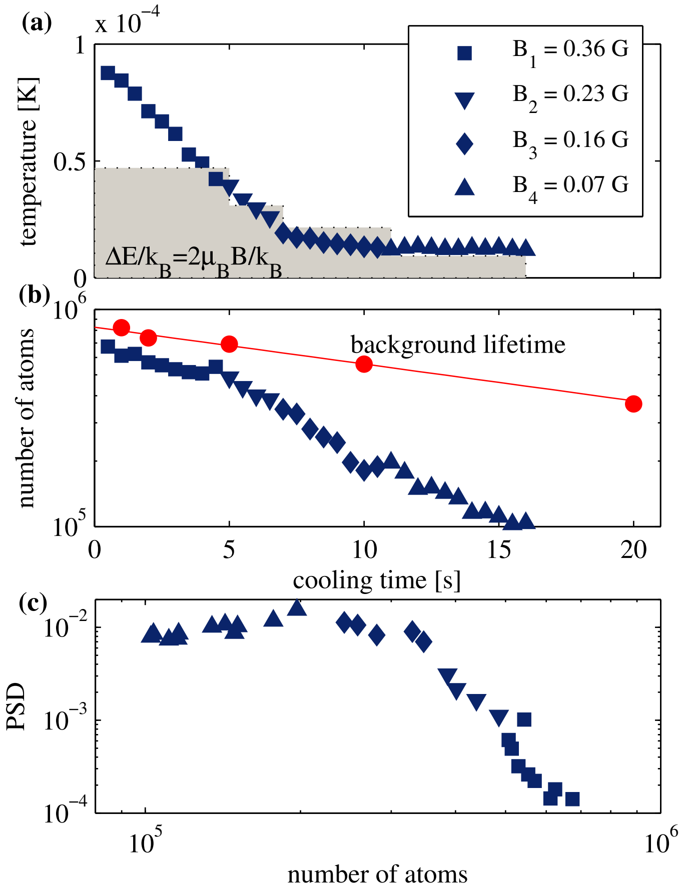

Figure 4.14: The time evolution of the temperature is shown in (a). The different symbols indicate the lowering of the magnetic field to match the decreasing temperature. In graph (b), the data points denoted by circles represent the decay of the number of atoms in the absence of cooling. The corresponding $1/e$-lifetime is $\tau = 27\,\mathrm{s}$. (c) The phase space density (PSD) plotted versus the number of atoms allows determining the efficiency of the cooling from the slope of the resulting curve.

for each time interval, resulting in a stepwise reduction of the offset field [3].

Figure 4.14(a) shows the temperature as a function of time for an optimized cooling sequence, in which the magnetic field was held constant during the time intervals 0-5s, 5-7s, 7-11s and 11-16s at values of $\mathrm{B}_1 = 0.36\,\mathrm{G}$, $\mathrm{B}_2 = 0.23\,\mathrm{G}$, $\mathrm{B}_3 = 0.16\,\mathrm{G}$ and $\mathrm{B}_4 = 0.07\,\mathrm{G}$ respectively. We observe a decrease in temperature from $T_0 = 90\,\mu\mathrm{K}$ to $T = 15\,\mu\mathrm{K}$ in the first 10 seconds and a further decrease to $T = 11\,\mu\mathrm{K}$ within the following 5 seconds. We achieve cooling rates more than one order of magnitude higher than observed in [Fattori et al., 2006]. We explain this improvement with the stronger confinement of our ODT and therefore the higher rate of dipolar relaxation collisions. The evolution of the number of atoms with and without cooling is presented in figure 4.14(b). While the lifetime of the atoms in the absence of light is only limited by the background pressure, the demagnetization cooling is accompanied by additional losses of atoms. We

---

[3] It would also be possible to linearly ramp the magnetic field as was done in [Fattori et al., 2006]. In our experiment, we have observed strong heating effects at specific magnetic fields. The origin of such resonances is not quite understood, although it appears that stray RF-fields were present, driving transitions to higher magnetic sub-states. Linear magnetic field ramps would necessarily cross the mentioned resonances, compromising the efficiency of the cooling sequence.

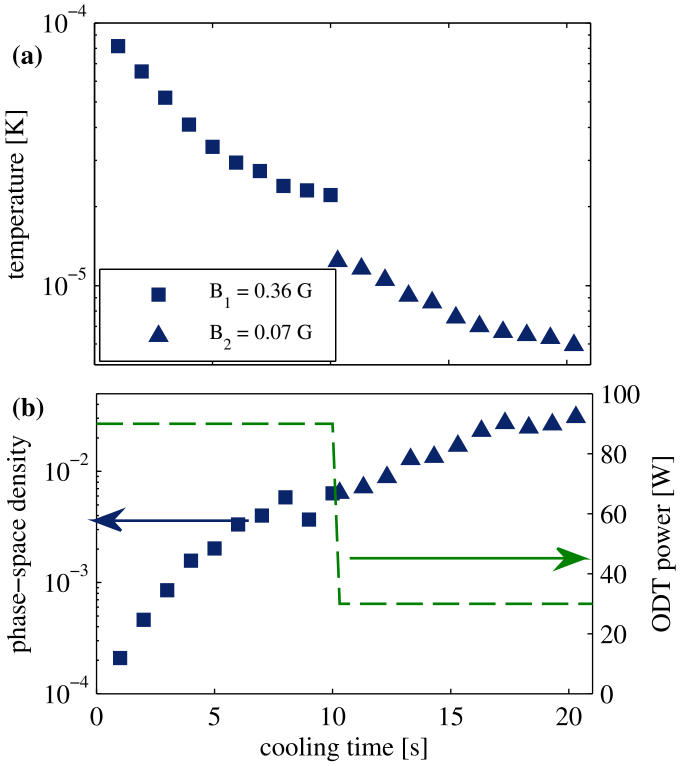

Figure 4.15: Temperature(a) and phase-space density(b) are presented as a function of cooling time in a semi-logarithmic scale. After 10 s of cooling at a high magnetic offset field, the power of the ODT was ramped down within 300 ms (right y-axis in graph (b)) and the magnetic offset field was reduced inducing further cooling. Note that the temperature 'jumps' due to adiabatic decompression when the ODT is ramped.

attribute these losses to excited-state collisions, possibly enhanced by re-absorption of scattered light in the dense medium. The adjustment of the magnetic field leads not only to an increase of dipolar relaxations but also to stronger losses, as discussed below. Nevertheless, the gain of the PSD over the loss in atom number, presented in figure 4.14(c) is superior to evaporative cooling: the absolute value of the initial slope in the doubly logarithmic graph in figure 4.14(c) represents γ_{eff} and amounts to 6 which exceeds typical values (< 4) obtained in evaporative cooling.

Temperatures as low as 6 μK were reached when the confinement of the optical dipole trap was reduced. To this end, the atoms were pre-cooled for a duration of 10 seconds at $\mathrm{B}_1 = 0.36\,\mathrm{G}$ and $P_1 = 90\,\mathrm{W}$. Subsequently, the power of the ODT was linearly ramped to $P_2 = 30\,\mathrm{W}$ within 300 milliseconds, while the magnetic offset field was reduced to $\mathrm{B}_4 = 0.07\,\mathrm{G}$. Opening of the ODT resulted in an adiabatic cooling, which explains the temperature drop at the beginning of the second cooling time, shown in figure 4.15(a). However, adiabatic opening of the potential normally conserves the phase-space density, as it is also the case in graph (b). At the end of the second cooling phase at $t_{\mathrm{end}} = 20.3\,\mathrm{s}$ the phase-space density saturates at a value of 0.03, which is more then factor 2 larger then in figure 4.14 in a tight ODT. It shows that the demagnetization in the tight ODT in not limited by a heating effect that could originate from light scattering induced by a fluctuating magnetic field as discussed below, or any other technical source of heating as suspected in [Fattori et al., 2006].

This result suggests that a density dependent limiting mechanism is present, which will be investigated in the following section. One might also consider further opening the confinement of the ODT in order to reach lower temperatures. Still, in the present set-up the phase-space density is limited by the atom number density which cannot be raised above $5 \times 10^{19} m^{-3}$. Ultimately, in order to achieve the onset of condensation at $T_{\rm min} \approx T_{\rm R} = 1.02\,\mu$K the density must exceed $10^{20} m^{-3}$.

4.4 Limitations of demagnetization cooling

In this section we study the losses occurring during the demagnetization cooling and find that they pose the main limitation in the present experimental implementation. We show that the scaling with density and light intensity is consistent with excited-state collisions. Furthermore, a modified version of the Gallagher-Pritchard [Gallagher and Pritchard, 1989] model for excited-state collisions is used to explain the variation of cooling and losses for positive detunings of the optical pumping light. The absolute strength of the losses is however much stronger compared to previous studies of optical cooling methods.

4.4.1 Technical considerations

First, let us have a brief look at limitations that may arise from technical imperfections rather than physics. As discussed in section 4.3.1, the orientation of the magnetic offset field plays a crucial role in keeping the $m_{\rm S} = -3$ as a dark-state. Static or slowly varying transverse fields can be measured and compensated for. However, the presence of various electric devices in proximity of the experimental chamber inevitably produces fluctuating stray fields, especially at the power line frequency of 50 Hz and its multiples. We measured the amplitude of the oscillating transverse magnetic fields with a fluxgate[4] next to the experimental chamber and show the results in figure 4.16. The amplitudes in the transverse directions are on the order of 1 mG. In the case of low magnetic offset fields below 50 mG the oscillating magnetic fields disturb the dark-state and lead to unwanted scattering of optical pumping light. Active stabilization of the magnetic field has been installed [Wenzel, 2012] and will be used in the future in order to reduce the fluctuations to values below 100 μG [Pasquiou et al., 2011].

In principle, the polarisation of the optical pumping light is only limited by the angle accuracy of the retardation plate rotation stages[5]. We have experimentally checked that variation of the angle of the retardation plates by ±1° did not affect the performance of the cooling.

---

[4] Stefan Mayer Instruments, FLC 100.

[5] Thorlabs, PRM1 with absolute accuracy of 0.1%.

Figure 4.16: Transverse magnetic field fluctuation at frequencies of 50, 100, and 150 Hz. Recorded with an oscilloscope triggered by the power line and averaged over 128 samples.

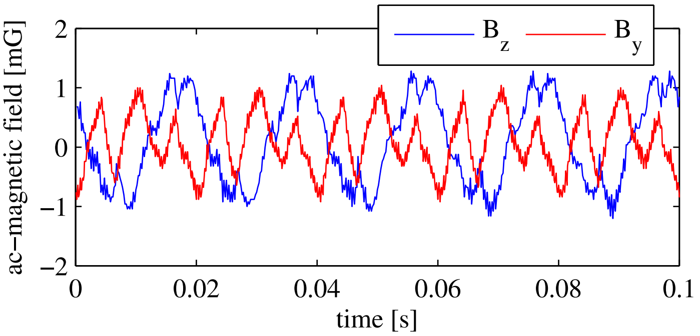

In conclusion, the experiments described in the following were not limited by any known technical imperfections.

4.4.2 Light assisted losses

To study the nature of the losses during the demagnetization cooling we modelled the losses using rate equations and performed additional experiments. In the case of excited state collisions, an atom in the electronic ground states collides with an atom excited by the optical pumping light. In a semi-classical treatment[Gallagher and Pritchard, 1989] the two atoms are considered at rest and separated by a certain distance when an excitation of one atom occurs. After excitation the atoms are accelerated towards or away from each other by the long-range $\pm 1/R^3$ dipole interaction potential, such that a portion of the internal excitation energy is converted to kinetic energy. As a consequence, both atoms may acquire sufficient energy to leave the trap. The increase of kinetic energy depends on the detuning of the excitation laser and will be discussed in section 4.4.3. In general, one expects the losses to scale with the density of the excited state atoms and the density of the ground state atoms.

Rate equations

We model our system using rate equations that describe the populations of the different states. The number of the excited states atoms N_e is proportional to the number of atoms that couple to the optical pumping light field N_c (that is all magnetic sub-states with $m_{\mathrm{S}} > -3$) and the pumping rate Γ_{OP}:

$$N_e = \frac{\Gamma_{\mathrm{OP}}}{\Gamma} N_c \qquad (4.8)$$

where $\Gamma = 2\pi \times 5\,\mathrm{MHz}$ is the transition strength. In all our experiments, we have $\Gamma_{\mathrm{OP}} \ll \Gamma$ and therefore $N_e \ll N_c$. The dynamics of the populations of the magnetic sub-states are governed by a set of differential rate equations. Here, we first consider the case without losses and describe the system in a simplified picture with a dark-state population N_{nc} in the $m_S = -3$ state and coupled states population N_c, which is given by

$$\dot{N}_c = \beta^+_{\rm dr}\frac{N^2_{nc}}{V} - \beta^-_{\rm dr}\frac{N_{nc}N_c}{V} - \Gamma_{\rm OP}N_c \tag{4.9}$$

where V is the temperature dependent effective volume, $\beta^+_{\rm dr}$ is the dipolar relaxation coefficient which determines the rate of spin flips from the $m_S = -3$ state to higher states, $\beta^-_{\rm dr}$ is the coefficient in the reversed direction, and the last term describes the optical pumping back to the dark state. The dipolar relaxation coefficients $\beta^\pm_{dr}$ depend on the temperature and the magnetic field, as described in the theory section 4.1. In order to estimate the general scaling of the populations we assume that at time scales of optical pumping and dipolar relaxations the temperature changes only slowly, therefore the volume and the coefficients $\beta^\pm_{\rm dr}$ are considered constant. As a consequence, dipolar relaxations in both directions and optical pumping are in equilibrium, hence

$$\Gamma_{\rm OP}N_c + \beta^-_{\rm dr}\frac{N_{nc}N_c}{V} = \beta^+_{\rm dr}\frac{N^2_{nc}}{V} \tag{4.10}$$

Let us further examine two extreme cases. In the first case, the optical pumping is much faster than the back-relaxation: $\Gamma_{\rm OP} \gg \beta^-_{\rm dr}\frac{N_{nc}}{V}$. In other words, atoms that are transferred to $m_S > -3$ by a dipolar relaxation, are immediately pumped back. Then, we obtain

$$N_c \approx \beta^+_{\rm dr}\frac{N^2_{nc}}{\Gamma_{\rm OP}V} \tag{4.11}$$

In the opposite case, a quasi-equilibrium of the spin degree of freedom is reached and we get

$$N_c \approx \frac{\beta^+_{\rm dr}}{\beta^-_{\rm dr}}N_{nc} \tag{4.12}$$

Finally, let us consider the dynamics of the total number of ground state atoms $N = N_{nc} + N_c$ including losses and given by

$$\dot{N} = -\gamma_{\rm Bg}N - \beta_{\rm LC}\frac{NN_e}{V} \tag{4.13}$$

The first term on the right hand side corresponds to losses due to collisions with atoms from the background gas with a rate coefficient $\gamma_{\rm Bg} = 0.037\,\mathrm{s}^{-1}$, the second term accounts for the light-assisted collisions with a rate coefficient $\beta_{\rm LC}$. Further we assume that $\beta_{\rm LC}$ is equal for all m_S states.

Density dependent losses

In the following set of experiments, the calculated optical pumping rate is $\Gamma_{\rm OP} \approx 350\,\mathrm{s}^{-1}$ which is much higher than the typical dipolar relaxation rates being on the order of

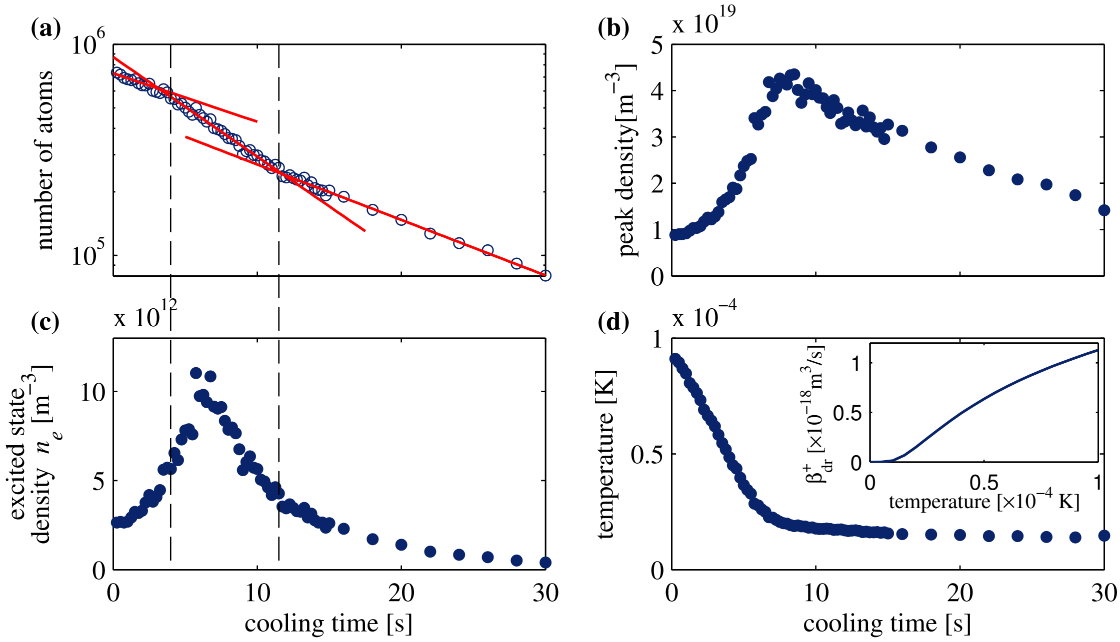

Figure 4.17: Modelling of the increased losses during the demagnetization cooling at a constant magnetic field $\mathrm{B}_1 = 0.36\,\mathrm{G}$. We compare the evolution of the number of atoms in (a) to effective excited state density n_e in (c). We use the peak density (b) and the temperature (d) to determine n_e for each measurement. The inset in (d) shows the dependence of the dipolar relaxation coefficient β^+_{dr} on the temperature. The variation of the observed loss coefficient (different slopes in (a)) is well reproduced by the shape of the curve of n_e.

$10\,\mathrm{s}^{-1}$. We assume therefore that equation 4.11 holds, yielding $N_{nc} \gg N_c$. We plug equation 4.8 into equation 4.13 and substitute N_c by equation 4.11. We obtain

$$
\begin{aligned}
\dot{N} &= -\gamma_{\mathrm{Bg}} N - \beta_{\mathrm{LC}} \frac{N N_e}{V} && (4.14)\\
&= -\gamma_{\mathrm{Bg}} N - \beta_{\mathrm{LC}} \frac{N}{V} \frac{\Gamma_{\mathrm{OP}}}{\Gamma} N_c && (4.15)\\
&= -\gamma_{\mathrm{Bg}} N - \beta_{\mathrm{LC}} \frac{N}{V} \frac{\Gamma_{\mathrm{OP}}}{\Gamma} \beta^+_{\mathrm{dr}} \frac{N^2_{nc}}{\Gamma_{\mathrm{OP}} V} && (4.16)\\
&= -\gamma_{\mathrm{Bg}} N - \beta_{\mathrm{LC}} \underbrace{\frac{\beta^+_{\mathrm{dr}}}{\Gamma} \frac{N^2_{nc}}{V^2}}_{\equiv n_e} N && (4.17)
\end{aligned}
$$

First, we find that the scattering rate Γ_{OP} drops out, thus we denote this regime as saturated. Second, in this saturated regime the loss coefficient from excited-state collisions is proportional to the excited-state density $n_e = \frac{\beta^+_{\mathrm{dr}}}{\Gamma} \frac{N^2_{nc}}{V^2} \approx \frac{\beta^+_{\mathrm{dr}}}{\Gamma} \frac{N^2}{V^2}$. In order to observe this scaling we performed a cooling sequence at a constant magnetic field $\mathrm{B}_1 = 0.36\,\mathrm{G}$. We varied the cooling time and recorded the number of atoms, the peak density and the temperature of the sample. The results are plotted in figure 4.17. The number of atoms is plotted versus cooling time in figure 4.17(a). In order to show the effect of light-assisted losses we plot the effective excited state density n_e in figure 4.17(c). We calculate n_e for each data-point by using the measured peak density (b) as $\frac{N}{V}$ and determining the dipolar relaxation coefficient β^+_{dr}(inset) from the measured temperature in figure 4.17(d). The loss of atoms during the final 18 seconds can be well fitted by an exponential decay with a loss coefficient $\gamma_1 = 0.06\,\mathrm{s}^{-1}$. This value of the loss coefficient also fits to the first 4 seconds of the cooling sequence. However, in the time interval between 4 and 12 seconds we observe a stronger decay with $\gamma_2 = 0.11\,\mathrm{s}^{-1}$. At the same times the calculated excited state density in (c) shows strong variations due to the changing density and temperature of the sample. As emphasised by the vertical dashed lines the increased loss of atoms coincides with the peak of the calculated excited state density n_e. This agreement indicates the validity of our model in the saturated regime.

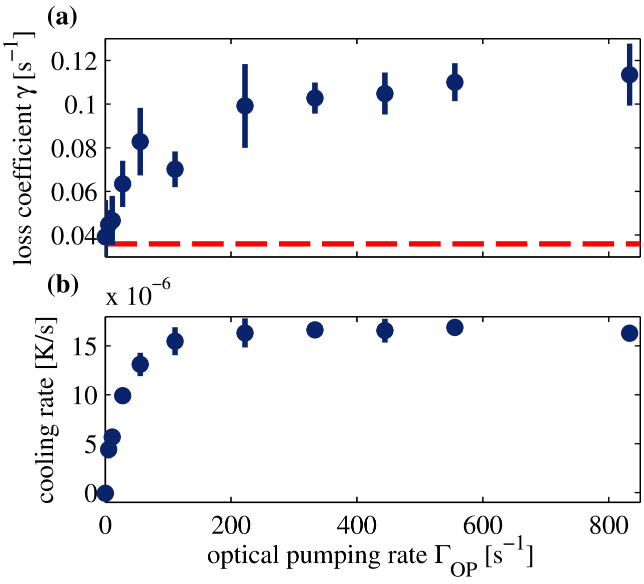

Figure 4.18: Loss coefficient (a) and cooling rate (b) are plotted versus the optical pumping rate. The dashed line in (a) corresponds to background losses in the absence of cooling. The saturation of the cooling and the losses indicate that optical pumping rate above $100\,\mathrm{s}^{-1}$ greatly exceeds the dipolar relaxation rate. The error bars show the standard deviation estimated by the fit-routine.

We can relate the observed loss rate coefficient γ_2 and the corresponding excited state density (for simplicity we take the peak value) to estimate the value of the rate coefficient $\beta_{\mathrm{LC}}^{\mathrm{exp}} = \frac{\gamma_2-\gamma_{\mathrm{Bg}}}{\max(n_e)} \approx 6.5 \times 10^{-15}\,\mathrm{m}^3\mathrm{s}^{-1}$. In the limit when each collision of an excited atom and a ground state atom leads to a loss, the rate coefficient can be calculated using the Condon radius R_{C} (see definition in section 4.4.3) to calculate the cross-section $\sigma_{\mathrm{LC}} = 4\pi R_{\mathrm{C}}^2$. Hence, the maximal theoretical loss rate coefficient is given by $\beta_{\mathrm{LC}}^{\mathrm{th}} \approx \sigma_{\mathrm{LC}} v_{\mathrm{T}}$, where v_{T} is the average relative velocity [Julienne and Vigué, 1991]. For a temperature of $25\,\mu$K and a detuning of $72\,\Gamma$ we get $\beta_{\mathrm{LC}}^{\mathrm{th}} = 4 \times 10^{-16}\,\mathrm{m}^3\mathrm{s}^{-1}$, which is more than one order of magnitude smaller than the observed loss rate coefficient. This discrepancy may be due to the unusually high density leading to the loss of multiple atoms from one excitation.

Intensity dependent losses

In the next set of experiments we varied the intensity of the optical pumping light for each cooling sequences at the same magnetic field B_1 as used above. We extracted the initial cooling rate from a linear fit to the first 4 seconds of the temperature evolution. Because of the complex interplay of the demagnetization cooling and light-assisted losses described above, we use an effective loss coefficient γ in order to compare different optical pumping light intensities. We obtain γ from an exponential fit to the number of atoms over the first 10 seconds. Both the cooling rate and the loss coefficient are plotted as a function of the optical pumping rate in figure 4.18. The data points corresponding to the lowest pumping light intensities are in the regime where $\Gamma_{\mathrm{OP}} \geq \beta^{-}_{\mathrm{dr}} \frac{N_{nc}}{V}$. Therefore, substituting N_c in equation 4.8 by equation 4.12 leads to a linear dependence of the excited state population on the optical pumping rate, similar to the results in works on light-assisted collisions in magneto-optical traps [Weiner et al., 1999]. As a consequence, the cooling rate and the effective loss coefficient increase at low optical pumping rates. In the saturated regime i.e. $\Gamma_{\mathrm{OP}} \gg \beta^{-}_{\mathrm{dr}} \frac{N_{nc}}{V}$, the cooling reaches a constant value. The effective loss coefficients saturate (within error bars) for pumping rates above $100\,s^{-1}$. Residual increase of losses for larger intensities might originate from stray light with uncontrolled and random polarisation.

4.4.3 Detuning dependent losses

Light-assisted collisions are expected to strongly depend on the detuning of the pumping light [Sesko et al., 1989, Fuhrmanek et al., 2012]. In order to avoid complications arising from bound molecular states and fine-structure changes, we limit the discussion here to positive detuning. This means that atoms interact via a repulsive C_3/R^3 potential with $C_3 = \frac{3\hbar\Gamma}{4}\left(\frac{\lambda}{2\pi}\right)^3$ when one of the atoms is excited, as illustrated in figure 4.19. The interaction energy is then given by $E_{\mathrm{int}} = C_3/R_0^3$, where R_0 is the interatomic distance at which the excitation takes place. We modify the semi-classical picture of [Gallagher and Pritchard, 1989] by assuming that the interaction energy is fully converted into kinetic energy[6] and both atoms are lost when this kinetic energy exceeds the depth of the ODT. This process is commonly known as radiative escape. The excitation probability within the interaction potential is given by

$$P_{\mathrm{exc}} = \frac{s_0/2}{1 + s_0 + \left(\frac{2\delta'}{\Gamma}\right)^2} \quad \text{with} \quad \delta' = \delta - \frac{C_3}{\hbar R^3} \tag{4.18}$$

where $s_0 = I/I_{\mathrm{S}}$ is the saturation parameter and δ is the detuning. Since the interaction potential shifts the resonance, one can then define a distance of resonant interaction as $R_{\mathrm{C}} = \left(\frac{C_3}{\hbar\delta}\right)^{\frac{1}{3}}$, often denoted as Condon radius. Already one can see that for increasing

---

[6] Hereby we neglect the probability of survival coming from the lifetime of the excited state.

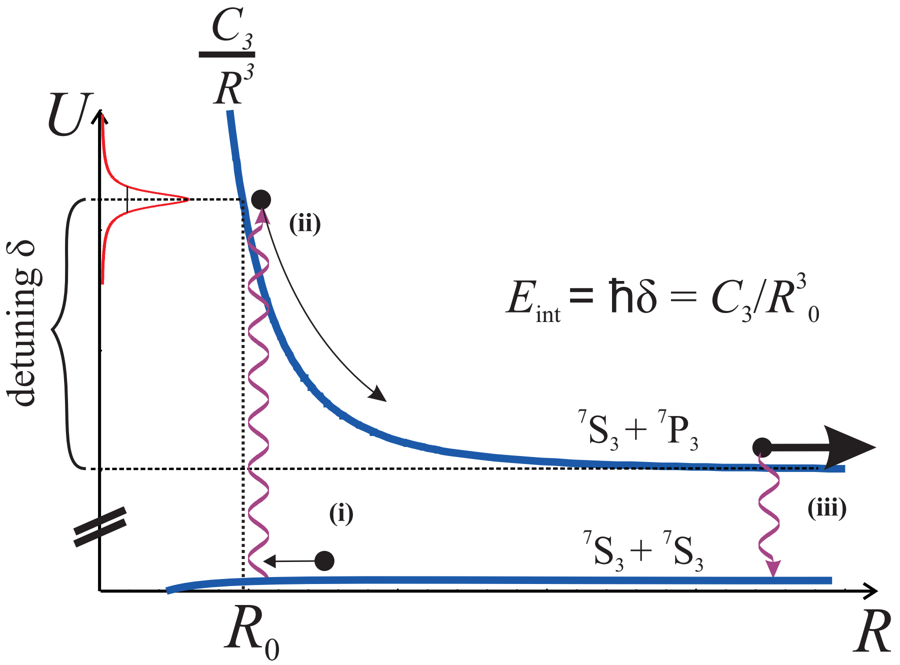

Figure 4.19: The process of a radiate escape for positive detuning is illustrated. The interaction potentials for both atoms in the electronic ground state ($^7S_3$ + $^7S_3$) and one of atoms in the excited state ($^7S_3$ + $^7P_3$) are shown as a function of the interatomic distance R. When two atoms approach **(i)**, the short-ranged ground-state potential is flat at large interatomic distances. The excitation occurs preferably at a distance R_0 where the frequency shift due to the long-range C_3/R^3 potential matches the detuning δ. The red profile illustrates the excitation probability for a given detuning. **(ii)** The two atoms are repelled from each other by the $^7S_3$ + $^7P_3$ potential. De-excitation takes place at large distances **(iii)** such that the interaction energy E_{int} is converted into kinetic energy, possibly allowing the two atoms to leave the trap.

detuning the Condon radius and thereby the surface area $4\pi R_C^2$ of a sphere at which the excitation is resonant shrink. At the same time, the slope of the interaction potential increases, therefore the near-resonant region around the Condon radius also diminishes in width. In other words, the resonant volume decreases for large detuning. From this geometrical argument one expects a decrease of losses. In order to obtain the loss probability, we integrate P_{exc} over a sphere in which the interaction energy is larger than twice the depth of the trap U_{ODT}

$$P_{\text{loss}} = \frac{1}{V_{\bar{\lambda}}} \int_0^{R_{\text{loss}}} 4\pi R^2 P_{\text{exc}}(R) dR \quad \text{with} \quad R_{\text{loss}} = \left(\frac{C_3}{U_{\text{ODT}}} \right)^{1/3} \tag{4.19}$$

where $V_{\bar{\lambda}} = \frac{4\pi}{3} \left(\frac{\lambda}{2\pi} \right)^3$ is the interaction volume. Indeed, at a constant intensity the loss probability rapidly decreases as a function of increasing detuning, which is consistent with results obtained in [Sesko et al., 1989]. In our particular experiment, we require a

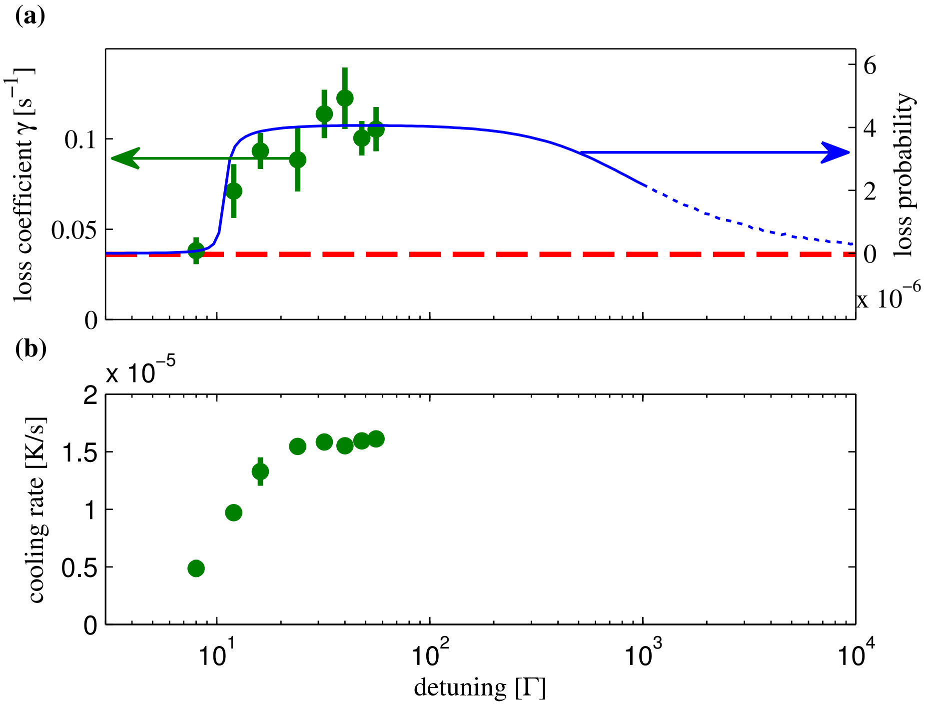

Figure 4.20: Loss coefficient (a, left axis) and cooling rate (b) are plotted as a function of optical pumping light detuning. Additionally, the calculated loss probability (see text) is plotted versus detuning in (a, right axis) for comparison. The dotted line indicates that for large detunings short-range molecular potentials as well as structures of the wave-functions are important, which is not included in the model. The error bars show the standard deviation estimated by the fit-routine.

constant (off-resonant) scattering rate to maintain the demagnetization cooling. Therefore, we increase the optical pumping intensity according to

$$\Gamma_{\mathrm{OP}} = \frac{\Gamma}{2}\frac{s_0}{1+s_0+\left(\frac{2\delta}{\Gamma}\right)^2} \quad\Rightarrow\quad s_0 \approx \frac{2\Gamma_{\mathrm{OP}}}{\Gamma}\left(1+\left(\frac{2\delta}{\Gamma}\right)^2\right) \tag{4.20}$$

for $\frac{2\Gamma_{\mathrm{OP}}}{\Gamma} \ll 1$. Away from the resonance, the saturation parameter s_0 scales with the square of the detuning. We plug s_0 into equation 4.18 and see that although the resonant surface $4\pi R_{\mathrm{C}}^2$ decreases with detuning, the loss probability is partially balanced by the quadratically increasing intensity. For large detunings, the saturation parameter $s_0 \gg 1$ leads to a power broadening of the transition.

We performed a series of cooling experiments at different detunings in order to check the aforementioned model. The experimental sequence was very similar to section 4.4.2, where we recorded the number of atoms and the temperature for increasing cooling times. We extracted the effective loss coefficient from the decay of the number of atoms and the cooling rate from the first 4 seconds of cooling. The magnetic offset field during

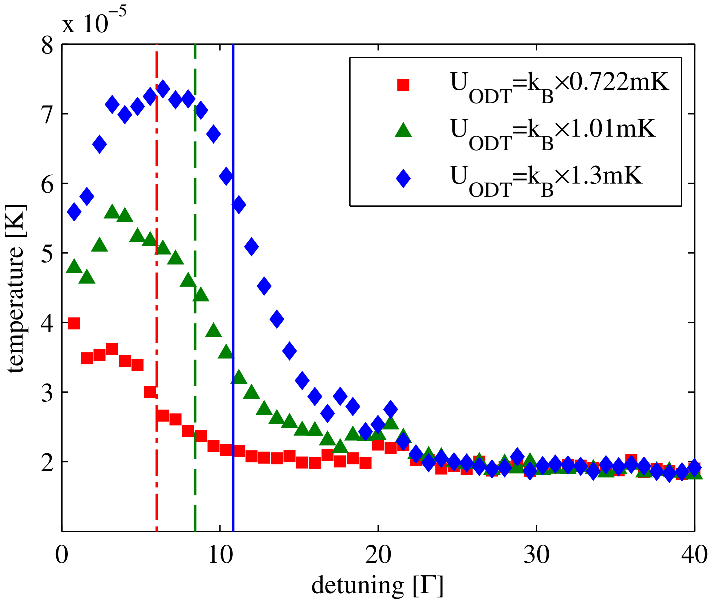

Figure 4.21: Temperature after 10 seconds of cooling is plotted versus the cooling detuning. The different symbols correspond to cooling at decreasing depth of the optical dipole tap, as indicated in the legend. The vertical lines indicate the energy (in units of frequency) required for a radiate escape at the given trap depth.

the cooling time was held at $B_x = 0,36\,\mathrm{G}$, while the intensity of the optical pumping light was varied to match the detuning such that the optical pumping rate was held constant at $\Gamma_{\mathrm{OP}} \approx 700\,\mathrm{s}^{-1}$. Figure 4.20 shows the obtained results. The solid blue line in (a) corresponds to the calculated loss probability using equation 4.19 and experimental parameters; in particular the depth of the ODT defines the edge at a detuning $\approx 10\,\Gamma$.

Note that the cooling rate drops when coming from large detuning in the range between $20 - 10\,\Gamma$. In the context of excited-state collisions this can be interpreted as heating due to collided atoms that did not obtain sufficient energy to leave the trap. The interaction energy is therefore redistributed via elastic collisions in the sample.

Since excited-state collisions at low detunings appear to affect the efficiency of the demagnetization cooling, we studied the dependence of the temperature after a fixed cooling time $t_{\mathrm{cool}} = 10\,\mathrm{s}$ for different detunings and depths of the ODT. As above, the intensity of the optical pumping light was adjusted for each detuning value, the magnetic offset field was set to $B_x = 0.36\,\mathrm{G}$. The experiment was performed for three different settings of the optical dipole trap power ($P_{\mathrm{ODT}} = 50, 70, 90\,\mathrm{W}$), the results are shown in figure 4.21. At large values of detuning the temperature after 10 seconds is constant, as for values close to resonance the cooling strongly depends on the depth of the dipole trap. We observe smeared out temperature-'edges' as a function of detuning. The centres of the edges shift to lower values of detuning for decreased depth of the optical dipole trap, as one would expect for radiative escape events. The vertical lines mark the energy (in units of frequency×$\hbar$) required for two atoms to leave the trap as a result of an excited-state collision and full conversion of the interaction energy into kinetic energy. We obtain a good agreement between the experimentally measured edges and the calculated values. It is likely that elastic collisions with cold atoms in the cloud during the radiative escape are responsible for smearing out of the edge.

In summary, in the currently accessible detuning range we observe only minor variations of the total loss rate, with the exception of reduced losses close to the resonance. On the red side (negative detuning), apart from strong loss features right below the resonance, which we attribute to photo-association of molecules, the loss rates are similar to those measured at large positive detuning.

4.5 Conclusion

Demagnetization cooling starting directly after the continuous loading of a ODT down to only a few recoil energies is a significant improvement over the previously achieved results. The absolute phase-space density is raised by more than two orders of magnitude to a value of 0.03, which ranks among the highest phase-space densities achieved with optical cooling only [Ido et al., 2000], in our case however *without* the need of a narrow-line transition. Compared to standard evaporation cooling, we have shown that demagnetization cooling is more efficient in terms of phase-space density gain versus the loss of atoms. This fact makes this cooling technique not only interesting by itself, but presents a remarkable alternative cooling strategy for dipolar species in general.

However, we have also observed losses of atoms that are related to demagnetization cooling. From the experimental evidence presented in this chapter we conclude that collision involving atoms in the excited state prevent us from reaching density higher than $5 \times 10^{19} m^{-3}$ under given experimental parameters. Due to the losses and hence a strongly reduced number of atoms the relaxation rate stagnates and eventually the cooling stops.

For very large detunings on the order of 10-100 GHz excited-state collisions may be strongly suppressed when the internuclear distance of resonant absorption coincides with the node in the ground state wave-function [Burnett et al., 1996].

5 Summary and outlook

In the present work, we have explored the optical pumping as an efficient means to increase phase-space density by Sisyphus cooling of continuously loaded chromium atoms and demagnetization cooling of a trapped chromium gas. In both cases, the optical pumping dissipates potential energy by spontaneous emission. First, we studied the loading mechanism allowing to transfer chromium atoms from a guided beam into a conservative trap at rest. The low-field seeking atoms travel along the minimum of a magnetic guide. The atoms are funnelled into an optical dipole trap at the centre of which they run into a state-dependent magnetic barrier and convert a part of the kinetic energy into potential energy in a single slowing step. The dissipation of the potential energy via the transfer to the high-field seeking state is realized by scattering of a few optical pumping photons. Depending on the remaining kinetic energy the atom may still be able to quickly leave the trap, for example in the radial direction where trap depth is generally lower than in the axial direction. We have shown that the amount of remaining energy is a crucial parameter for the efficiency of the loading mechanism, especially when the initial beam conditions are varied over a wide range. Therefore, we have implemented an additional simultaneous cooling, consisting of multiple iterations of the slowing step, that makes the combined loading and cooling insensitive to the initial conditions. This form of Sisyphus cooling was readily implemented by applying a weak radio-frequency field. As a consequence, atoms were transferred to higher magnetic states during the oscillation inside the trap, and thus did not regain the full kinetic energy at the passage of the trap centre. We demonstrated a gain of up to nine orders in phase-space density and a maximal phase-space density reaching 4×10^{-4} in steady-state. Furthermore, we achieved high number density enabling efficient evaporation cooling during the loading (and contributing to the final phase-space density) essentially independent of the incident flux or radial temperature of the beam. In conclusion, the Sisyphus-enhanced continuous loading can be seen as a generally applicable loading mechanism, since it does not require a closed laser cooling transition (as emphasised in [Falkenau et al., 2011]) and can be applied to particle beams with a broad range of initial conditions.

In the second part of this work, we investigated the demagnetization cooling of chromium atoms. We have shown that intrinsic spin-orbit coupling via dipolar relaxation (instead of radio-frequency transitions) populated higher magnetic sub-states at the cost of energy from the motional degree of freedom. In this context, optical pumping into the lowest magnetic sub-state can be seen as cooling of the spin degree of freedom, while dipolar relaxation drives the thermalization between the spin and the motional degree of freedom. As a result, each photon can dissipate energy on the order of the thermal energy leading to a highly efficient cooling method which allows reaching an absolute phase-space density of 0.03 by optical means only. This result is therefore an important step towards the experimental realization of a system in which Bose-Einstein condensation can be reached by optical means only, i.e a quantum phase-transition driven by optical pumping [Santos et al., 2001, Cirac and Lewenstein, 1996]. We have also shown evidence that light-assisted losses pose a hurdle to reaching higher densities at lower temperature, a prerequisite for Bose-Einstein condensation. We have established models based on rate equations for the loss process and found qualitative agreement in the scaling of the losses with the intensity and the density of the cooled sample. Though the gravity of the observed loss effect is not fully understood and needs further studying, as will be discussed below.

Outlook

Based on the obtained results, we briefly present and discuss some promising prospects for future experiments.

Towards truly continuous BEC

The presented experimental apparatus is designed to perform a series of phase-space density-increasing steps similar to a conveyor belt, that is – simultaneously. Unlike most experimental set-ups, here the cooling stages (MOT, Doppler-cooling, continuous loading, Sisyphus cooling) are separated in space and operate at the same time. As mentioned above, phase-space density of 4×10^{-4} is reached in a continuous operation.

The next stage is the investigation of the so-called 'dimple trick‘ in the continuous regime. First demonstrated in [Stamper-Kurn et al., 1998b], the idea of this technique consists in adiabatically compressing a small fraction of the trapped sample, thereby strongly increasing the local density, while staying in thermal contact with a large heat bath. The local phase-space density can be increased by several orders of magnitude in a reversible way. Another way of describing this effect is by regarding the local compression as a global change of the potential power-law, which then also leads to a change of the phase-space density. A strongly focused laser beam has already been implemented in the current apparatus by Hannes Gorniaczyk [Gorniaczyk, 2012]. This optical dimple is displaced from the axial centre of trap as shown by the local density increase in figure 5.1(a). In this configuration the dimple is located outside of the optical pumping

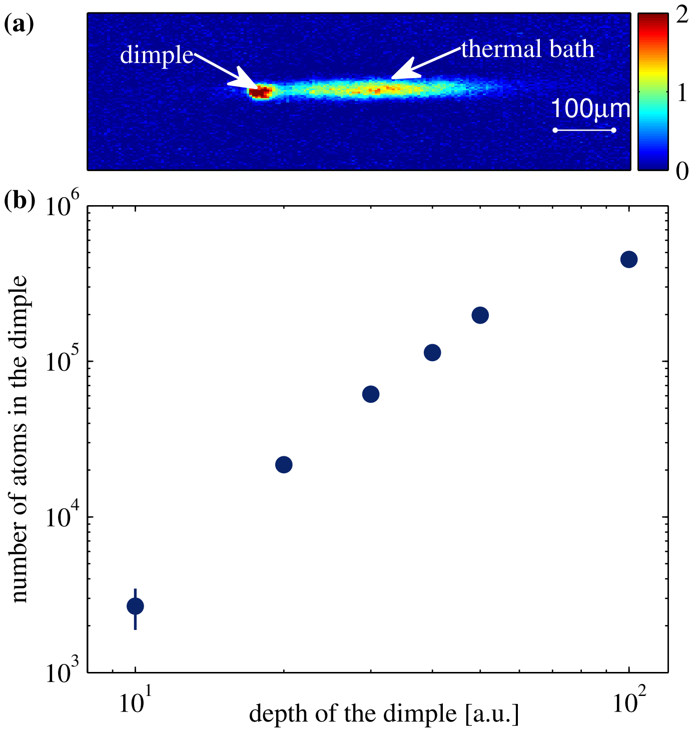

Figure 5.1: Absorption picture of a continuously loaded trap with a locally increased density is shown in (a). The colour code denotes the optical density of the atomic cloud. The density increase is induced by an additional strongly focused optical dipole trap(dimple). Number of atoms (measured after the removal of the thermal bath and a time of flight) versus the depth of the dimple are shown in (b) in a doubly logarithmic scale. The error bars denote the standard deviation of 5 independent repetitions.

beam but stays in contact with the atomic cloud, therefore the density boost should not be limited by light-assisted losses. The accumulation of atoms inside of the dimple takes place by elastic collisions, therefore the dimple can be regarded as a realization of a continuously loaded non-dissipative trap as proposed in [Roos et al., 2003]. In a preliminary experiment, we recorded the number of atoms loaded into the dimple as a function of the dimple depth, as shown in figure 5.1(b). We observed a strong increase of dimple-population until the number of atoms becomes comparable to that of the bath.

In future, the phase-space density gain needs to be accurately determined, by specifically taking the non-harmonic trapping potential into account. In particular the combination of the Sisyphus cooling mechanism at low magnetic barrier field (as discussed in section 3.7) yielding steady-state temperatures around 50 μK and a deep dimple potential may lead to a big step in phase-space density towards a truly continuous Bose-Einstein condensate.

Sisyphus cooling in a hybrid trap

In section 3.5, we have shown that Sisyphus cooling is able to reach collisional regime in the continuously loaded trap despite a very weak source. This scheme could be thus applied to a wide range of atomic or molecular beams, provided state dependent potentials can be realized using external fields and transitions for fast optical pumping are available.

In the case of pulsed loading experiments (e.g. [van de Meerakker et al., 2005, Narevicius et al., 2008]) Sisyphus cooling could also be used to bring a trapped but dilute sample to a density allowing for collisional thermalization, a prerequisite for subsequent evaporative cooling. During a collision-less phase of the Sisyphus cooling one would obtain truncated energy distributions, similar to results in section 3.4.1. Therefore, the driving frequency would have to be adapted continuously or in steps in order to resume the cooling process. At some density, collisions would begin to produce high-energetic atoms, resulting in an increase of cooling efficiency. Open questions to be addressed are what phase-space density can be reached using such a scheme, and whether sub-recoil temperatures can be obtained for sufficiently large η_{RF} (see section 3.4.2). From the experience with demagnetization cooling, light-assisted losses may play an important role here as well. However, it is important to note that dipolar relaxation is not required in the case of RF-driven Sisyphus cooling. Therefore the density constraints for the continuation of the cooling are much lower than for demagnetization cooling. In conclusion, such as a scheme deserves experimental investigation.

Excited-state collisions and molecular resonances

Demagnetization cooling relies on high density (typically above $10^{19}\,\mathrm{m}^{-3}$) of the gas, since the cooling rate directly depends on the dipolar relaxation rate. As we have shown in section 4.4.2, high density significantly increases losses, which we attribute to collisions between ground-state and excited-state atoms. We studied the loss coefficient for positive detuning involving free excited-states. In the original work on excited-state collisions [Gallagher and Pritchard, 1989], the authors treat the case of negative detuning and describe the motion of atoms after the excitation using classical equations. They justify this approach by assuming an excitation to a coherent superposition of several bound molecular states. This is valid as long as the level spacing between the excited vibrational levels is smaller than the transition line-width. However it is clear that for large negative detunings, one should be able to resolve the deeper bound states. On the one hand, the accurate measurement of the energy of the excited vibrational states [Thorsheim et al., 1987, Lett et al., 1993] can be used to further improve the understanding of chromium molecules [Andersson, 1995]. On the other hand, this should also allow suppressing excited state-collisions by choosing a detuning in between of two molecular states.

Another way to suppress excited-state collisions is to tune the optical pumping laser such that the resonant internuclear distance coincides with the first zero-crossing of the ground-state wave-function, as proposed by [Burnett et al., 1996]. In the limit of s-wave scattering, the zero-crossing distance is approximately equal to the scattering length $a = 102\,\mathrm{a}_0$, while the corresponding detuning depends on the C_3 factor and lies in the range of 10-30 GHz [Rührig, 2014]. In order to maintain the off-resonant scattering rate Γ_{OP} sufficiently high (see section 4.4.2) additional laser power is required for such large detuning. In the currently on-going experimental efforts , a new laser system has been installed, delivering more than 100 mW of light around 427 nm and allowing for a detuning of several tens of GHz. As mentioned in section 2.1.1, state-dependent *optical* potentials can be realized when the detuning is comparable or smaller than the fine-structure splitting. Hence, the new laser system can also be used to produce laser induced quadratic Zeeman shift[Santos et al., 2007]. In other words, in addition to the normal Zeeman shift produced by the magnetic offset field, the energy of coupled atoms (those with magnetic sub-state $m_{\mathrm{S}} > -3$) is shifted by the optical field. This effect can be used to finely control the energy splitting between the magnetic sub-states.

Reabsorption

In the present work, the atoms in the lowest magnetic sub-state with the quantum number $m_{\mathrm{S}} = -3$ are considered 'dark' because they do not couple to the circularly polarized optical pumping light. However, the scattered photon produced in an optical pumping event is necessarily linearly polarized, since it stems from a $\Delta m_{\mathrm{S}} = 0$ transition, hence the dark state is not dark with respect to photons spontaneously emitted by other atoms. In the presence of the optical pumping light, the reabsorption cross-section of such a fluorescence photon is equal to the resonant cross-section even for an off-resonant pumping [Castin et al., 1998]. The result of reabsorption is multiple scattering and radiation trapping in the optically dense medium. A quantitative study of radiation trapping in a caesium MOT was reported in [Fioretti et al., 1998]. Furthermore, a slow diffusion of scattered light and frequency redistribution are investigated in [Labeyrie et al., 2003]. In both works, the optical density of the atomic sample was on the order of 20, which is comparable to our experiments. However, the excitation occurs close to the atomic resonance and the Doppler width of the sample is negligible compared to the natural line-width, whereas in our work the experiments are performed at large detuning. According to [Cohen-Tannoudji et al., 1998], the optical pumping rate Γ_{OP} defines the line-width of the scattered light in the limit of weak and off-resonant coupling (coherent scattering). Then, reabsorption can be suppressed by a factor $\frac{\Gamma_{\mathrm{OP}}}{\omega_{\mathrm{D}}}$, where ω_{D} is the Doppler-width of the atoms [Castin et al., 1998], provided the line-width of the optical pumping laser does not exceed Γ_{OP}.

Reabsorption and thus enhanced scattering could be responsible for a heating rate and an increased strength of the light-assisted losses, however, this assumption needs to be confirmed experimentally[1]. For example, based on [Castin et al., 1998], varying of the line-width of the optical pumping laser between the optical pumping rate Γ_{OP} and the Doppler-width ω_{D} of the sample should have a direct impact on the cooling and loss rates.

Towards optical pumping into degeneracy

Suppression of reabsorption and light-assisted losses would pave the way to the long-standing goal of reaching quantum degeneracy by optical means only. An all-optical route to degeneracy via demagnetization cooling or Sisyphus cooling would then represent a real breakthrough. Alternatively, evaporative cooling could be used to prepare a cold and depolarized sample on the verge of condensation. Then, it should be possible to optically polarize the atoms and obtain a condensation process driven by optical pumping.

In any case, it would allow studying the so-called Bose-accumulation regime [Cirac and Lewenstein, 1996], in which quantum interference is at heart of the condensation. The role of the photon involved in such a process is of special interest: the emission of the photon is then subject to bosonic stimulation. However, unlike in a laser, where a strongly occupied *photonic* mode is present, here the *atom* is stimulated into the macroscopically occupied ground state, while the photon ensures the momentum and energy conservation. Therefore, one might also expect a change in the radiation pattern of the emitted photons.

---

[1] Note, that in the case of demagnetization cooling, a single re-emitted linearly polarized photon most likely would be reabsorbed only once, promoting thereby a dark atom into a bright state and leaving the cloud as a circularly polarized photon. Still, this (new) bright atom could then scatter another photon from the optical pumping beam, re-emit a linearly polarized photon and so on. In total, this would have to the same effect as a multiply scattered single photon, but it would be not possible to observe a frequency redistribution or slower decay of fluorescence as it was done in [Fioretti et al., 1998, Labeyrie et al., 2003].

List of publications

- Volchkov, V. V., Rührig, J., Pfau, T., and Griesmaier, A. (2013). Sisyphus cooling in a continuously loaded trap. *New Journal of Physics*, 15(9):093012.
- Volchkov, V. V., Rührig, J., Pfau, T., and Griesmaier, A. (2013). Efficient demagnetization cooling of atoms and its limits. *arXiv 1306.3365.*
- Falkenau, M., Volchkov, V. V., Rührig, J., Gorniaczyk, H., and Griesmaier, A. (2012). Evaporation-limited loading of an atomic trap. *Phys. Rev. A*, 85:023412.
- Falkenau, M., Volchkov, V. V., Rührig, J., Griesmaier, A., and Pfau, T. (2011). Continuous loading of a conservative potential trap from an atomic beam. *Phys. Rev. Lett.*, 106(16):163002.
- Aghajani-Talesh, A., Falkenau, M., Volchkov, V., Trafford, L., Pfau, T., and Griesmaier, A. (2010). Laser cooling of a magnetically guided ultra cold atom beam. *New J. Phys*, 12:065018

Bibliography

[Aghajani-Talesh et al., 2009] Aghajani-Talesh, A., Falkenau, M., Griesmaier, A., and Pfau, T. (2009). A proposal for continuous loading of an optical dipole trap with magnetically guided ultra cold atoms. *Journal of Physics B: Atomic Molecular and Optical Physics*, 42:245302.

[Aghajani-Talesh et al., 2010] Aghajani-Talesh, A., Falkenau, M., Volchkov, V., Trafford, L., Pfau, T., and Griesmaier, A. (2010). Laser cooling of a magnetically guided ultra cold atom beam. *New J. Phys*, 12:065018.

[Allen, 2004] Allen, M. P. (2004). Introduction to molecular dynamics simulation.

[Alt, 2002] Alt, W. (2002). An objective lens for efficient fluorescence detection of single atoms. *Optik - International Journal for Light and Electron Optics*, 113(3):142 – 144.

[Ammann and Christensen, 1997] Ammann, H. and Christensen, N. (1997). Delta kick cooling: A new method for cooling atoms. *Phys. Rev. Lett.*, 78:2088–2091.

[Anderson and Kasevich, 1998] Anderson, B. P. and Kasevich, M. A. (1998). Macroscopic quantum interference from atomic tunnel arrays. *Science*, 282(5394):1686–1689.

[Anderson et al., 1995] Anderson, M. H., Ensher, J. R., Matthews, M. R., Wieman, C. E., and Cornell, E. A. (1995). Observation of bose-einstein condensation in a dilute atomic vapor. *Sience*, 269:198.

[Andersson, 1995] Andersson, K. (1995). The electronic spectrum of cr2. *Chemical Physics Letters*, 237(34):212 – 221.

[Aspect et al., 1988] Aspect, A., Arimondo, E., Kaiser, R., Vansteenkiste, N., and Cohen-Tannoudji, C. (1988). Laser cooling below the one-photon recoil energy by velocity-selective coherent population trapping. *Phys. Rev. Lett.*, 61:826–829.

[Barry et al., 2012] Barry, J. F., Shuman, E. S., Norrgard, E. B., and DeMille, D. (2012). Laser radiation pressure slowing of a molecular beam. *Phys. Rev. Lett.*, 108:103002.

[Bergeman et al., 1987] Bergeman, T., Erez, G., and Metcalf, H. J. (1987). Magnetostatic trapping fields for neutral atoms. *Phys. Rev. A*, 35:1535–1546.

[Bethlem et al., 1999] Bethlem, H. L., Berden, G., and Meijer, G. (1999). Decelerating neutral dipolar molecules. *Phys. Rev. Lett.*, 83(8):1558–1561.

[Billy et al., 2008] Billy, J., Josse, V., Zuo, Z., Bernard, A., Hambrecht, B., Lugan, P., Clement, D., Sanchez-Palencia, L., Bouyer, P., and Aspect, A. (2008). Direct observation of Anderson localization of matter waves in a controlled disorder. *Nature*, 453(7197):891–894.

[Bird, 1994] Bird, G. A. (1994). *Molecular Gas Dynamics and the Direct Simulation of Gas Flows (Oxford Engineering Science)*. Oxford University Press, USA, 2nd edition.

[Bloch et al., 2008] Bloch, I., Dalibard, J., and Zwerger, W. (2008). Many-body physics with ultracold gases. *Rev. Mod. Phys.*, 80:885–964.

[Bohn et al., 2009] Bohn, J. L., Cavagnero, M., and Ticknor, C. (2009). Quasi-universal dipolar scattering in cold and ultracold gases. *New Journal of Physics*, 11(5):055039.

[Bradley et al., 1995] Bradley, C. C., Sackett, C. A., Tollett, J. J., and Hulet, R. G. (1995). Evidence of bose-einstein condensation in an atomic gas with attractive interactions. *Physical Review Letters*, 75:1687.

[Burnett et al., 1996] Burnett, K., Julienne, P. S., and Suominen, K.-A. (1996). Laser-driven collisions between atoms in a bose-einstein condensed gas. *Phys. Rev. Lett.*, 77:1416–1419.

[Castin et al., 1998] Castin, Y., Cirac, J. I., and Lewenstein, M. (1998). Reabsorption of light by trapped atoms. *Phys. Rev. Lett.*, 80:5305–5308.

[Chikkatur et al., 2002] Chikkatur, A. P., Shin, Y., Leanhardt, A. E., Kielpinski, D., Tsikata, E., Gustavson, T. L., Pritchard, D. E., and Ketterle, W. (2002). A continuous source of bose-einstein condensed atoms. *Science*, 296:2193.

[Chin et al., 2009] Chin, C., Flambaum, V. V., and Kozlov, M. G. (2009). Ultracold molecules: new probes on the variation of fundamental constants. *New Journal of Physics*, 11(5):055048.

[Chu et al., 1985] Chu, S., Hollberg, L., Bjorkholm, J., Cable, A., and Ashkin, A. (1985). Three-dimensional viscous confinement and cooling of atoms by resonance radiation pressure. *Phys.Rev.Lett.*, 55:48.

[Cirac and Lewenstein, 1996] Cirac, J. I. and Lewenstein, M. (1996). Pumping atoms into a bose-einstein condensate in the boson-accumulation regime. *Phys. Rev. A*, 53(4):2466–2476.

[Cohen-Tannoudji et al., 1998] Cohen-Tannoudji, C., Dupont-Roc, J., and Grynberg, G. (1998). *Atom-Photon Interactions (Wiley Science Paperback Series)*. Wiley-VCH.

[Cren et al., 2002] Cren, P., Roos, C., Aclan, A., Dalibard, J., and Guery-Odelin, D. (2002). Loading of a cold atomic beam into a magnetic guide. *European Physical Journal D*, 20:107.

[Dalibard and Cohen-Tannoudji, 1989] Dalibard, J. and Cohen-Tannoudji, C. (1989). Laser cooling below the doppler limit by polarization gradients: simple theoretical models. *J.O.S.A. B*, 6:2046.

[Davis et al., 1995] Davis, K. B., Mewes, M. O., Andrews, M. R., van Druten, N. J., Durfee, D. S., Kurn, D. M., and Ketterle, W. (1995). Bose-einstein condensation in a gas of sodium atoms. *Physical Review Letters*, 75:3969.

[DeMille, 2002] DeMille, D. (2002). Quantum computation with trapped polar molecules. *Phys. Rev. Lett.*, 88(6):067901.

[Demkov and Ostrovsky, 2001] Demkov, Y. N. and Ostrovsky, V. N. (2001). The exact solution of the multistate landau-zener type model: the generalized bow-tie model. *Journal of Physics B: Atomic, Molecular and Optical Physics*, 34(12):2419.

[Doyle et al., 1995] Doyle, J. M., Friedrich, B., Kim, J., and Patterson, D. (1995). Buffer-gas loading of atoms and molecules into a magnetic trap. *Phys. Rev. A*, 52(4):R2515–R2518.

[Egorov et al., 2002] Egorov, D., Lahaye, T., Schöllkopf, W., Friedrich, B., and Doyle, J. M. (2002). Buffer-gas cooling of atomic and molecular beams. *Phys. Rev. A*, 66(4):043401.

[Enomoto and Momose, 2005] Enomoto, K. and Momose, T. (2005). Microwave stark decelerator for polar molecules. *Phys. Rev. A*, 72:061403.

[Enss and Hunklinger, 2005] Enss, C. and Hunklinger, S. (2005). *Low-Temperature Physics*. SpringerLink: Springer e-Books. Springer.

[Falkenau, 2011] Falkenau, M. (2011). *Continuous loading of an optical dipole trap*. PhD thesis, Universität Stuttgart.

[Falkenau et al., 2012] Falkenau, M., Volchkov, V. V., Rührig, J., Gorniaczyk, H., and Griesmaier, A. (2012). Evaporation-limited loading of an atomic trap. *Phys. Rev. A*, 85:023412.

[Falkenau et al., 2011] Falkenau, M., Volchkov, V. V., Rührig, J., Griesmaier, A., and Pfau, T. (2011). Continuous loading of a conservative potential trap from an atomic beam. *Phys. Rev. Lett.*, 106(16):163002.

[Fattori et al., 2006] Fattori, M., Koch, T., Goetz, S., Griesmaier, A., Hensler, S., Stuhler, J., and Pfau, T. (2006). Demagnetization cooling of a gas. *Nature Physics*, 2(11):765–768.

[Fedichev et al., 1996] Fedichev, P. O., Reynolds, M. W., Rahmanov, U. M., and Shlyapnikov, G. V. (1996). Inelastic decay processes in a gas of spin-polarized triplet helium. *Phys. Rev. A*, 53:1447–1453.

[Fioretti et al., 1998] Fioretti, A., Molisch, A., Müller, J., Verkerk, P., and Allegrini, M. (1998). Observation of radiation trapping in a dense cs magneto-optical trap. *Optics Communications*, 149(46):415 – 422.

[Fuhrmanek et al., 2012] Fuhrmanek, A., Bourgain, R., Sortais, Y. R. P., and Browaeys, A. (2012). Light-assisted collisions between a few cold atoms in a microscopic dipole trap. *Phys. Rev. A*, 85:062708.

[Gallagher and Pritchard, 1989] Gallagher, A. and Pritchard, D. E. (1989). Exoergic collisions of cold Na*-Na. *Phys. Rev. Lett.*, 63:957–960.

[Gaunt et al., 2013] Gaunt, A. L., Schmidutz, T. F., Gotlibovych, I., Smith, R. P., and Hadzibabic, Z. (2013). Bose-einstein condensation of atoms in a uniform potential. *Phys. Rev. Lett.*, 110:200406.

[Gorniaczyk, 2012] Gorniaczyk, H. (2012). A crossed optical dipole trap. Master's thesis, Universität Stuttgart.

[Götz, 2006] Götz, S. (2006). Demagnetization cooling in an ultracold chromium gas. Master's thesis, Universität Stuttgart.

[Greiner, 2008] Greiner, A. (2008). *Erzeugung eines lasergekühlten Atomstrahls in einem Magnetleiter - Eine intensive Quelle für die Atomlithographie.* PhD thesis, Universität Stuttgart.

[Greiner et al., 2007] Greiner, A., Sebastian, J., Rehme, P., Aghajani-Talesh, A., Griesmaier, A., and Pfau, T. (2007). Loading chromium atoms in a magnetic guide. *J. Phys B: At. Mol. Opt. Phys.*, 40(5):F77–F84.

[Greiner et al., 2002] Greiner, M., Mandel, O., Esslinger, T., Hänsch, T. W., and Bloch, I. (2002). Quantum phase transition from a superfluid to a mott insulator in a gas of ultracold atoms. *Nature*, 415(6867):39–44.

[Griesmaier, 2006] Griesmaier, A. (2006). *Dipole-dipole interaction in a degenerate quantum gas.* PhD thesis, Universität Stuttgart.

[Griesmaier et al., 2009] Griesmaier, A., Greiner, A., Sebastian, J., Aghajani-Talesh, A., Falkenau, M., Rehme, P., and Pfau, T. (2009). A high flux of ultra-cold chromium atoms in a magnetic guide. *J. Phys B: At. Mol. Opt. Phys.*, 42:145306.

[Grimm et al., 2000] Grimm, R., Weidemüller, M., and Ovchinnikov, Y. B. (2000). Optical dipole traps for neutral atoms. volume 42 of *Advances In Atomic, Molecular, and Optical Physics*, pages 95 – 170. Academic Press.

[Hagley et al., 1999] Hagley, E. W., Deng, L., Kozuma, M., Wen, J., Helmerson, K., Rolston, S. L., and Phillips, W. D. (1999). A well-collimated quasi-continuous atom laser. *Science*, 283(5408):1706–1709.

[Harris et al., 2004] Harris, J. G. E., Michniak, R. A., Nguyen, S. V., Campbell, W. C., Egorov, D., Maxwell, S. E., van Buuren, L. D., and Doyle, J. M. (2004). Deep superconducting magnetic traps for neutral atoms and molecules. *Review of Scientific Instruments*, 75(1):17–23.

[Hensler et al., 2003] Hensler, S., A.Görlitz, S.Giovanazzi, and T.Pfau (2003). Dipolar relaxation in an ultra-cold gas of magnetically trapped chromium atoms. *Appl.Phys.B*, 77:765.

[Hensler et al., 2005] Hensler, S., Greiner, A., Stuhler, J., and Pfau, T. (2005). Depolarisation cooling of an atomic cloud. *EPL (Europhysics Letters)*, 71(6):918.

[Hess, 1986] Hess, H. F. (1986). Evaporative cooling of magnetically trapped and compressed spin-polarized hydrogen. *Phys.Rev.B*, 34:3476.

[Hung et al., 2013] Hung, C.-L., Gurarie, V., and Chin, C. (2013). From cosmology to cold atoms: Observation of sakharov oscillations in a quenched atomic superfluid. *Science*, 341(6151):1213–1215.

[Ido et al., 2000] Ido, T., Isoya, Y., and Katori, H. (2000). Optical-dipole trapping of sr atoms at a high phase-space density. *Phys. Rev. A*, 61:061403.

[Janis et al., 2005] Janis, J., Banks, M., and Bigelow, N. P. (2005). rf-induced sisyphus cooling in a magnetic trap. *Phys. Rev. A*, 71:013422.

[Julienne and Vigué, 1991] Julienne, P. S. and Vigué, J. (1991). Cold collisions of ground- and excited-state alkali-metal atoms. *Physical Review A*, 44:4464.

[Kagan et al., 1981] Kagan, Y., Vartanyants, I., and Shlyapnikov, G. (1981). Kinetics of decay of metastable gas phase of polarized atomic hydrogen at low temperatures. *Sov. Phys. JETP*, 54:590–604.

[Kasevich et al., 1989] Kasevich, M. A., Riis, E., Chu, S., and DeVoe, R. G. (1989). Atomic fountains and clocks. *Optics News*, 15(12):31–32.

[Kastler, 1950] Kastler, A. (1950). Quelques suggestions concernant la production optique et la dtection optique d'une ingalit de population des niveaux de quantifigation spatiale des atomes. application l'exprience de stern et gerlach et la rsonance magntique. *Le Journal de Physique et le Radium*, 11(6):255.

[Katori et al., 1999] Katori, H., Ido, T., Isoya, Y., and Kuwata-Gonokami, M. (1999). Magneto-optical trapping and cooling of strontium atoms down to the photon recoil temperature. *Phys. Rev. Lett.*, 82:1116–1119.

[Ketterle et al., 1993] Ketterle, W., Davis, K., Joffe, M., Martin, A., and Pritchard, D. E. (1993). High densities of cold atoms in a dark spontaneous-force optical trap. *Phys.Rev.Lett*, 70:2253.

[Ketterle et al., 1999] Ketterle, W., Durfee, D. S., and Stamper-Kurn, D. M. (1999). Making, probing and understanding bose-einstein condensates. In *Bose-Einstein condensation in atomic gases*, pages 67–176.

[Ku et al., 2012] Ku, M. J. H., Sommer, A. T., Cheuk, L. W., and Zwierlein, M. W. (2012). Revealing the superfluid lambda transition in the universal thermodynamics of a unitary fermi gas. *Science*, 335(6068):563–567.

[Kuppens et al., 2000] Kuppens, S. J. M., Corwin, K. L., Miller, K. W., Chupp, T. E., and Wieman, C. E. (2000). Loading an optical dipole trap. *Phys. Rev. A*, 62:013406.

[Labeyrie et al., 2003] Labeyrie, G., Vaujour, E., Müller, C. A., Delande, D., Miniatura, C., Wilkowski, D., and Kaiser, R. (2003). Slow diffusion of light in a cold atomic cloud. *Phys. Rev. Lett.*, 91:223904.

[Lagendijk et al., 1986] Lagendijk, A., Silvera, I. F., and Verhaar, B. J. (1986). Spin exchange and dipolar relaxation rates in atomic hydrogen: Lifetimes in magnetic traps. *Phys. Rev. B*, 33:626–628.

[Lawall et al., 1995] Lawall, J., Kulin, S., Saubamea, B., Bigelow, N., Leduc, M., and Cohen-Tannoudji, C. (1995). Three-dimensional laser cooling of helium beyond the single-photon recoil limit. *Phys. Rev. Lett.*, 75:4194–4197.

[LeBlanc and Thywissen, 2007] LeBlanc, L. J. and Thywissen, J. H. (2007). Species-specific optical lattices. *Physical Review A (Atomic, Molecular, and Optical Physics)*, 75(5):053612.

[Lett et al., 1993] Lett, P. D., Helmerson, K., Phillips, W. D., Ratliff, L. P., Rolston, S. L., and Wagshul, M. E. (1993). Spectroscopy of na_2 by photoassociation of laser-cooled na. *Phys. Rev. Lett.*, 71:2200–2203.

[Lu et al., 2012] Lu, M., Burdick, N. Q., and Lev, B. L. (2012). Quantum degenerate dipolar fermi gas. *Phys. Rev. Lett.*, 108:215301.

[Madison et al., 2000] Madison, K. W., Chevy, F., Wohlleben, W., and Dalibard, J. (2000). Vortex formation in a stirred bose-einstein condensate. *Phys. Rev. Lett.*, 84:806–809.

[McClelland and Hanssen, 2006] McClelland, J. J. and Hanssen, J. L. (2006). Laser cooling without repumping: A magneto-optical trap for erbium atoms. *Phys. Rev. Lett.*, 96(14):143005.

[Metcalf and van der Straten, 2002] Metcalf, H. J. and van der Straten, P. (2002). *Laser Cooling and Trapping.* Springer-Verlag.

[Mewes et al., 1997] Mewes, M.-O., Andrews, M. R., Kurn, D. M., Durfee, D. S., Townsend, C. G., and Ketterle, W. (1997). Output coupler for bose-einstein condensed atoms. *Physical Review Letters*, 78:582.

[Migdall et al., 1985] Migdall, A., Prodan, J., and Phillips, W. (1985). First observation of magnetically trapped neutral atoms. *Phys.Rev.Lett*, 54:2596.

[Miller et al., 2002] Miller, K. W., Dürr, S., and Wieman, C. E. (2002). rf-induced sisyphus cooling in an optical dipole trap. *Phys. Rev. A*, 66:023406.

[Narevicius et al., 2008] Narevicius, E., Libson, A., Parthey, C. G., Chavez, I., Narevicius, J., Even, U., and Raizen, M. G. (2008). Stopping supersonic beams with a series of pulsed electromagnetic coils: An atomic coilgun. *Phys. Rev. Lett.*, 100(9):093003.

[Newbury et al., 1995] Newbury, N. R., Myatt, C. J., Cornell, E. A., and Wieman, C. E. (1995). Gravitational sisyphus cooling of ^{87}Rb in a magnetic trap. *Phys. Rev. Lett.*, 74:2196–2199.

[Olson et al., 2013] Olson, A. J., Niffenegger, R. J., and Chen, Y. P. (2013). Optimizing the efficiency of evaporative cooling in optical dipole traps. *Phys. Rev. A*, 87:053613.

[Olson et al., 2006] Olson, S. E., Mhaskar, R. R., and Raithel, G. (2006). Continuous propagation and energy filtering of a cold atomic beam in a long high-gradient magnetic atom guide. *Physical Review A*, 73:033622.

[Onofrio et al., 2000] Onofrio, R., Raman, C., Vogels, J. M., Abo-Shaeer, J. R., Chikkatur, A. P., and Ketterle, W. (2000). Observation of superfluid flow in a bose-einstein condensed gas. *Phys. Rev. Lett.*, 85(11):2228–2231.

[Ovchinnikov et al., 1997] Ovchinnikov, Y. B., Manek, I., and Grimm, R. (1997). Surface trap for cs atoms based on evanescent-wave cooling. *Phys. Rev. Lett.*, 79:2225–2228.

[Pasquiou et al., 2010] Pasquiou, B., Bismut, G., Beaufils, Q., Crubellier, A., Maréchal, E., Pedri, P., Vernac, L., Gorceix, O., and Laburthe-Tolra, B. (2010). Control of dipolar relaxation in external fields. *Phys. Rev. A*, 81:042716.

[Pasquiou et al., 2011] Pasquiou, B., Maréchal, E., Bismut, G., Pedri, P., Vernac, L., Gorceix, O., and Laburthe-Tolra, B. (2011). Spontaneous demagnetization of a dipolar spinor bose gas in an ultralow magnetic field. *Phys. Rev. Lett.*, 106:255303.

[Patterson et al., 2009] Patterson, D., Rasmussen, J., and Doyle, J. M. (2009). Intense atomic and molecular beams via neon buffer-gas cooling. *New Journal of Physics*, 11(5):055018.

[Price et al., 2008] Price, G. N., Bannerman, S. T., Viering, K., Narevicius, E., and Raizen, M. G. (2008). Single-photon atomic cooling. *Phys. Rev. Lett.*, 100(9):093004.

[Pritchard, 1983] Pritchard, D. E. (1983). Cooling neutral atoms in a magnetic trap for precision spectroscopy. *Phys.Rev.Lett.*, 51:1336.

[Raab et al., 1987] Raab, E. L., Prentiss, M., Cable, A., Chu, S., and Pritchard, D. E. (1987). Trapping of neutral sodium atoms with radiation pressure. *Phys. Rev. Lett.*, 59(23):2631–2634.

[Ramsey, 1983] Ramsey, N. F. (1983). History of atomic clocks. *JOURNAL OF RESEARCH of the National Bureau of Standards*, 88(5):301–320.

[Rangwala et al., 2003] Rangwala, S. A., Junglen, T., Rieger, T., Pinkse, P. W. H., and Rempe, G. (2003). Continuous source of translationally cold dipolar molecules. *Phys. Rev. A*, 67(4):043406.

[Ratschbacher et al., 2013] Ratschbacher, L., Sias, C., Carcagni, L., Silver, J. M., Zipkes, C., and Köhl, M. (2013). Decoherence of a single-ion qubit immersed in a spin-polarized atomic bath. *Phys. Rev. Lett.*, 110:160402.

[Robins et al., 2008] Robins, N. P., Figl, C., Jeppesen, M., Dennis, G. R., and Close, J. D. (2008). A pumped atom laser. *Nature Physics*, 4(9):731–736.

[Roos et al., 2003] Roos, C. F., Cren, P., Gury-Odelin, D., and Dalibard, J. (2003). Continuous loading of a non-dissipative atom trap. *Europhysics Letters*, 61:187.

[Rührig, 2011] Rührig, J. (2011). Continuous loading of an optical dipole trap using ultra cold chromium atoms. Master's thesis, Universität Stuttgart.

[Rührig, 2014] Rührig, J. (2014). PhD thesis, Universität Stuttgart.

[Santos et al., 2007] Santos, L., Fattori, M., Stuhler, J., and Pfau, T. (2007). Spinor condensates with a laser-induced quadratic zeeman effect. *Phys. Rev. A*, 75:053606.

[Santos et al., 2001] Santos, L., Floegel, F., Pfau, T., and Lewenstein, M. (2001). Continuous optical loading of a bose-einstein condensate. *Phys. Rev. A*, 63(6):063408.

[Schmaljohann et al., 2004] Schmaljohann, H., Erhard, M., Kronjäger, J., Kottke, M., van Staa, S., Cacciapuoti, L., Arlt, J. J., Bongs, K., and Sengstock, K. (2004). Dynamics of $f = 2$ spinor bose-einstein condensates. *Phys. Rev. Lett.*, 92:040402.

[Schmidt et al., 2003] Schmidt, P. O., Hensler, S., Werner, J., Binhammer, T., Görlitz, A., and Pfau, T. (2003). Continuous loading of cold atoms into a ioffe-pritchard magnetic trap. *Journal of Optics B*, 5:S170.

[Schmiedmayer, 1995] Schmiedmayer, J. (1995). Guiding and trapping a neutral atom on a wire. *Phys. Rev. A*, 52(1):R13–R16.

[Serwane et al., 2011] Serwane, F., Zürn, G., Lompe, T., Ottenstein, T. B., Wenz, A. N., and Jochim, S. (2011). Deterministic preparation of a tunable few-fermion system. *Science*, 332(6027):336–338.

[Sesko et al., 1989] Sesko, D., Walker, T., Monroe, C., Gallagher, A., and Wieman, C. (1989). Collisional losses from a light-force atom trap. *Phys. Rev. Lett.*, 63:961–964.

[Shlyapnikov et al., 1994] Shlyapnikov, G. V., Walraven, J. T. M., Rahmanov, U. M., and Reynolds, M. W. (1994). Decay kinetics and bose condensation in a gas of spin-polarized triplet helium. *Phys. Rev. Lett.*, 73:3247–3250.

[Shuman et al., 2010] Shuman, E. S., Barry, J. F., and DeMille, D. (2010). Laser cooling of a diatomic molecule. *Nature (London)*, (467):820–823.

[Shytov, 2004] Shytov, A. V. (2004). Landau-zener transitions in a multilevel system: An exact result. *Phys. Rev. A*, 70:052708.

[Sidorenkov et al., 2013] Sidorenkov, L. A., Khoon Tey, M., Grimm, R., Hou, Y.-H., Pitaevskii, L., and Stringari, S. (2013). Second sound and the superfluid fraction in a resonantly interacting Fermi gas. *Nature*, 498:78–81.

[Smith and Pethick, 2002] Smith, H. and Pethick, C. (2002). *Bose-Einstein Condensation in Dilute Gases*. Cambridge Universtiy Press.

[Stamper-Kurn et al., 1998a] Stamper-Kurn, D. M., Andrews, M. R., Chikkatur, A. P., Inouye, S., Miesner, H.-J., Stenger, J., and Ketterle, W. (1998a). Optical confinement of a bose-einstein condensate. *Phys. Rev. Lett.*, 80:2027–2030.

[Stamper-Kurn et al., 1998b] Stamper-Kurn, D. M., Miesner, H.-J., Chikkatur, A. P., Inouye, S., Stenger, J., and Ketterle, W. (1998b). Reversible formation of a bose-einstein condensate. *Phys. Rev. Lett.*, 81:2194–2197.

[Swope et al., 1982] Swope, W. C., Andersen, H. C., Berens, P. H., and Wilson, K. R. (1982). A computer simulation method for the calculation of equilibrium constants for the formation of physical clusters of molecules: Application to small water clusters. *The Journal of Chemical Physics*, 76(1):637–649.

[Tarbutt et al., 2004] Tarbutt, M. R., Bethlem, H. L., Hudson, J. J., Ryabov, V. L., Ryzhov, V. A., Sauer, B. E., Meijer, G., and Hinds, E. A. (2004). Slowing heavy, ground-state molecules using an alternating gradient decelerator. *Phys. Rev. Lett.*, 92:173002.

[Thorsheim et al., 1987] Thorsheim, H. R., Weiner, J., and Julienne, P. S. (1987). Laser-induced photoassociation of ultracold sodium atoms. *Phys. Rev. Lett.*, 58:2420–2423.

[Tsuji et al., 2010] Tsuji, H., Sekiguchi, T., Mori, T., Momose, T., and Kanamori, H. (2010). Stark velocity filter for nonlinear polar molecules. *Journal of Physics B: Atomic, Molecular and Optical Physics*, 43(9):095202.

[van Buuren et al., 2009] van Buuren, L. D., Sommer, C., Motsch, M., Pohle, S., Schenk, M., Bayerl, J., Pinkse, P. W. H., and Rempe, G. (2009). Electrostatic extraction of cold molecules from a cryogenic reservoir. *Phys. Rev. Lett.*, 102(3):033001.

[van de Meerakker et al., 2005] van de Meerakker, S. Y. T., Smeets, P. H. M., Vanhaecke, N., Jongma, R. T., and Meijer, G. (2005). Deceleration and electrostatic trapping of oh radicals. *Phys. Rev. Lett.*, 94(2):023004.

[Vanhaecke et al., 2007] Vanhaecke, N., Meier, U., Andrist, M., Meier, B. H., and Merkt, F. (2007). Multistage zeeman deceleration of hydrogen atoms. *Phys. Rev. A*, 75(3):031402.

[Volchkov et al., 2013] Volchkov, V. V., Rührig, J., Pfau, T., and Griesmaier, A. (2013). Efficient demagnetization cooling of atoms and its limits. *arXiv 1306.3365*.

[Volchkov et al., 2013] Volchkov, V. V., Rührig, J., Pfau, T., and Griesmaier, A. (2013). Sisyphus cooling in a continuously loaded trap. *New Journal of Physics*, 15(9):093012.

[Vutha et al., 2011] Vutha, A. C., Campbell, W. C., Gurevich, Y. V., Hutzler, N. R., Parsons, M., Patterson, D., Petrik, E., Spaun, B., Doyle, J. M., Gabrielse, G., and DeMille, D. (2011). Search for the electric dipole moment of the electron with thorium monoxide. *Journal of Physics B: Atomic, Molecular and Optical Physics*, 44(7):079803.

[Weiner et al., 1999] Weiner, J., Bagnato, V. S., Zilio, S., and Julienne, P. S. (1999). Experiments and theory in cold and ultracold collisions. *Rev. Mod. Phys.*, 71:1–85.

[Wenzel, 2012] Wenzel, M. (2012). Aktive magnetfeldkompensation für atomoptische experimente.

[Wu and Foot, 1996] Wu, H. and Foot, C. J. (1996). Direct simulation of evaporative cooling. *Journal of Physics B: Atomic, Molecular and Optical Physics*, 29(8):L321.

[Zeppenfeld et al., 2012] Zeppenfeld, M., Englert, B. G. U., Glöckner, R., Prehn, A., Mielenz, M., Sommer, C., van Buuren, L. D., Motsch, M., and Rempe, G. (2012). Sisyphus cooling of electrically trapped polyatomic molecules. *Nature*, 491:570–573.

Danksagung

An dieser Stelle möchte ich mich bei allen bedanken, die mich durch diese Arbeit begleitet haben.

Mein besonderer Dank gilt Tilman Pfau für das Aufnehmen in das 5. Physikalische Institut und die Möglichkeit am Chrom II Experiment mitzuwirken. Die vielen wertvollen Diskussionen möchte ich nicht missen. Vor allem danke ich Tilman aber für das Vertrauen und die Freiheit zu experimentieren.

Herrn Prof. Jörg Wrachtrup danke ich für die freundliche Übernahme des Mitberichts.

Axel Griesmaier danke ich für die spannende Zeit im Labor und die Erfahrung, die er mit mir geteilt hat, seien es technische Fragen zu Elektronik, physikalische Grundlagen wie nicht-lineare Optik oder wissenschaftliches Schreiben.

Weiterhin möchte ich mich bei allen Weggefährten am Chrom II Experiment bedanken, insbesondere bei:

- Anoush Aghajani-Talesh, für die Einführung in das Experiment.
- Markus Falkenau, nicht nur für ausgezeichnete Zusammenarbeit am Experiment, sondern auch für die gemeinsamen Unternehmungen ausserhalb des Labors.
- Jahn Rührig danke ich für die tatkräftige Unterstützung am Experiment, gerade in den letzten beiden Jahren.
- Hannes Gorniaczyk, Matthias Wenzel und Stephan Jennewein für ihren unbeirrbaren Einsatz im Labor und ihren Optimismus.

Karin Otter, Beatrice Olgun-Lichtenberg, Karin Hauff und Oliver Nagel bin ich besonders dankbar für das Erleichtern aller bürokratischen Anliegen. Genauso wie ich Harald Kübler, Paul Rehme und Bernhard Huber für das Aufrechterhalten einer fortschritlichen und funktionierenden Computerinfrastruktur danke.

Ich danke allen Mitgliedern des 5. Physikalischen Instituts für die gemeinsamen sportlichen Events, Feiern und „Denkpausen“ – oder teamarbeitsfördernde Abendprogramme.

Ein großer Dank geht an meine Familie und an Kathrin, die mich besonders dadurch unterstützt haben, dass sie immer meinen regelmässigen Versuchen, ihnen den Inhalt und den Sinn dieser Arbeit zu erklären, standgehalten haben.